СПЕКТРОСКОПИЧЕСКИ И/ИЛИ СТРУКТУРНО ИНТРИГУЮЩИЕ ФТАЛОЦИАНИНЫ И РОДСТВЕННЫЕ СОЕДИНЕНИЯ. ЧАСТЬ 1. МОНОМЕРНЫЕ СИСТЕМЫ

Н. Кобаяши

Нагао Кобаяши

Кафедра химии и материалов, Факультет текстильных наук и технологии, Университет Шиншу, Уеда, 386-8567, Япония
E-mail: nagaok@shinshu-u.ac.jp, nagaok@m.tohoku.ac.jp

Представлена первая часть серии обзорных работ по свойствам некоторых синтетически и спектроскопически интересных исследований нашей группы за период 2007-2017 гг. В частности, приведены примеры анализа спектроскопических данных в сочетании с расчетами методом молекулярных орбиталей. Мы использовали в основном спектроскопические методы электронного поглощения и естественного и магнитного кругового дихроизма, периодически применяя флуоресценцию, фосфоресценцию и ЭПР с временным разрешением. Теоретически проанализированы спектры (4n + 2) π систем, а также некоторые 4nπ антиароматических систем, что помогает читателю интерпретировать спектральные данные. В первой части и второй частях этого обзора рассматриваются мономерные системы, а в третьей - тримерные и тетрамерные системы.

Ключевые слова: порфирин, фталоцианин, структура, спектроскопия, расчеты молекулярных орбиталей (МО)

SPECTROSCOPICALLY AND/OR STRUCTURALLY INTRIGUING PHTHALOCYANINES AND RELATED COMPOUNDS. PART 1. MONOMERIC SYSTEMS

N. Kobayashi

Nagao Kobayashi

Department of Chemistry and Materials, Faculty of Textile Science and Technology, Shinshu University, Ueda, 386-8567, Japan
E-mail: nagaok@shinshu-u.ac.jp, nagaok@m.tohoku.ac.jp

The first part of the series of review papers on the properties of some synthetically and spectroscopically interesting studies of our group for the period 2007-2017 is presented. In particular, examples are shown on the analysis of spectroscopic data in conjunction with molecular orbital (MO) calculations. We have used mainly electronic absorption and natural and magnetic circular dichroism (CD and MCD) spectroscopic techniques, with occasional use of fluorescence, phosphorescence, and time-resolved ESR. Not only the spectra of (4n + 2) π systems, but also some 4nπ anti-aromatic systems are theoretically analyzed, which helps the reader to learn how to interpret the spectral data. In the first part and the second part of this review monomer systems are considered, and in the third - trimeric and tetrameric systems.

Key words: porphyrin, phthalocyanine, structure, spectroscopy, molecular orbital (MO) calculations

INTRODUCTION

Since their first synthesis of more than 110 years ago, [1] many peoples have been involved in the research of phthalocyanines (Pcs) and related compounds. Pcs are an important industrial commodity used in inks, coloring for plastics and metal surfaces, and dyestuffs and the number of literatures and patents in the 21st century exceeds more than 2000 per year. The future potential uses of metalloPcs (MtPcs), currently under study, include for example photodynamic reagents for cancer therapy and other medical applications, solar cells, electrochromic display devices, and sensing elements in chemical sensors. We summarized some research fields of MtPcs and related compounds in the last 20 years from time to time as reviews [2-28] and in book chapters. [29-62] In this review, we introduce some of our representative works in the last 12 years on Pcs and related compounds, summarized mainly on the basis of spectroscopic interest and specific properties.

MONOMERIC SYSTEMS

2-1. Nearly Planar (Low Symmetry) Systems
a) Relationship between Symmetry of Porphyrinic π-Conjugated Systems and Singlet Oxygen ($^1\Delta_g$) Yields. Previously, we reported the relationship between molecular symmetry and absorption spectra of tetraazaporphyrins (TAPs) and phthalocyanine (Pc) analogues [22, 30, 63, 64]. However, the relationship between the molecular symmetry and singlet oxygen yields ($^1\Delta_g$) which is important in the field of, for example, photodynamic therapy was not examined. Accordingly, the excited-state properties and singlet oxygen generation mechanism were examined in phthalocyanines (**4M**; H_2, Mg, or Zn) and in low-symmetry metal-free, magnesium, and zinc TAPs, that is, monobenzo-substituted (**1M**), *adjacently* dibenzo-substituted (**2AdM**), *oppositely* dibenzo-substituted (**2OpM**), and tribenzo-substituted (**3M**) TAP derivatives, whose π conjugated systems were altered by fusing benzo rings (Fig.1) [65].

Figure 2 exhibits the absorption spectra of Mg and H_2 derivatives shown in Fig. 1. The important point in this figure [6, 30, 65, 66] is that the compounds with D_{4h} symmetry do not show the splitting of both the Soret (B) and Q bands theoretically. The C_{2v} type compound such as **2AdMg** also does not show splitting

but in this case the splitting is so small that seemingly a single peak appears in both the Q and B band regions.
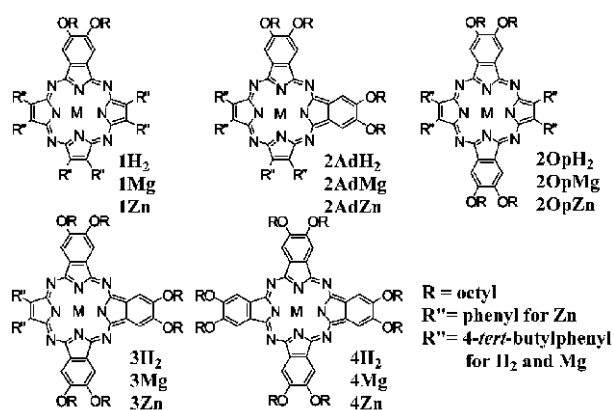

Fig. 1. Molecular structures of low-symmetry TAP derivatives
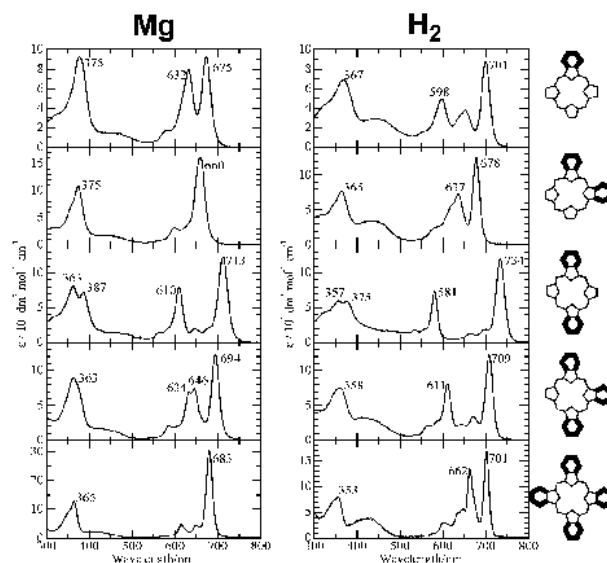Рис. 1. Строение молекул нихкосимметричных ТАР производных

Fig. 2. Electronic absorption spectra of Mg (left) and H_2 (right) compounds
Рис. 2. Электронные спектры поглощения соединений Mg(слева) и H_2 (справа)

The D_{2h} type compound (**2OpMg**) shows the largest splitting, and the central energy of the split bands is very close to that of C_{2v} type compound. In the case of H_2 compounds, pyrrole protons are bound to the pyrrole Ns along the short-axis. This has been confirmed by comparing experimental splitting of the Q band and calculated splitting. If the pyrrole protons are

Izv. Vyssh. Uchebn. Zaved. Khim. Khim. Tekhnol. 2019. V. 62. N 4

5

linked to pyrrole Ns along the long axis, the splitting of the Q band is much smaller than in the experiments. Due to the low symmetry of the compounds, all H_2 derivatives theoretically show split absorption bands.

The luminescence, particularly phosphorescence spectra of porphyrins and phthalocyanines are very rare because of the low phosphorescence efficiency so that systematic data of low-symmetry porphyrinoids have not been reported to date. In Fig. 3, we show the fluorescence and phosphorescence spectra of our Mg- and H_2TAPs observed in the near-IR region, apart from **4H_2**. The T_{1x} energy of the Mg complexes decreased in the order of **1Mg**>**2AdMg**>**3Mg**>**2OpMg**> >**4Mg**, which is similar to the Zn complexes [64]. In the case of metal-free compounds, the T_{1x} energy decreased in the order of **1H_2**>**3H_2**>**2OpH_2**>**2AdH_2**.
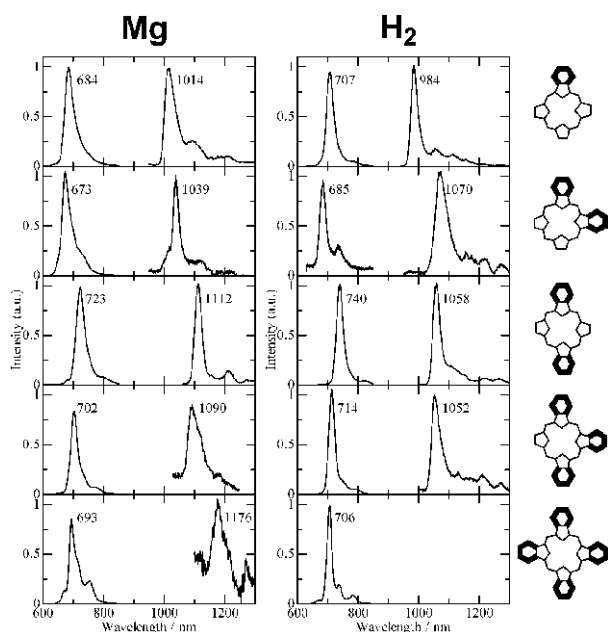

Fig. 3. The luminescence spectra of Mg (left) and H_2 (right) compounds. The fluorescence and phosphorescence spectra were at ambient temperature and 77K, respectively

Рис. 3. Спектры люминесценци соединений Mg(слева) и H_2 (справа). Спектры флуоресценции и фосфоресценции при темпертуре окрюжающей среды и 77 К, соответственно

Singlet oxygen yield (Φ_Δ) in the presence of these compounds were also investigated by monitoring the singlet oxygen ($^1\Delta_g$) luminescence at 1275 nm, and the values are summarized in Fig. 4. From this figure, we can see two important features. 1) The Φ_Δ values of the Zn complexes are much larger than those of the corresponding Mg complexes, while the electronic structures are similar. This was easily interpreted by conventional spin orbit coupling (SOC) theory, called the heavy atom effect. 2) The Φ_Δ values strongly depend on the shape of the π conjugated system. In particular,

the Φ_Δ dependence of the metal-free derivatives is noteworthy. For example, while the Φ_Δ value of **2AdH_2** is smallest, that of **2OpH_2** is larger than that of **4Zn**, exceeding the heavy atom effect. That is, the Φ_Δ value increases with increasing splitting of the Q band. Thus, we have succeeded in changing the Φ_Δ values by fusing benzo unit.
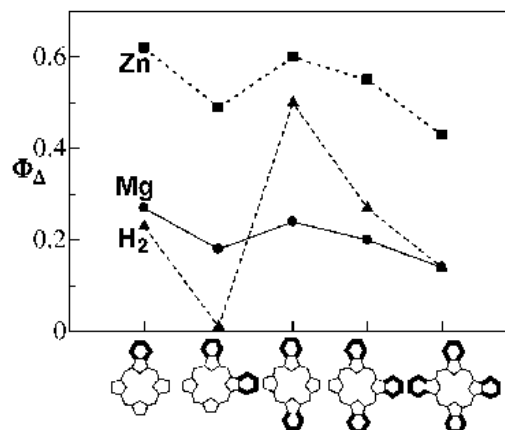

Fig. 4. Relationships between the molecular structures and Φ_Δ values
Рис. 4. Взаимосвязь молекулярного строения и величин Φ_Δ

In order to clarify the singlet oxygen generation mechanism, in the first place, the excited state energies of the Mg and H_2 complexes are determined (Fig. 5). In the case of the Mg complexes, the S_{1x} and S_{1y} energies were determined from the electronic absorption spectra, except those of **2AdMg** which were evaluated by band deconvolution analysis of the electronic absorption and MCD spectra.
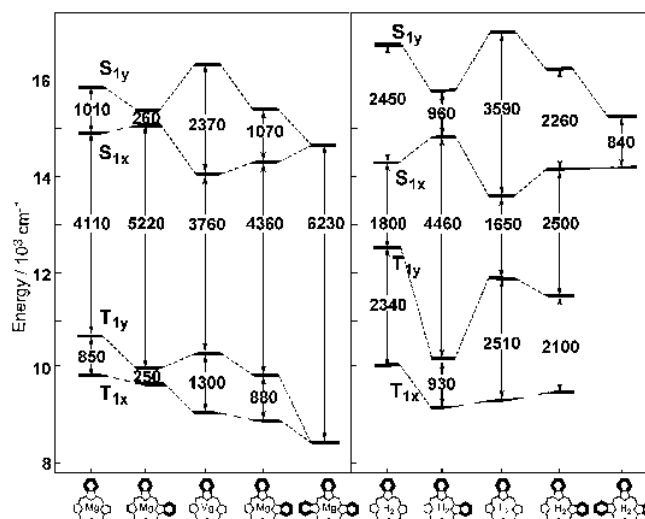

Fig. 5. Summary of the ΔE_{SS} and ΔE_{TT} values of Mg (left) and metal-free (right) complexes
Рис. 5. Сводка значений ΔE_{SS} и ΔE_{TT} для комплексов Mg(слева) и неметаллических комплексов

The T_{1x} energies were determined from the position of phosphorescence peaks. The T_{1y} energies were evaluated by reference to the ΔE_{TT} values of Pd or Zn complexes (ΔE_{TT}: the energy splitting between the T_{1x} and T_{1y} states) [64]. This approximation that the ΔE_{TT} values among the Zn, Pd, and Mg complex is plausible, since the magnitude of the Q band splitting is similar for these complexes when comparing across complexes with the same π system.

In the case of metal-free (H_2) compounds, the S_{1x}, S_{1y}, and T_{1x} energies were determined from the electronic absorption and phosphorescence spectra. However, it was difficult to obtain the T_{1y} energies by directly utilizing the ΔE_{TT} values of the Pd and Zn complexes, since the Q band splitting of metal-free complexes are different from those of the corresponding Zn or Pd complexes. To estimate the ΔE_{TT} values of the metal-free compounds (= $\Delta E_{TT}(H_2)$), the S_{1x}-S_{1y} splitting (= $\Delta E_{SS}(H_2)$) and the $\Delta E_{TT}(H_2)$ values were divided into two parts, i.e.

$$\Delta E_{SS}(H_2) = \Delta E_{SS}^{\pi} + \Delta E_{SS}^{2H}$$
$$\Delta E_{TT}(H_2) = \Delta E_{TT}^{\pi} + \Delta E_{TT}^{2H},$$

where ΔE_{SS}^{π} and ΔE_{TT}^{π} are the S_{1x}-S_{1y} and T_{1x}-T_{1y} splitting due to the lowering of the π symmetry, while those due to inner pyrrole protons are termed ΔE_{SS}^{2H} and ΔE_{TT}^{2H}, respectively. The ΔE_{SS} and ΔE_{TT} values of the Zn complex were used as the ΔE_{SS}^{π} and ΔE_{TT}^{π} values of the metal-free complex, since the splitting of the Q band was similar among Zn, Mg and Pd complexes. From the difference between the $\Delta E_{SS}(H_2)$ and $\Delta E_{SS}(Zn)$ (= ΔE_{SS}^{π}) values, ΔE_{SS}^{2H} was calculated as 1540, 680, 1200, 1200, and 800 cm^{-1} for **1H₂**, **2AdH₂**, **2OpH₂**, **3H₂**, and **4H₂**, respectively. We assumed that $\Delta E_{SS}^{2H} \sim \Delta E_{TT}^{2H}$, since MO calculations suggest that the inner pyrrole protons barely change the π MO coefficients in the HOMO, LUMO, and LUMO+1 that associate to the Q transition. Thus, the $\Delta E_{TT}(H_2)$ value was approximated according to the following equation.
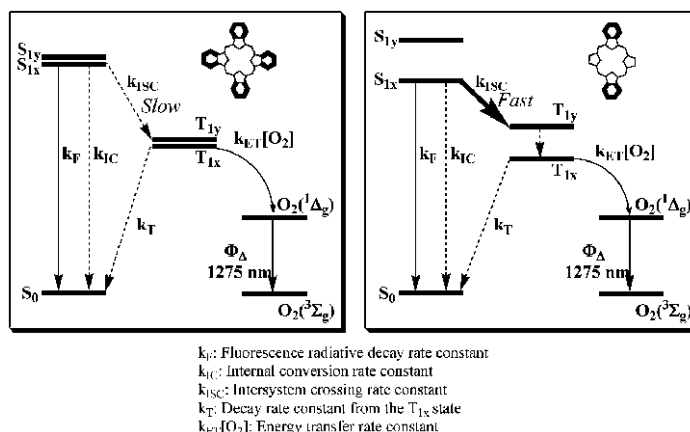
$$\Delta E_{TT}(H_2) = \Delta E_{TT}^{\pi} + \Delta E_{TT}^{2H} = \Delta E_{TT}(Zn) + [\Delta E_{SS}(H_2) - \Delta E_{SS}(Zn)]$$

Using this equation, the excited state energies of the metal-free compounds were evaluated and summarized at the right-hand side of Fig. 5. The important outcome is that the ΔE_{SS} and ΔE_{TT} values of the metal-free complexes are much larger than those of the Zn and Mg complexes due to the inner pyrrole protons.

As shown in Fig. 4, the Φ_Δ value of **2OpH₂** is larger than that of **4Zn**, while **2AdH₂**, being the isomer of **2OpH₂**, exhibited the smallest Φ_Δ value of the compounds examined, indicating that the Φ_Δ value depends

significantly on the symmetry of the ligand π structure. In order to elucidate this phenomenon, the singlet oxygen generation mechanism was discussed.

The singlet oxygen is generated via two processes, i.e. S_1-T_1 intersystem crossing (ISC) of photosensitizer and energy transfer from the T_1 photosensitizer to triplet oxygen ($^3\Sigma_g$) so that the Φ_Δ is expressed by $\Phi_{ET} \times \Phi_{ISC}$, where Φ_{ET} (= $k_{ET}[O_2]/(k_{ET}[O_2] + kT)$) and Φ_{ISC} (= $k_{ISC}/(k_F + k_{IC} + k_{ISC})$) are the quantum yields of energy transfer and ISC, respectively (Scheme 1).

k$_F$: Fluorescence radiative decay rate constant
k$_{IC}$: Internal conversion rate constant
k$_{ISC}$: Intersystem crossing rate constant
k$_T$: Decay rate constant from the T_{1x} state
k$_{ET}[O_2]$: Energy transfer rate constant

Scheme 1. Singlet oxygen generation mechanism in **4M** and **2OpM**
Схема 1. Механизм генерации синглетного кислорода в **4M** и **2OpM**

Since the T_1 lifetimes of our Zn complexes are much longer than the energy transfer, [64] the energy-transfer efficiency is almost 100%, that is, $\Phi_\Delta \sim \Phi_{ISC}$, consistent with previous studies on Pc derivatives [67-69]. Thus, it becomes evident that the S_1-T_1 ISC is the most important process in the relationship between the molecular structures and Φ_Δ values. In the S_1-T_1 ISC, we decided to focus on the ISC from the S_{1x} state to the T_{1y} state (Scheme 1). While the S_{1x} and S_{1y} states or the T_{1x} and T_{1y} states are almost entirely degenerate in the case of **4M** and **2AdM**, those of **1M**, **2OpM**, and **3M** are split. As a result, the energy difference between the S_{1x} and T_{1y} states (=ΔE_{SxTy}) is much smaller in **1M**, **2OpM**, and **3M** than in **4M** and **2AdM**, enhancing the S_{1x}-T_{1y} ISC. Thus, in the next step, the relationship between the S_{1x}-T_{1y} ISC and ΔE_{SxTy} value was discussed. The k_{ISC} value is represented using the wave functions of the S_{1x} (=$|\Phi_n^{Sx}\Phi_{es}^{Sx}\rangle$) and T_{1y} (= $|\Phi_n^{Ty}\Phi_{es}^{Ty}\rangle$) states as follows [70].

$$k_{ISC} \propto |\langle \Phi_n^{Sx}|\Phi_n^{Ty}\rangle|^2 \times |\langle \Phi_{es}^{Sx}|H_{SOC}|\Phi_{es}^{Ty}\rangle|^2$$

Here, $|\langle\Phi_n^{Sx}|\Phi_n^{Ty}\rangle|^2$ and $|\langle\Phi_{es}^{Sx}|H_{SOC}|\Phi_{es}^{Ty}\rangle|^2$ denote the Franck-Condon factor and the SOC matrix element between the S_{1x} and T_{1y} states, respectively. The Franck-Condon factor correlates with the energy

gap between the initial and final states, that is, $|<\Phi_n{}^{Sx}|\Phi_n{}^{Ty}>|^2 \propto \exp(-\Delta E_{SxTy})$ [70]. Under this energy-gap law, the k_{ISC} value is represented as follows.

$$k_{ISC} = \alpha \times |\ \langle \Phi_{es}{}^{Sx} |H_{SOC}|\Phi_{es}{}^{Ty}\rangle\ |^2 \times \exp(-\Delta E_{SxTy})$$

Experimental relationships between the $\Phi_\Delta/\tau F$ ($\sim k_{ISC}$ when $\Phi_\Delta \sim \Phi_{ISC}$) and $\exp(-\Delta E_{SxTy})$ values are shown in Fig. 6.

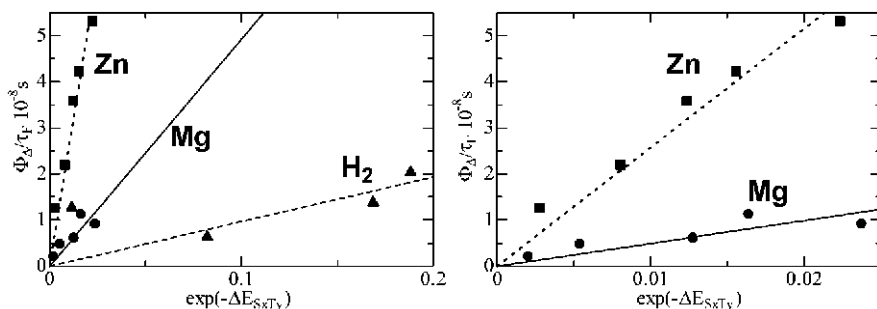Fig. 6. Relationships between the $\Phi_\Delta/\tau F$ and $\exp(-\Delta E_{SxTy})$ values. The ΔE_{SxTy} value is in kcm^{-1}

Рис. 6. Взаимосвязь величин $\Phi_\Delta/\tau F$ и $\exp(-\Delta E_{SxTy})$. ΔE_{SxTy} в ксм$^{-1}$

We see in each compounds, the $\Phi_\Delta/\tau F$ values are proportional to $\exp(-\Delta E_{SxTy})$, indicating that singlet oxygen ($^1\Delta g$) is produced via the T_{1y} state and that the S_{1x} - T_{1y} ISC process follows the energy-gap law. The slope increases in the order $H_2 <$ Mg $<$ Zn, consistent with conventional SOC theory [70]. In the case of the zinc complexes, many EPR results indicate that ISC from the S_{1x} state is selective to the z sublevel in the T_{1y} state, rather than the T_{1x} states, because of the z component of SOC between the d$_{xz}$ and d$_{yz}$ orbitals of the central zinc atom which are admixed with the LUMO and LUMO+1 of the TAP ligand, respectively [64, 71-78]. Therefore, our experimental results for the Zn complexes, where singlet oxygen ($^1\Delta g$) is produced via the T_{1y} state, is consistent with the previous EPR studies. On the other hand, in the case of the metal-free and Mg compounds, selective ISC to the x and y sublevels is dominant because of the x and y components of SOC, which originate from the admixture of the S_1 (or T_1) state and the (σ,π^*) (or (π,σ^*)) configurations via vibronic coupling [71-78]. Thus, the selectivity between the T_{1x} and T_{1y} states had not been clarified. Therefore, these experimental relationships between the $\Phi_\Delta/\tau F$ and $\exp(-\Delta E_{SxTy})$ values became the first experimental evidence of a S_{1x} - T_{1y} ISC process in metal-free and Mg compounds.

Through this study, focusing on low-symmetry TAP derivatives, the singlet oxygen ($^1\Delta g$) generation mechanism was investigated. We have succeeded in increasing the Φ_Δ value by fusing benzo-units and have found a qualitative relationship, where the large Q-band splitting results in efficient generation of singlet oxygen (Φ_Δ). Quantitative analyses on the excited-state energies show that the k_{ISC} value, being proportional to $\exp(-\Delta E_{SxTy})$, follows the energy-gap law. Our results can be utilized for example in the field of photodynamic therapy (PDT). Namely, with respect to PDT, since heavy elements generally exhibit toxicity, our methodology, in which the Φ_Δ value can be controlled by the symmetry of the π conjugated system without heavy elements, should be useful for preparing novel photosensitizers.

b) Electronic structures of azulene-fused porphyrins as seen by magnetic circular dichroism and TD-DFT calculations [79].
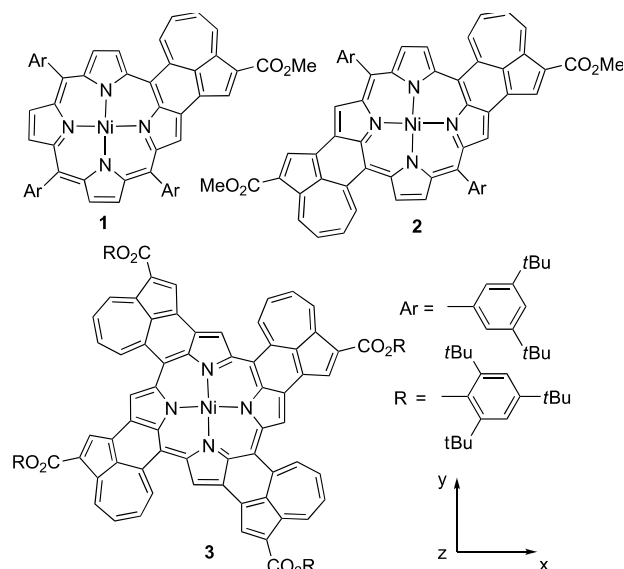
Scheme 2. Azulene-fused porphyrins. Ar = 3,5-di-*tert*- buthyl-phenyl, R = 2, 4, 6-tri-*tert*-butylphenyl. The Ar and R groups were substituted by phenyl and methyl groups, respectively, during DFT and TD-DFT calculations

Схема 2. Исследованные соединения Ar = 3,5-ди-*трет*-бутилфенил, R = 2,4,6-три-*трет*-бутилфенил. Группы Ar и R были замещены фенильной и метильной группами, соответственно, во время расчетов DFT и TD-DFT

It is known that the energy difference between the HOMO and HOMO-1 (ΔHOMO) of normal porphyrins such as tetraphenylporphyrin (TPP) and octaethylporphyrin (OEP) is larger than that between the LUMO and LUMO+1 (ΔLUMO) [71]. By lowering the molecular symmetry of porphyrins, there may be cases that ΔLUMO is larger than ΔHOMO. In order to see this possibility, we have prepared compounds shown in Scheme 2 and compared their electronic ab-

sorption and magnetic circular dichroism (MCD) spectra, and the concomitant MO calculations also supported our experimental data [79]. As will be shown below, low-symmetry compound **2** revealed spectra characteristic of ΔLUMO > ΔHOMO while **1** showed spectra which suggest ΔLUMO ~ ΔHOMO.

Figure 7 shows the electronic absorption and MCD data of the compounds in Scheme 2 and their calculated stick spectra. Intense bands are observed at 684 and 1136 nm in the electronic absorption spectra of **3**, which is saddle-shaped and has C_2 symmetry. A derivative-shaped pseudo A-term in the 1100-1200 nm (Q_{00}) region demonstrates that the two lowest energy singlet states are accidentally near degenerate. A weaker pseudo-A term in the 600-700 nm region points strongly to this being the Soret band region, since there is a smaller angular momentum change associated with the transition and weaker MCD intensity is, therefore, anticipated relative to the Q_{00} bands. In contrast, the absorption spectrum of **1** contains a broad Soret band at 468 nm with a shoulder at 526 nm and well separated Q_{y00} and Q_{x00} bands at 696 and 890 nm, respectively. A weak Q_{00} band means that ΔLUMO ~ ΔHOMO [79]. This pattern is observed in the MCD spectrum of **1** (top left), despite the large angular momentum change associated with the Q band. In contrast, however, the Q_{y00} MCD band at *ca.* 700 nm is clearly positive in sign. The sign sequence of the MCD B term envelopes is, therefore, minus and plus in terms of the $[\theta]_M$ signal. In other word, it is suggested experimentally that the ΔHOMO value is nearly the same as, or slightly larger than, that of the ΔLUMO.

A split Soret band is observed in the electronic absorption spectrum of **2**, at 487 and 545 nm, while there are also three intense peaks at 763, 898, and 1015 nm in the Q band region. The bands at 763 and 1015 nm are assigned as the Q_{y00} and Q_{x00} bands respectively, while the band at 898 nm is assigned as a Q_x vibronic band, based on the sign sequence of the Faraday B terms. The signs of the B-term envelopes are plus and minus for the Q_x and Q_y bands, respectively, which strongly implies that the ΔHOMO value is smaller than that of the ΔLUMO. It is evident, based on the spectra of compounds **1-3**, that the intensity of the Q bands increases as the number of fused azulenes increases, with a concomitant red shift of the Q bands. The intensity of the Q band of **3** suggests that the ΔHOMO value is unusually large for a porphyrin (ΔHOMO would typically be <0.2 eV in DFT based calculations).
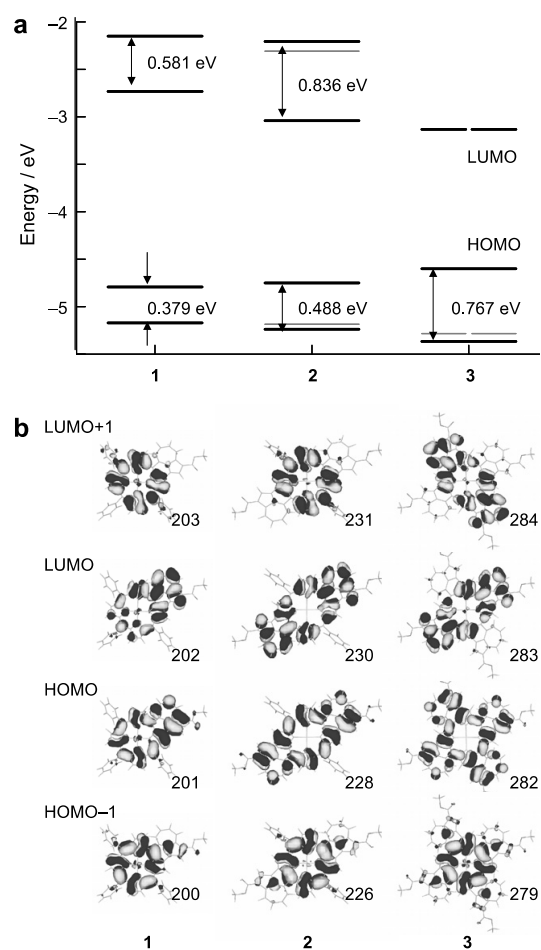
Fig. 8. (a) The energy levels and (b) frontier Kohn-Sham MOs of azulene-fused porphyrins
Рис. 8. (a) Уровни энергии и (b) граничные МО по Кон-Шаму азулин-конденсированных порфиринов

Figure 8 shows the frontier Kohn-Sham MOs of azulene-fused compounds and their energies. For simplicity, we denote only the key Kohn-Sham MOs associated with the Q band transitions. The orbital numbering for compounds **2** and **3** are not consecutive,
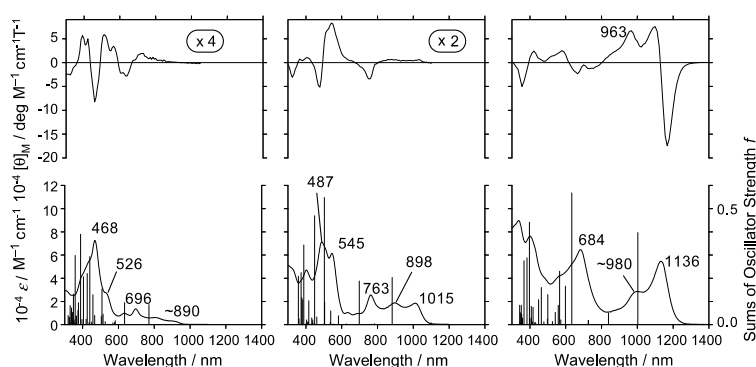

Fig. 7. Experimental electronic absorption (bottom, left scale) and MCD (top) spectra of **1** (left), **2** (center), and **3** (right) in Scheme 2. Solid bars in the absorption spectra (bottom, right scale) indicate the sums of the calculated oscillator strengths over a 1 nm range
Рис. 7. Экспериментальные электронные спектры поглощения (внизу, слева) и спектры MCD (вверху) **1** (слева), **2** (в центре) и **3** (справа) на схеме 2. Сплошные интервалы в спектрах поглощения (внизу, справа) указывают суммы расчетных сил осциллятора в диапазоне 1 нм

Izv. Vyssh. Uchebn. Zaved. Khim. Khim. Tekhnol. 2019. V. 62. N 4

9

therefore, since only the four frontier π-MOs associated with Gouterman's four-orbital model [80] have been selected. It is clear from Fig. 8 that the HOMOs are delocalized over both the porphyrin and azulene units, but that there is a set of nodes between porphyrin and azulene moieties, indicating the presence of anti-bonding interactions between them. Therefore, the energy of the HOMO increases as the number of fused azulene increases. On the other hand, the nodes of HOMO-1 are localized mainly on the porphyrin unit and the azulene units are linked by a bonding interaction, so that the energy levels slightly decrease as the number of azulene unit increases, resulting in an increase in the ΔHOMO value as the number of fused azulenes increases.

The effect of adding fused aromatic rings on the LUMO and LUMO+1 energy was previously discussed and it was concluded that the magnitude of the ΔLUMO value can be explained by using the bonding and anti-bonding interaction on benzo-fusion into account, based on the size of the MO coefficients [64]. It should be noted that the effect of azulene-fusion on the LUMO level is opposite to that of benzo-fusion. In the case of benzo-fusion, the interaction was of an anti-bonding type, while the interaction was of a bonding type in the case of azulene-fusion case, Fig. 8b. When azulene is fused to porphyrins, the LUMO is, therefore, stabilized as a bonding MO.

The trends observed in the electronic absorption and MCD data can be compared with the trends that are predicted for ΔHOMO and ΔLUMO. For **3**, the LUMO and the LUMO+1 are accidentally degenerate since the non-planarity caused in the z-direction by the azulene substituents is symmetrical, so a pseudo-A term was observed in the Q_{00} band region of the MCD spectrum. The intense absorbance of the Q_{00} band can be readily explained based on the large ΔHOMO value [80] of 0.767 eV, since the two LUMOs are accidentally degenerate. For **2**, the ΔLUMO value of 0.835 eV is larger than the 0.487 eV value predicted for ΔHOMO. This accounts for the plus-to-minus MCD sign sequence in ascending energy terms that is observed in the Q band region [16, 59, 82, 83]. However, although an analysis of the MCD spectrum of **1** points to a ΔHOMO value that is approximately the same or slightly larger than the ΔLUMO value, this trend was not reproduced in the MO calculations. The greater electronic absorption intensity of the Q_{y00} band of **1** relative to the Q_{x00} band was reproduced, however. It can be inferred from the results in Fig. 8a that the increase of ΔLUMO on going from compound **1** to **2** is significant since the MCD sign pattern changed in ascending energy terms from minus-to-plus in the case of **1** to plus-to-minus in the case of **2**.

We have successfully clarified the relationship between the electronic structures of azulene-fused porphyrins, **1-3**, and their spectral properties based on an analysis of the MCD spectral data in conjunction with the results of TD-DFT calculations. By fusing one or two azulene unit(s) to porphyrin, the ΔLUMO increased relative to ΔHOMO, and this was reflected on the sign pattern of the MCD spectra in the Q_{00} band region.

c) Detection of unusual ΔHOMO < ΔLUMO relationship in tetrapyrrolic cis- and trans-doubly N-confused porphyrins [81]

In normal D_{4h} or D_{4d} type metallo- and D_{2h} type metal-free porphyrinoids, generally ΔHOMO > ΔLUMO relationship exists, since some degenerate orbitals in a high-symmetry parent hydrocarbon perimeter are raised due to a structural perturbation. When the C_{16} axis of $C_{16}H_{16}^{2-}$ is replaced by a C_4 in the proper rotation axis in the context of D_{4h} or D_{4d} symmetry with respect to tetrapyrrolic porphyrins, only the degeneracy of MOs with M_L = odd number is retained, while that of those with M_L = even number is split. This outcome means that the LUMOs ($M_L = \pm5$) are degenerate, while the HOMOs ($M_L = \pm4$) are split [80]. Accordingly, the energy difference between the LUMO and LUMO+1 (ΔLUMO ~ 0) is always smaller than that between the HOMO and HOMO-1 (ΔHOMO). According to the widely accepted Gouterman's four- orbital theory explaining the electronic absorption spectra of porphyrins, the extent of ΔHOMO is manifested in the Q_{00} band intensity: the larger the ΔHOMO, the greater the intensity [80]. Using MCD spectroscopy, the ΔLUMO < ΔHOMO relationship appears as a minus-to-plus pattern in ascending energy [82, 83]. The theory of MCD spectra furthermore predicts that the sign pattern becomes plus-to-minus if ΔLUMO > ΔHOMO. Utilizing the high sensitivity of MCD spectroscopy, the electronic states of various porphyrins and Pcs have been successfully elucidated [16, 17]. Accordingly, we decided to apply MCD spectroscopy to core-modified N-confused porphyrins, which have become popular over the last 20 years, [84] due to their unique properties that are different from conventional porphyrins. Among these, the copper(III) complexes of *cis-* and *trans-* doubly N-confused porphyrins (*cis*-**1** and *trans*-**1**) (Fig. 9) [85, 86] have attracted our attention, since these complexes exhibit strongly perturbed absorption spectra with broad, red-shifted transitions which are not seen in standard tetrapyrrolic porphyrins. In order to gain an insight into the nature of N-confused porphyrin electronic systems, the location of the Q transitions of these porphyrins are assigned using MCD spectroscopy. The assignments are confirmed nicely

10

Изв. вузов. Химия и хим. технология. 2019. Т. 62. Вып. 4

by quantum chemical calculations. In particular, we found, on the basis of Michl's MCD theory [82, 83] that ΔLUMO is exceptionally larger than ΔHOMO, which is the opposite relationship to regular tetrapyrrolic porphyrins.
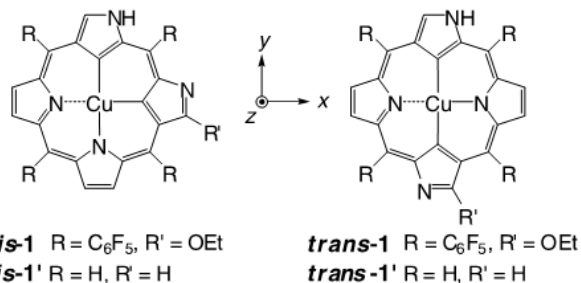

Fig. 9. Structures and abbreviations of *cis*- and *trans*-**1**, and structures used for calculation (*cis*- and *trans*-**1′**)

Рис. 9. Структуры и сокращения *цис*- и *транс*-**1**, а также структуры, использованные для расчета (*цис*- и *транс*-**1′**)

The electronic absorption and MCD spectra of *cis*-**1** (left) and *trans*-**1** are shown in Fig. 10. In contrast to regular metalloporphyrins which have an intense Soret band at around 400 nm and a weak Q band at around 550-600 nm, [80] both the doubly N-confused porphyrins exhibited strongly perturbed absorption spectra.
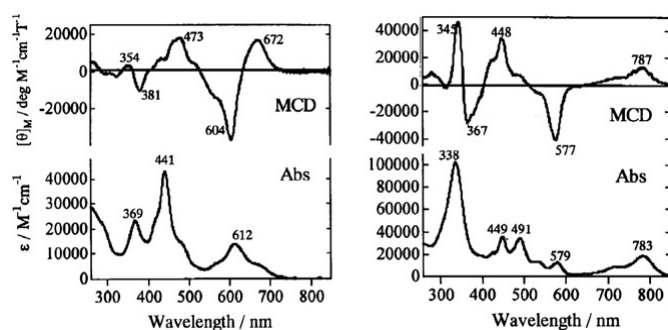

Fig. 10. MCD and electronic absorption spectra of *cis*-**1** (left) and *trans*-**1** (right) in CH_2Cl_2

Рис. 10. MCD и электронные спектры поглощения *цис*-**1** (слева) и *транс*-**1** (справа) в CH_2Cl_2

Comparing the longest wavelength components, *cis*-**1** has an absorption band at 612 nm with a shoulder on the longer side, while an absorption band is observed at an unusually long 783 nm for *trans*-**1**.

In the MCD spectra, relatively intense signals were observed for the lowest-energy transition reflecting large angular momentum properties. A positive/negative sign sequence with increasing energy was observed for the lowest-energy absorption band of *cis*-**1**. This sign pattern can be assigned to coupled Faraday B terms, which arise from magnetically induced mixing of nondegenerate excited states. Since the MCD peak positions (672 and 604 nm) are very close to the absorption shoulder (ca. 680 nm) and peak (612 nm),

there are at least two different electronic transitions in the 600-700 nm region of *cis*-**1**. In contrast, the MCD pattern associated with the lowest-energy transition of *trans*-**1** is similar in shape to the corresponding absorption bands, indicating the presence of a single Faraday B terms. In particular, a plus-to-minus MCD pattern in ascending energy strongly suggests that the unusual ΔHOMO < ΔLUMO relationship holds. A relatively intense MCD trough was observed at 577 nm. Since the MCD sign is opposite to that of the lowest-energy transition, the polarization of the 577 nm transition is different from that of the lowest-energy transition.

In order to assign the absorption bands, excitation energies and oscillator strengths of the doubly N-confused porphyrins without peripheral substituents (*cis*-**1′** and *trans*-**1′**) have been calculated using the CIS and TDDFT methods. As can be seen from Fig. 11, broad and red-shifted absorption bands are predicted. The *trans*-isomer has a longer wavelength absorption than the *cis*-isomer, in agreement with experiments.
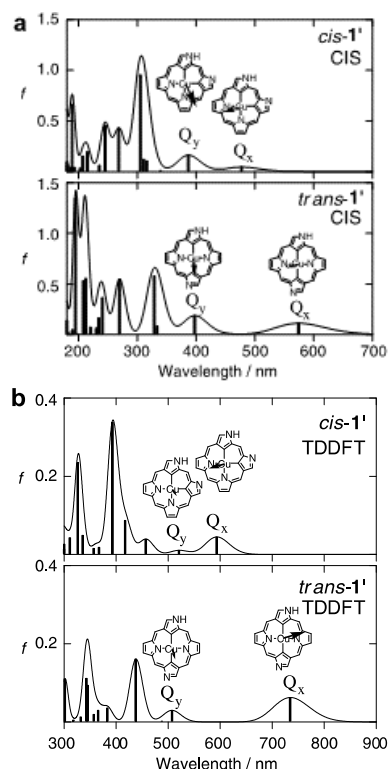

Fig. 11. Calculated transition energies and oscillator strength (f) for the doubly N-confused porphyrins without peripheral substituents (*cis*-**1′** and *trans*-**1′**): (a) CIS/6-31G(d) and (b) TDDFT (B3LYP/6-31G(d))

Рис. 11. Рассчитанные энергии перехода и сила осциллятора (f) для дважды N-спутанных порфиринов без периферических заместителей (*цис*-**1′** и *транс*-**1′**): (a) CIS / 6-31G (d) и (b) TDDFT (B3LYP / 6-31G (d))

To relate the spectroscopic properties to the molecular structures, a MO analysis was carried out.

Figure 12 shows a MO energy diagram and the frontier MOs of *cis*-**1**' and *trans*-**1**'. It can be noted that the appearance of the four frontier orbitals is similar to those of the normal porphyrin (**2**). Due to the large structural perturbation resulting from pyrrole inversions, the a_{1u}-type orbital and one of the e_g-type orbitals stabilize, while the a_{2u}-type and the other e_g-type orbital destabilize in the N-confused complexes. Essentially identical frontier orbitals and energy ordering were found even when including peripheral substituents.
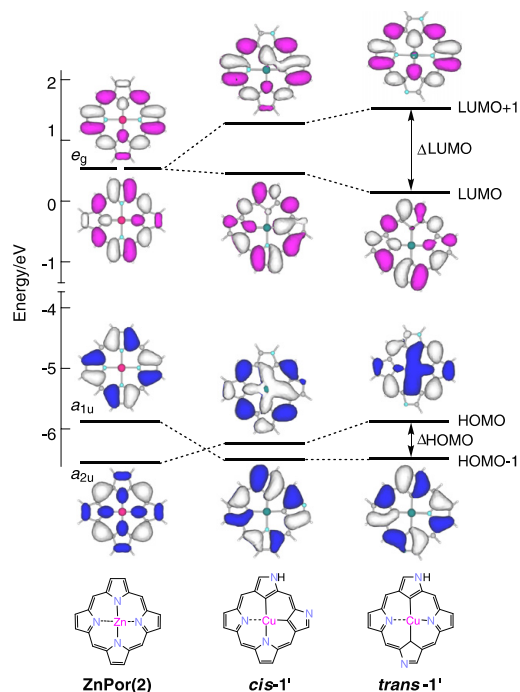

Fig. 12. Frontier molecular orbital diagram and contour plots of occupied and virtual orbitals of zinc(II) porphyrin with D_{4h} symmetry (**2**) and *cis*-**1**′ and *trans*-**1**′ obtained from the HF/6-31G(d) method
Рис. 12. Граница молекулярной орбитальной диаграммы и контурные графики занятых и виртуальных орбиталей цинкового (II) порфирина с симметрией D_{4h} (**2**) и *цис*-**1**′ и *транс*-**1**′, полученных по методу HF / 6-31G (d)

In order to gain an insight into the origin of the electronic structures of the N-confused porphyrin systems, Fig. 13 illustrates a schematic representation of the effect of inversion of the pyrrole rings on the four frontier orbitals. We consider that the pyrrole inversion only affects the location of the pyrrole nitrogen atom, because the MO coefficients essentially preserve the nodal properties upon inversion. Since a nitrogen atom is more electronegative than a carbon atom, the energy of the molecular orbitals having large coefficients on the nitrogen atoms is lowered. In the case of the a_{2u}-type orbital, the original porphyrin has relatively large coefficients on the pyrrole nitrogens. When a pyrrole ring is inverted, the size of the coefficient on the nitrogen becomes small, leading to destabilization of the orbital energy. In contrast, since there is a nodal plane on

the pyrrole nitrogen of the a_{1u} orbital, the MO energy of the N-confused porphyrins becomes lower than that of the porphyrin. When more pyrrole rings are inverted, this effect should be summed regardless of the *cis* or *trans* position. The perturbation to the unoccupied orbitals can also be discussed in a similar manner. The poprhyrin's LUMO (e_g-type orbital) is doubly degenerate by symmetry. As seen in Fig. 13, one of the e_g-type orbitals has a nodal plane on the nitrogen, while the other has coefficients on the nitrogen. The degeneracy is lifted upon inversion of the pyrrole ring, since stabilization and destabilization occur in the former and latter orbitals. It is noted that the effect of the perturbation to the LUMO in the doubly N-confused system depends on the position of inversion. In the case of the *cis*-isomer, an adjacent pyrrole ring is inverted, so that one ring destabilizes and the other ring stabilizes the MO energy upon inversion. On the other hand, the effect is summed in the *trans*-isomer. This results in a larger energy difference between the LUMO and LUMO+1 of the *trans*-isomer compared to that of the *cis*-isomer, which leads to a smaller HOMO–LUMO gap. Thus, this simple picture accounts well for the calculated MO features of the doubly N-confused porphyrins.
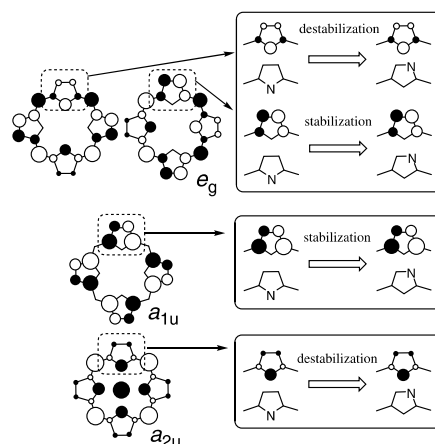

Fig. 13. Schematic representation of the perturbation of molecular orbitals by pyrrole inversion
Рис. 13. Схематическое представление возмущения молекулярных орбиталей пиррольной инверсией

Thus, using N-inverted porphyrins, we could prove experimentally and using MO calculations that the ΔHOMO < ΔLUMO relationship holds in their electronic structure.

d) Control of Chromophore Symmetry by Positional Isomerism of Peripheral Substituents [87]

Because Pc and TAP molecules are synthesized by tetramerization reactions of a phthalonitrile or fumaronitrile, a mixture of four positional isomers with C_{4h}, D_{2h}, C_{2v}, and C_s symmetry is obtained when unsymmetrically substituted precursors are used. In the

12

Изв. вузов. Химия и хим. технология. 2019. Т. 62. Вып. 4

case of substituents that introduce only a small perturbation into the π-conjugated systems of Pc and TAP, it is generally accepted that there is almost no difference in the absorption spectra of the four positional isomers. If substituents with sufficiently large perturbations are introduced in an unsymmetrical manner, in theory, chromophore symmetry can be controlled. TAP is more suitable for forming such systems than their Pc counterparts because the peripheral substituents are closer to the inner perimeter where most of the electron density of the frontier π molecular orbitals is found. On this basis, the key feature of the molecular design was the introduction of strongly perturbing push–pull substituents into TAP. Electron-donating amino and electron-withdrawing cyano groups were selected for this

purpose. Because TAPs are synthesized by tetramerization of fumaronitrile, substituted tricyanoethylene can provide the target TAP molecule and its positional isomers with C_{4h}, D_{2h}, C_{2v}, and C_s symmetry due to the arrangement of these substituents. The *tert*-butylamino group was selected as a push substituent with the aim of improving the solubility of the products. Since the Q band of regular porphyrin is weak, if this combination (cyano and amino groups) in TAPs having strong Q bands did not work, it appeared impossible to control the chromophore symmetry by positional isomerism of peripheral substituents in any other porphyrinoid systems. Scheme 3 shows the synthesis of push-pull TAP compounds.
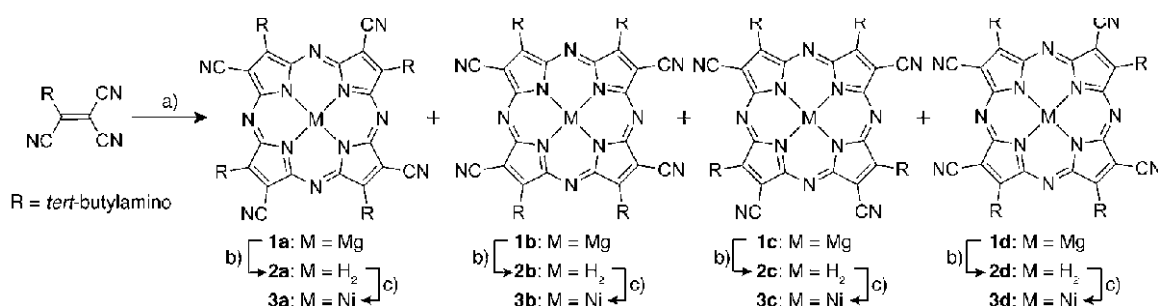
Scheme 3. Synthesis of the push–pull TAP compounds. Reagents and conditions: a) Mg(OC6H13)2, 1-hexanol, 180 °C, 3 h; b) CF3CO2H, CHCl3, 30 min; c) NiCl2·6H2O, DMF, 180 °C, 1 h
Схема 3. Синтез двухтактных TAP-соединений. Реагенты и условия: a) Mg (OC6H13) 2, 1-гексанол, 180 ° C, 3 ч; b) CF3CO2H, CHCl3, 30 мин; c) NiCl2 · 6H2O, ДМФА, 180 ° C, 1 час
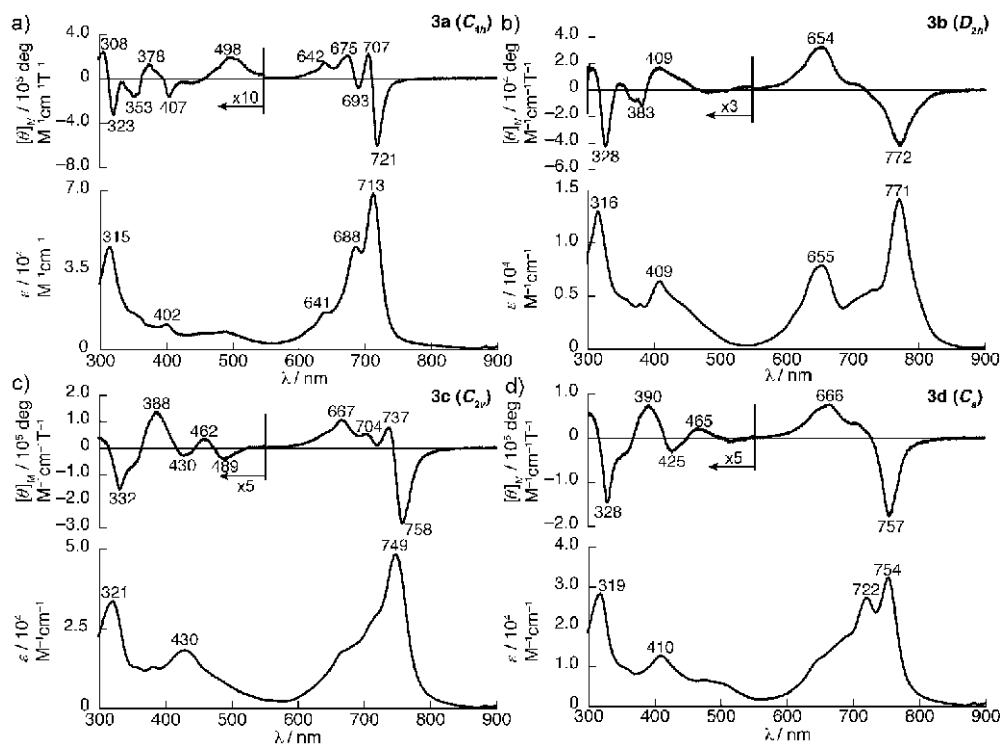

Fig. 14. UV/Vis absorption (bottom) and MCD (top) spectra of a) **3a**, b) **3b**, c) **3c**, and d) **3d** in CHCl3, except for **3b** in pyridine
Рис. 14. Ультрафиолетовое / видимое поглощение (внизу) и MCD (вверху) спектры a) **3a**, b) **3b**, c) **3c** и d) **3d** в CHCl3, за исключением **3b** в пиридине

Isomeric structures were determined by using NMR and occasionally single crystal X-ray data. Here, we show the relationship between the spectroscopic properties and isomeric structures using Ni complexes, i.e. **3a** (C_{4h}), **3b** (D_{2h}), **3c** (C_{2v}), and **3d** (C_s).

The absorption spectra of **3a-3d** are collected in Fig. 14. The absorption spectra of **3a** and **3c** show a single intense Q band at 713 and 749 nm, respectively, with shoulders on the high-energy side due to the presence of vibronic bands. In contrast, there is a marked splitting of the Q bands of **3b** and **3d**. Their x- and y-polarized components lie at 771 and 655 nm, and 754 and 722 nm, respectively. The splitting energy of the Q-band absorptions of **3b** is greater than that of **3d**.

In the MCD spectrum of **3a**, a derivative-shaped Faraday A term is observed with a trough and peak at 721 and 707 nm, respectively, with the crossover point corresponding to the center of the Q-band absorption. This is the pattern that is anticipated due to the degeneracy of the $\pi\pi*$ excited states of **3a** [16, 22, 30, 39, 71, 80]. Similarly, a derivative-shaped Faraday A terms is observed in the Q-band region of **3c** with a trough and peak at 758 and 737 nm, respectively. Due to the lack of three-fold or higher molecular symmetry in **3c**, this signal is assigned as a pseudo-Faraday A terms, which can be observed when molecules possess accidentally nearly degenerate excited states [16, 17, 22, 38, 45, 59]. On the other hand, **3b** and **3d** exhibit Faraday B terms at 772 and 654 nm (**3b**) and at 757 and 666 nm (**3d**) with a minus-to-plus sign sequence in ascending energy that corresponds to the split Q-band absorption. These MCD spectra indicate contributions of nondegenerate excited states to these Q-band absorptions.

To carry out an in-depth analysis of the electronic structures, molecular orbitals (MOs) and transition energies were calculated for the nickel complexes of the push–pull TAPs (**3a–d**) by using DFT and TDDFT methods. Calculations were also performed on unsubstituted nickel complex **4** and the C_{4h}-symmetric positional isomers of nickel complexes with four *tert*-butylamino or cyano substituents (**5** and **6**) as model compounds. Relative to the unsubstituted TAP **4**, the HOMO and degenerate LUMO of **6** are stabilized due to the presence of pull substituents (Fig. 15). The extent of the stabilization appears to be greater for the LUMO (1.46 eV) than for the HOMO (1.33 eV).

On the other hand, the HOMO and LUMO of **5** are both destabilized, with the destabilization being more significant for the HOMO (1.67 eV) than for the

LUMO (1.10 eV). The shift in the energies of the frontier MOs of the push–pull TAP **3a** relative to those of **4** is due to the synergetic effects of the push–pull substituents, and this causes the marked redshift of the Q bands of **3a–d**. The differences observed in the Q-band regions of the push–pull TAPs can be directly related to the differences in the relative energies of the frontier π-MOs, which are predicted to provide the largest contributions to the Q band transition. As has been demonstrated in the electronic structures of porphyrinoids, a 16-atom 18π electron $C_{16}H_{16}^{2-}$ cyclic perimeter is used to describe the optical properties based on the $M_L = \pm 4$ and ± 5 nodal patterns of the HOMO and LUMO, respectively, and this can also be regarded as the parent perimeter for the push–pull TAP molecules. The D_{16h} symmetry of the perimeter model is first perturbed to form the D_{4h} symmetry of the TAP structure, and is then further modified to form the respective lower symmetries of **3a–d** due to the significant perturbations introduced by the push–pull substituents. The same nodal pattern sequences can still be clearly observed in the frontier MOs shown in Fig. 16. Evidence for the retention of the perimeter model properties can be obtained experimentally based on a relative intensification of the MCD signals in the Q-band region due to the $\Delta M_L = \pm 9$ properties.
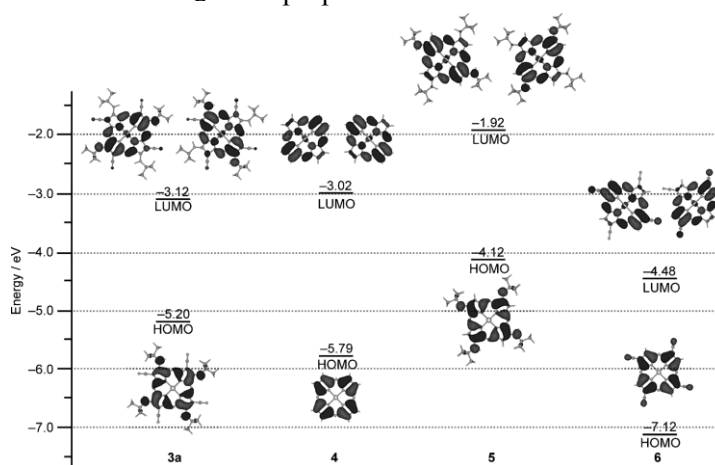

Fig. 15. Partial molecular orbital energy diagrams of **3a**, **4**, **5**, and **6** (B3LYP/6-31G(d))

Рис. 15. Диаграммы парциальной молекулярной орбитальной энергии **3a**, **4**, **5** и **6** (B3LYP / 6-31G (d))

Taking particular note of the nodal planes through the *meso*-nitrogen atoms of the degenerate LUMO of **3a** and the LUMO and LUMO+1 of the other isomers, it can be readily demonstrated that these MOs vary only with respect to differences in conjugation along the x and y axes. The energy diagrams of the excited states can be explained by considering the interactions of the push–pull substituents with the differing nodal patterns of the LUMO and LUMO+1. In the

cases of **3a** and **3c**, the push and pull substituents cause a destabilization and stabilization of the orbital energies, respectively, and equally perturb the excited state to result in the degenerate and nearly degenerate excited states of **3a** and **3c**, respectively. On the other hand, the push–pull substituents in **3b** and **3d** do not equally perturb the LUMO and LUMO+1, causing significant energy difference between these MOs (the ΔE_{LUMO} value). The smaller ΔE_{LUMO} value of **3d** is related to the lower molecular symmetry of **3d**. The TDDFT results reproduce the observed single and split Q-band absorptions as would be anticipated on this basis.
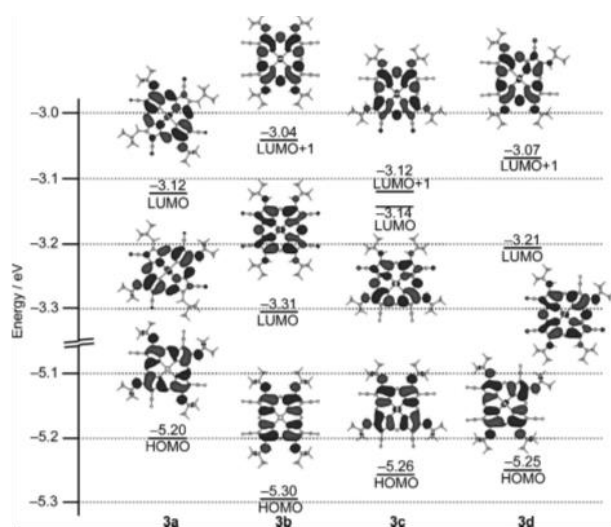

Fig. 16. Partial molecular orbital energy diagrams of **3a–d** (B3LYP/6-31G(d))

Рис. 16. Диаграммы парциальной молекулярной орбитальной энергии **3a–d** (B3LYP / 6-31G (d))

As seen in Fig. 14, the absorption spectra of isomeric tetraazaporphyrinoids which differ in the position of push-pull substituents could be explained nicely by concept and theoretical calculations. This type of data might be difficult to obtain in other systems such as regular porphyrins and Pcs, since the Q band of the former is essentially forbidden and therefore very weak and the substituent effect is weak in the latter.

e) Phosphorus(V) Tetraazaporphyrins: Porphyrinoids Showing an Exceptionally Strong CT Band between the Soret and Q bands [88]

More than a quarter century ago, it was reported that the absorption spectra of tetra-*tert*-butylated and octa-phenylated MgTAPs differ in the band position and intensity and even in shape slightly [89]. Namely, both the Q and Soret bands of the latter is a few times stronger than that of the former, and a small band appears at the longer wavelength side of the Soret band of the latter. Since phenyl groups is considered to be an electron-donor, we inferred that this small band may be a CT from phenyl groups to the TAP core. If

this is the case, the CT band may shift to longer wavelength with concomitant increase in intensity by introducing electron-rich element on the phenyl groups and more positive element in the center of the TAP skeleton, since the CT transition becomes easier. From this concept, we inserted P(V) ion in the center of the TAP skeleton and OMe, *tert*-butyl, F, and CF$_3$ groups at the *para*-positions of eight phenyl groups of octaphenyltetraaaporphyrin (Fig. 17), and examined whether this is true or not [88].
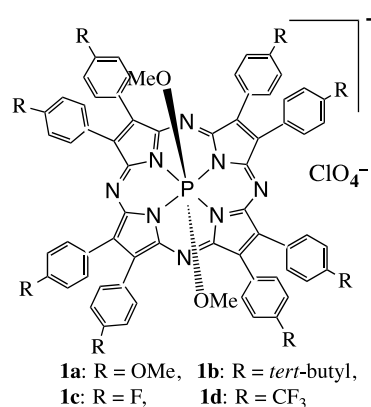

1a: R = OMe, **1b**: R = *tert*-butyl,
1c: R = F, **1d**: R = CF$_3$

Fig. 17. Octaphenyl P(V)TAPs substituted at the *para*-positions of phenyl groups

Рис. 17. Октафенил Р (V) ТАП, замещенный в *пара*-положениях фенильных групп

Compounds **1a-d** were prepared from the corresponding Mg complex after demetallation by acid. For the introduction of a phosphorus ion into the center of the TAPs, phosphorus oxybromide was used as a precursor. At the end of the reaction, the reaction mixture was quenched with dichloromethane/methanol, which provided dimethoxy-substituted (as axial ligand) P(V)TAPs. Finally, the counter anion was replaced by excess NaClO$_4$. Figure 18 shows the electronic absorption spectra of **1a-d**, together with that of octa-*p*-(*tert*-butyphenyl) MgTAP. The UV-vis spectrum of MgTAP **2a** is characteristic of metallated TAPs with D_{4h} symmetry, and as reported previously, a weak band appeared at ca. 460 nm (Fig. 18, bottom). Interestingly, the absorption envelope of P(V)TAP **1a** is quite different from that of the Mg complex **2a**. A Q band-like absorption was observed at 664 nm, and the phosphorus(V) ion assisted slightly to shift the position of the Q band. The envelope of the Soret band resembles that of the Mg complexes, with a peak appearing at 342 nm. However, a broad, intense absorption band appeared between the Soret and Q bands at 534 nm only for P(V)TAP. Therefore, **1a** can absorb across the entire UV-visible region (in particular, the absorption coefficient is more than $2 \cdot 10^4$ M^1 cm^1 across 500-700 nm in CH$_2$Cl$_2$) as a single chromophore. The color of a solution of **1a** in dichloromethane is purple rather than the typical green color of aryl-substituted free-base and

metallated TAPs. The absorption band at 534 nm cannot, of course, be assigned to the Q band, and its position is close to that of a CT transition in **2a**, but the apparent intensity is about 2-4 times stronger. Similarly, **1b-d** having different *para*-substituents also showed intense CT-like bands between the Q and Soret regions, indicating that the central phosphorus ion enhances the substituent effect even though the substituents are located at the para positions of the phenyl groups, outside the π-conjugation system of the TAP.
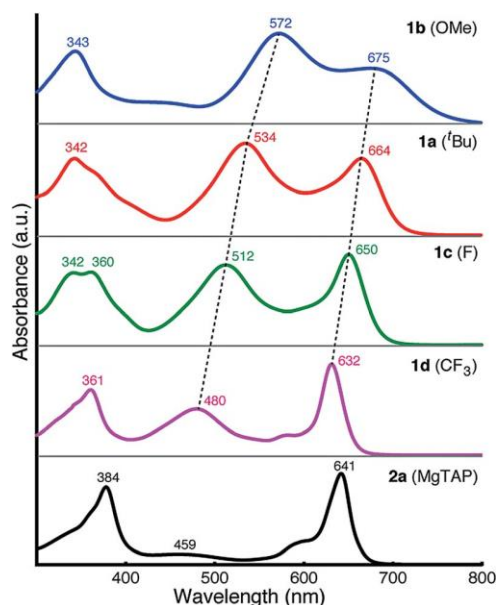

Fig. 18. UV-vis absorption spectra of **1a–d** and **2a** in CH_2Cl_2
Рис. 18. Ультрафиолетовые спектры поглощения **1a – d** и **2a** в CH_2Cl_2

The difference of the CT-like bands between electron-withdrawing (CF_3, **1d**) and electron-donating (OMe, **1b**) groups (92 nm, 3400 cm^{-1}) was larger than that of the Q bands (43 nm, 1000 cm^{-1}). The small difference for the Q band suggests that the peripheral substituents only marginally affect the electronic structure of the HOMO and LUMO. On the other hand, the peaks at around 550-450 nm apparently contain a transition associated with the aryl moiety, since they change in both intensity and position depending on the substituents at the *para* positions of the phenyl groups, suggesting that they are CT bands between the aryl moiety and the TAP core. P(V)TAPs **1a–b** containing electron-donating groups have a Q-band intensity smaller than that of the CT bands, whereas P(V)TAPs **1c–d** containing electron-withdrawing groups display the opposite absorption properties, where the intensity of the Q bands are larger than the CT bands. For example, in the case of the CF_3-substituted P(V)TAP **1d**, the Q band is sharp and intense, whereas the CT band is relatively small, resembling that of typical metallo-TAPs (i.e. **2a**). Since similar phenomena were ob-

served in the case of tetraazachlorin–fullerene conjugates [90], the electronic communication between the peripheral aryl moieties and the P(V)TAP core was inferred to be altered by the substituents.
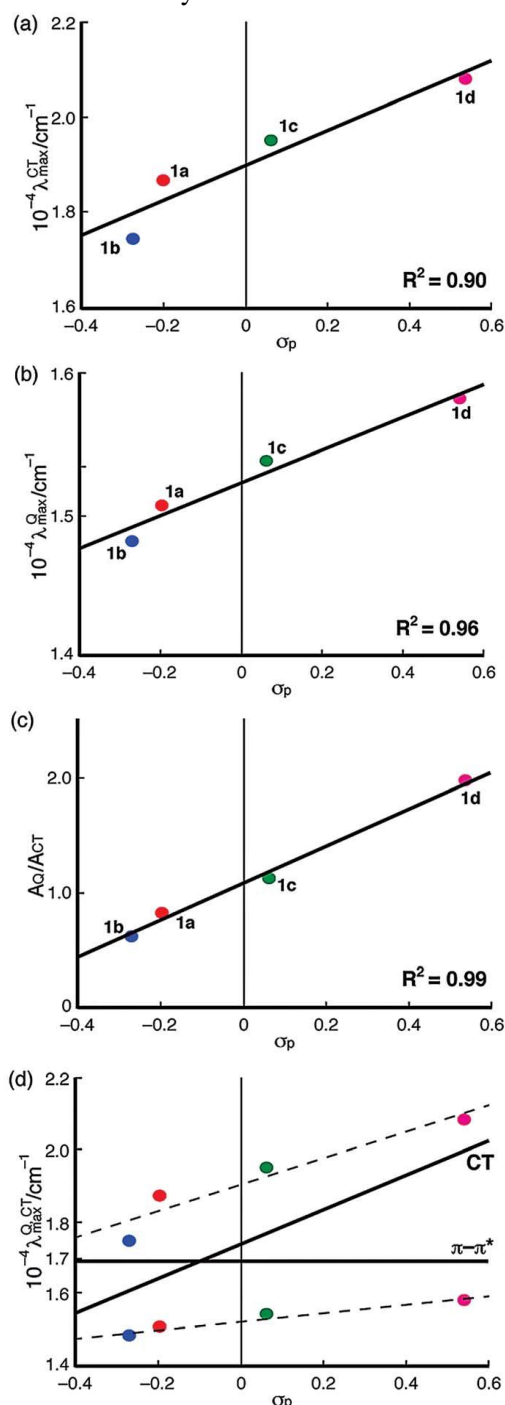

Fig. 19. Plots of (a) position of the CT bands, (b) position of the Q bands, and (c) ratio of A_Q to A_{CT} versus Hammett σ-values derived from the P(V)TAPs. (d) Configuration interaction diagrams for the CT and Q transitions
Рис. 19. Графики (a) положения полос CT, (b) положения полос Q и (c) отношения AQ к ACT по сравнению со значениями σ Хаммета, полученными из P (V) TAP. (d) Конфигурационные диаграммы взаимодействия для переходов CT и Q

More interestingly, both the position and intensity of the peaks of P(V)TAPs exhibit a noteworthy correlation with the Hammett σ_p value of substituents on the aryl moieties (Fig. 19). Plots of the position of both the Q- and the CT-like bands versus the Hammett σ_p value of the substituents constitute a straight line for **1a-d**. Plots of the ratio of the intensity of the Q bands to that of the CT bands versus the Hammett σ_p value of the substituents also constitute a good straight line.
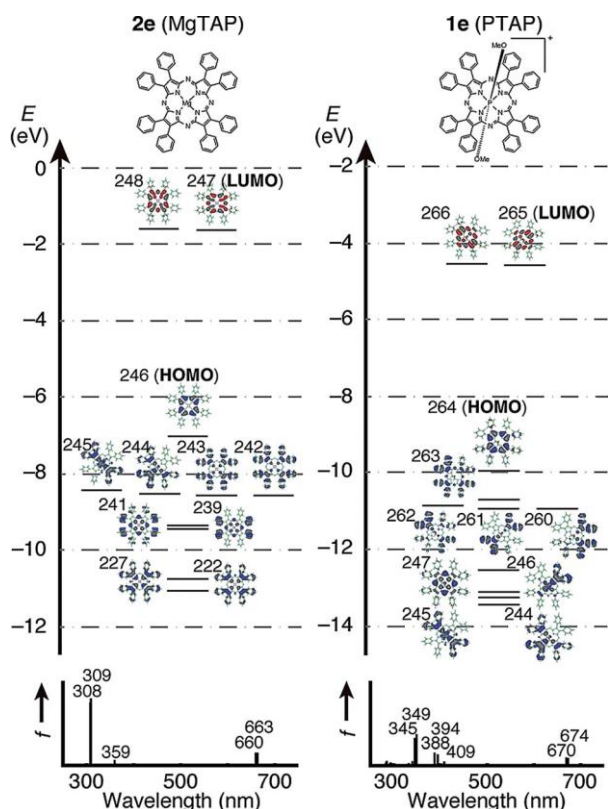

Fig. 20. Partial molecular energy diagram and orbitals of Ph₈P(V)TAP (**1e**) and Ph₈MgTAP (**2e**) (top) and their calculated absorption spectra (bottom). Calculations were performed at the LC-BLYP/6-31G*//B3LYP/6-31G* level

Рис. 20. Диаграмма парциальной молекулярной энергии и орбитали Ph₈P (V) TAP (**1e**) и Ph₈MgTAP (**2e**) (вверху) и их рассчитанные спектры поглощения (внизу). Расчеты проводились на уровне LC-BLYP / 6-31G * // B3LYP / 6-31G *

Partial MO energy diagrams of the model structures are shown in Fig. 20. For both TAPs, the HOMO, LUMO, and LUMO+1 are dominated by the TAP orbitals, and these orbitals corresponded to the a_{1u}-, e_{gy}-, and e_{gx}-like orbitals in Gouterman's model [80], respectively. Therefore, these calculated transitions at 674 and 670 nm (for P(V)TAP **1e**) and 663 and 660 nm (for MgTAP **2e**) can be assigned to the experimental Q bands. In the UV region of the calculated spectrum of **2e**, two close, intense bands were obtained at 309 and 308 nm, energetically comparable to the observed Soret bands. These bands are composed of transitions from the HOMO-1, HOMO-2, HOMO-3, HOMO-4, HOMO-5, and HOMO-7 to the LUMO and

LUMO+1 (almost degenerate), and particularly from the HOMO-1 to the degenerate LUMOs. The HOMO-1 to HOMO-7 are delocalized over the entire complex, indicating that the intramolecular charge transfer (CT) transitions including the phenyl (or aryl) moiety are not negligible for these bands. However, the TAP moiety of the HOMO-1, HOMO-5, and HOMO-7 originate from the a_{2u}-type orbitals. The band calculated at 359 nm is relatively weak, composed of transitions from the HOMO-1 to HOMO-7, HOMO-19, and HOMO-24 to the degenerate LUMOs. The HOMO-19 and HOMO-24 are partially localized on the lone pairs of the *meso*-nitrogens, supporting the conclusion that these transitions have some $n–\pi^*$ transition character. This assignment and the weak band of **2a** at 459 nm is therefore assigned ambiguously to an $n–\pi^*$ transition. The aryl moieties also contribute to these bands, and the contribution of the CT transition is crucial for the intensity of this band.

The introduction of the phosphorus(V) ion into the TAP center stabilizes all of the MOs, but does not affect the symmetry of the HOMO, LUMO, and LUMO+1. The calculated HOMO–LUMO energy gap of P(V)TAP **1e** is similar to that of MgTAP **2e**, so that we can infer that the position of the Q band of **1a** changes slightly when the P(V) ion is introduced. In the region between 450 and 350 nm, the calculated transitions (409, 403, 394, and 388 nm) of **1e** are more complex than those of **2e**. The MCD spectrum of **1a** was quite complicated at around 500 nm (not shown), whereas that of **2a** showed a clear Faraday A term at 509 and 444 nm. Thus, these experimental differences appeared to be reproduced by this calculation on **1e**, due perhaps to the deformation of the macrocycle and/or a weak interaction between P(V) and the TAP core. These transitions comprise the $n–\pi^*$ transitions and CT transitions, as mentioned for the magnesium complex **2e**. Moreover, these bands were estimated to be stronger than those of **2e** in the longer wavelength region. The contribution of the HOMO-1 to HOMO-4 dominates, and as can be judged from the size of the coefficient of MOs in Fig. 20, the MOs are mainly localized on the peripheral phenyl groups. These results reproduce clearly the experimental absorption spectrum of **1a**, where the intense CT band appears in the longer wavelength region compared to **2a**. In other words, the absorption features of **1e** can be interpreted as typical metalloTAPs, but the position and intensity of the CT bands have been markedly altered after the introduction of the P(V) ion.

Finally, the relationship between the CT and Q bands theoretically interpreted. Here, if we accept the above MO calculation results (Fig. 20) and experimental data shown in Figs. 18 and 19, we can consider as follows. The Q excited state is of E_u symmetry (we use the notation of D_{4h} symmetry). The CT excited

state appears to be also of E_u symmetry, since the CT transitions are mostly from a_{1u}- and a_{2u}-type orbitals delocalized over the whole molecule, including the phenyl groups, to the TAP-centered e_{gx} and e_{gy} orbitals, leading to two E_u excited states. Thus, the Q and CT transitions can arise from configuration interaction between a CT state and a π-π* state. In order to show this, we have plotted, in Fig. 19d, the CT and Q band position, together with the estimated energy of the pure π-π* state (horizontal continuous line) and the hypothetical CT state (continuous straight line of unit slope). If these states mix through configuration interaction, the experimental points should lie on the broken lines. The points in Fig. 19d appear to be consistent with this model. The positions of the straight lines are only guesses, but the overall picture seems to be essentially correct.

Based on the combination of spectroscopic and theoretical results, the effect of the P(V) ion in the TAP was found to be an enhancement of a CT band between the Soret and Q bands, without perturbing the π-conjugated system of the TAP. Thus, our conjecture that the CT band of octaphenylated MgTAP may be shifted to longer wavelength and intensified by inserting more positive central element was correct. The P(V)TAPs can absorb light across the entire UV-vis region, while the position and intensity of these absorption envelopes can be tuned rationally.

f) Modulation of the Molecular Spintronic Properties of Adsorbed Copper Corroles [91]

Molecular pintronics is an emerging research field, in which organic molecules are placed between electrodes, and the electron conductance is controlled by the free circulation of the electron spin of a single molecule [92-94]. The modulation of conductance through molecules in this manner has been demonstrated by molecular-level scanning tunneling microscopy (STM) measurements of Kondo resonance signals, which are associated with the exchange coupling between the unpaired spins of the paramagnetic molecules and the conduction band electrons of the metal substrate. For example, when porphyrinoids were adsorbed on metal surfaces, the unpaired π-orbitals of metal complexes tend to play an important role in spin-sensitive electron transfer, because π-radical orbitals are delocalized and can be coupled more efficiently with the conduction band [95, 96]. Corroles are porphyrin analogues with a direct pyrrole–pyrrole link, which can stabilize higher oxidation states of the coordinated transition metal ions. In recent decades, there has been extensive research on corrole complexes, since the ligands may have a non-innocent character in which a one-electron dianionic radical rather than the

normal closed-shell trianion binds to the central metal [97]. Copper corroles stand out as the most notable in this regard [97-100]. It has been demonstrated that considerable electron density can flow into the copper $3d_{x2-y2}$ orbital from the HOMO of the corrole ligand π-system; this specific d–π interaction can lead to a saddling distortion that is observed in both X-ray crystal and DFT-optimized structures [99]. Since the spin states of copper corroles are determined by the d–π interaction, special attention has been paid to how the spin-state properties can be modulated by modifying the corrole ligand. Accordingly, we demonstrated that a triplet ground state can be switched on in a manner that may be suitable for spintronics by introducing fused benzene rings on the corrole periphery, and that the spin properties are further modulated on the Au(III) substrate by a rotation of the *meso*-aryl groups [91]. A bicyclo[2.2.2]octadiene (BCOD)-fused copper corrole (Cu-BCOD) has been prepared, which can readily be converted into a tetrabenzocorrole (Cu-Benzo) in quantitative yield by heating in vacuo (Fig. 21). A copper 5,10,15-triphenylcorrole (Cu-TPC) has also been prepared so that the effect of fused-ring-expansion on the Kondo resonance signals can be readily analyzed.
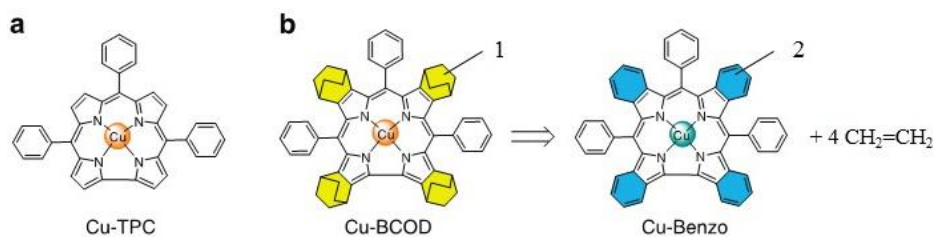

Fig. 21. (a) Structure formula of Cu-TPC. The orange ball represents the central Cu(III) ion. (b) Cu-BCOD was converted into Cu-Benzo via a retro-Diels–Alder reaction during a sublimation process with the extrusion of ethylene molecules. The dark-green ball represents the central Cu(II) ion. The BCOD and Benzo moieties are highlighted in yellow (1) and blue (2), respectively (Fig. 21 in color see http://journals.isuct.ru/ctj/article/view/1061)

Рис. 21. (a) Структурная формула Cu-TPC. Оранжевый шар представляет собой центральный ион Cu (III). (b) Cu-BCOD был превращен в Cu-бензо посредством реакции ретро-Дильса-Альдера во время процесса сублимации с экструзией молекул этилена. Темно-зеленый шар представляет собой центральный ион Cu (II). Части BCOD и Benzo выделены желтым (1) и синим (1) цветом соответственно (Рис. 21 в цвете смотри http://journals.isuct.ru/ctj/article/view/1061)

The molecule was transferred to a Au(III) substrate using a sublimation method under ultra-high vacuum conditions, by heating the sample in a Ta boat at ~300 °C During the sublimation process, Cu-BCOD was converted into the Cu-Benzo molecule via a retro-Diels–Alder reaction involving the extrusion of four ethylene molecules from the fused BCOD rings as shown in Fig. 22b. This was confirmed by time-of-flight (TOF) secondary ion mass spectrometry (MS). In contrast, the sublimation of Cu-TPC resulted in no

18

Изв. вузов. Химия и хим. технология. 2019. Т. 62. Вып. 4

molecular decomposition. An STM image of an isolated Cu-Benzo molecule adsorbed on Au(III) (Fig. 22a) exhibits three characteristic protruded areas together with a square-like region. The STM image simulations were calculated for a sample bias voltage of -0.8V (Fig. 22b), using a Vienna *Ab initio* Simulation Package (VASP)-optimized molecular structure (Fig. 22c). The simulation image contains three protruded spots similar to those observed in Fig. 22a. The distance between the two bright spots in Fig. 22a is ~13.0 Å, which is close to the separation of the centers of the *meso*-aryl rings of 12.6 Å shown in Fig. 22c. In the rest of the molecule, a square-like protruded area can be identified, which is similar to that observed in the STM image. Each protruded spot has a node in the middle.

However, the node is not visible in the observed STM image. This discrepancy may be related to a tilting of the phenyl rings upon adsorption. The aryl ring marked A in Fig. 22a will be referred to as the y-axis *meso*-aryl rings, while the other two will be referred to as the x-axis *meso*-aryl rings. In contrast, Cu-TPC molecules form a chain on the Au(III) surface. In the unit cell marked by the white square, two Cu-TPC molecules rotated by 180° with respect to each other (see Fig. 22d). The optimized model structure is shown in Fig. 22f together with a simulated STM image for a bias voltage of -0.8V (Fig. 22e), which indicates that three *meso*-aryl rings appear protruded as is also observed for Cu-Benzo molecules.
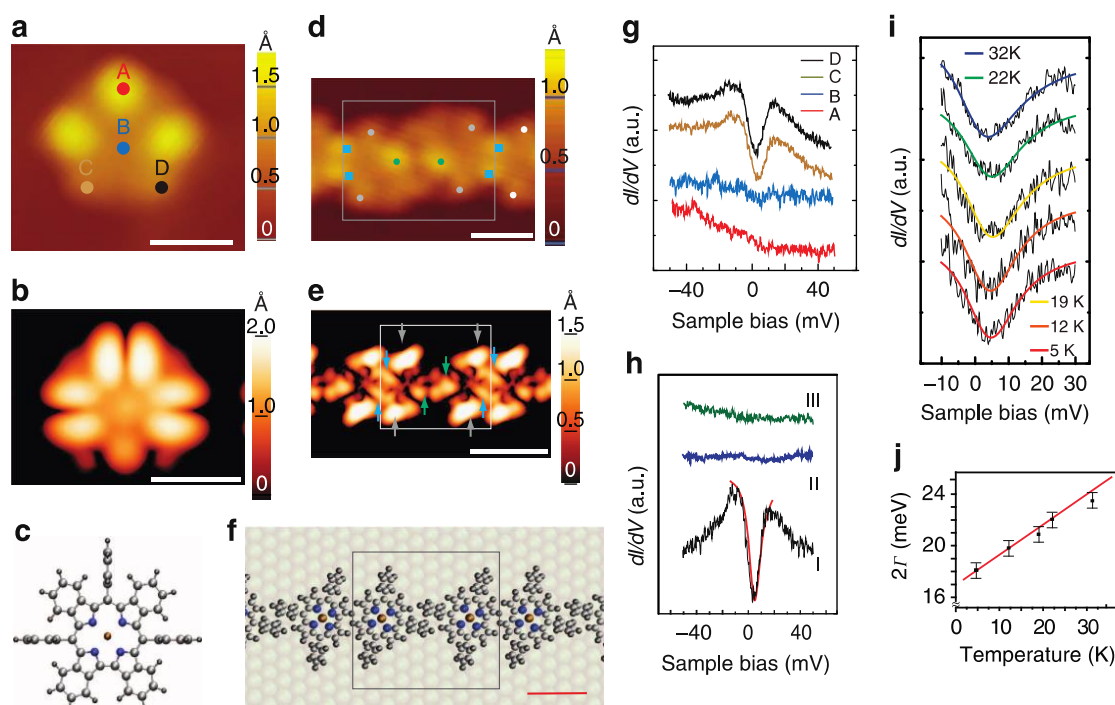

Fig. 22. STM image and Kondo resonance of Cu-TPC and Cu-Benzo. (a) STM topographic image, (b) simulated STM image and (c) optimized structural model of Cu-Benzo monomer on Au(111). Corresponding tunneling conditions of V_{sample} = -0.8 V and I_{tunnel} = 0.3 nA. Scale bars, 10 Å and color scales indicate height information. In c, large (small) grey spheres represent C (H) atoms, while blue and gold spheres correspond to N and Cu atoms, respectively. (d–f) Same as a–c but for a Cu-TPC chain on Au(111) surface. The box indicates the unit cell that appears periodically in the chain. Prominent features are marked by dots in d, whose corresponding protrusions in the simulation are shown by arrows with the same color. The color scheme of atoms in f is same as that in c. (g) dI/dV spectra obtained for Cu-Benzo monomer at positions A–D in a. (h) Comparison of the dI/dV spectra at the ligand positions of Cu-Benzo on Au(111) (I, black), on Cu(111) (II, blue) and Cu-TPC on Au(111) (III, green). Red curve in i shows the result of the Fano fitting. (i) Temperature dependence of the Fano dip of Cu-Benzo measured in the temperature region of 4.7–32 K. (j) Width of the dip at half maximum (2G) versus temperature for the Kondo dip near the Fermi level. The solid curve indicates the fitted curve. The error bars were estimated by measuring the scattering of the data in the heat cycles repeated eight times (Fig. 22 in color see http://journals.isuct.ru/ctj/article/view/1061)

Рис. 22. СТМ-изображение и резонанс Кондо для Cu-TPC и Cu-Benzo. (a) топографическое изображение СТМ, (b) моделируемое изображение СТМ и (c) оптимизированная структурная модель мономера Cu-бензо на Au (111). Соответствующие условия туннелирования V_{sample} = -0,8 В и I_{tunnel} = 0,3 нА. Шкала, 10 Å и цветовая шкала указывают информацию о высоте. В с большие (маленькие) серые сферы представляют атомы C (H), тогда как синие и золотые сферы соответствуют атомам N и Cu соответственно. (d – f) то же, что и a–c, но для цепи Cu-TPC на поверхности Au (111). Поле указывает на элементарную ячейку, которая периодически появляется в цепочке. Характерные черты отмечены точками на d, соответствующие выступы в симуляции показаны стрелками того же цвета. Цветовая схема атомов у f такая же, как у c. (g) спектры dI / dV, полученные для Cu-бензо мономера в положениях A – D в a. (h) Сравнение спектров dI / dV в положениях лигандов Cu-бензо на Au (111) (I, черный), на Cu (111) (II, синий) и Cu-TPC на Au (111) (III) зеленый). Красная кривая в i показывает результат подгонки Фано. (i) Температурная зависимость провала Фано для Cu-Benzo, измеренная в области температур 4,7–32 К. (j) Ширина провала на половине максимума (2G) в зависимости от температуры для провала Кондо вблизи уровня Ферми. Сплошная кривая показывает подогнанную кривую. Столбики ошибок были оценены путем измерения рассеяния данных в циклах нагрева, повторенных восемь раз (Рис. 22 в цвете смотри http://journals.isuct.ru/ctj/article/view/1061)

The spin states of Cu-Benzo and Cu-TPC molecules were investigated by detecting the Kondo resonance using STM. The Kondo effect is caused by the interaction between the conduction band electrons and localized spins [101]. The Kondo resonance appears in the scanning tunneling spectroscopy (STS) spectrum near the Fermi level either as a sharp peak or dip, which is determined by the Fano resonance effect-type interference between the tunneling electron [102]. The STS spectra obtained for Cu-Benzo molecule at the A–D positions (Fig. 22a) are provided in Fig. 22g. At positions A and B, on the y-axis *meso*-aryl ring and the central Cu atom, no STS features are observed. In contrast, spectra obtained at positions C and D of the corrole ligand show signals at the Fermi level, whose narrow width and shape are consistent with a Kondo dip feature. The peak-width change with sample temperature (see Fig. 22i,j) was examined to prove that the zero-bias peak originates from Kondo resonance. The peaks are fitted with the Fano functions, the result of which is shown as solid curves in Fig. 22j. An examination of the peak width shows clear variation with sample temperatures. The observed data (solid circles) were successfully fitted using this formula. The fitted curve is shown in Fig. 22j as a solid line, which gives $T_K \sim 105K$. This is consistent with the assignment of the zero-bias peak to Kondo resonance [101]. The STS spectrum measured for Cu-TPC exhibits no Kondo feature at the ligand position (III of Fig. 22h). This indicates the absence of molecular spin and provides direct spectroscopic evidence for the singlet ground state. When electron paramagnetic resonance (EPR) spectra were measured, Cu-TPC and Cu-BCOD were found to be EPR silent, as would be anticipated for a Cu(III) singlet ground state, while the EPR spectrum of Cu-Benzo in frozen CHCl₃ exhibits a highly distinctive Cu(II) dimer signal [103, 104]. Thus, experimentally, the oxidation state of Cu in Cu-TPC and Cu-BCOD was found to be +3, while that in Cu-Benzo +2.

To examine electronic and spin states more precisely, geometry optimizations and calculation of electronic states were carried out for singlet and triplet ground states of Cu-TPC, Cu-BCOD and Cu-Benzo using the hybrid B3LYP functional with 6–31G(d) basis sets. As anticipated, the singlet ground state was predicted to be more stable for Cu-TPC and Cu-BCOD (by 0.4 and 2.6 kcal·mol⁻¹, respectively), but not for Cu-Benzo (by 5.1 kcal·mol⁻¹). For all three complexes, the geometry of the singlet ground state is predicted to be significantly more saddled than the triplet states in a manner that is consistent with Kahn's concept of orthogonal magnetic orbitals [105]. The theory is generally based on the symmetry of the orbitals on the metal and the ligand that contain unpaired electrons. In a planar structure, the metal orbital is strictly orthogonal to the ligand π-radical orbital and this results in an S = 1 triplet state. On the other hand, when the orbitals of the metal and ligand are not strictly forbidden by symmetry and hence partially overlap, as in a saddled structure, there is antiferromagnetic coupling resulting in an S = 0 singlet state, which cannot be distinguished from dative bond formation. This concept can be applied to metallocorroles as well due to the similar frontier π-MOs in shape [97]. Almost all of the crystal structures that have been reported for copper corroles have saddled conformations due to the d–π interaction [106]. For Cu-Benzo, however, a planar conformation is observed in the crystal structure.

When the B3LYP-optimized structures are compared with the crystal structures by the displacements of the 23 core ligand atoms, the saddling conformation of the Cu-TPC macrocycle can be clearly observed in the edge-on view, similar to the optimized structure for the singlet ground state as shown in Fig. 23a. Interestingly, the asymmetric unit cell of Cu-Benzo contains two molecules with different conformations. One has a saddled structure, which also closely matches the optimized singlet structure (Fig. 23b), whereas the other one adopts a planar conformation that overlaps perfectly with the optimized triplet structure. The crystal and optimized structures of the planar conformation of Cu-Benzo are essentially identical, including that of the three *meso*-aryl groups (Fig. 23e). The *meso*-aryl groups of Cu-Benzo are almost perpendicular to the mean corrole plane with an average dihedral angle of 82.9° (Fig. 23d), while the dihedral angle for Cu-TPC is only 48.8° (Fig. 23c). The spin density plots for the planar triplet state (Fig. 23f) demonstrate that there is ferromagnetic coupling between the copper $3d_{x2-y2}$ orbital and the benzocorrole π-orbital. There is almost no spin density on the *meso*-aryl groups, since they lie orthogonal to the corrole plane.

Copper corroles represent an unusual exception among metallocorroles, because saddled structures have been a shared feature of all of the complexes reported to date, even in the absence of steric crowding at the ligand periphery. It has been widely accepted that copper corroles are saddled, since there is an energetically favorable $3d_{x2-y2}$ and ligand π–HOMO interaction. Upon fused-ring-expansion to form Cu-Benzo, however, there are significant changes in the relative energies of the frontier MOs in a manner that discourage overlap between the $3d_{x2-y2}$ orbital of the metal ion and the occupied frontier π-orbital, which has large MO coefficients on the pyrrole nitrogens, and this favors a planar conformation.

20

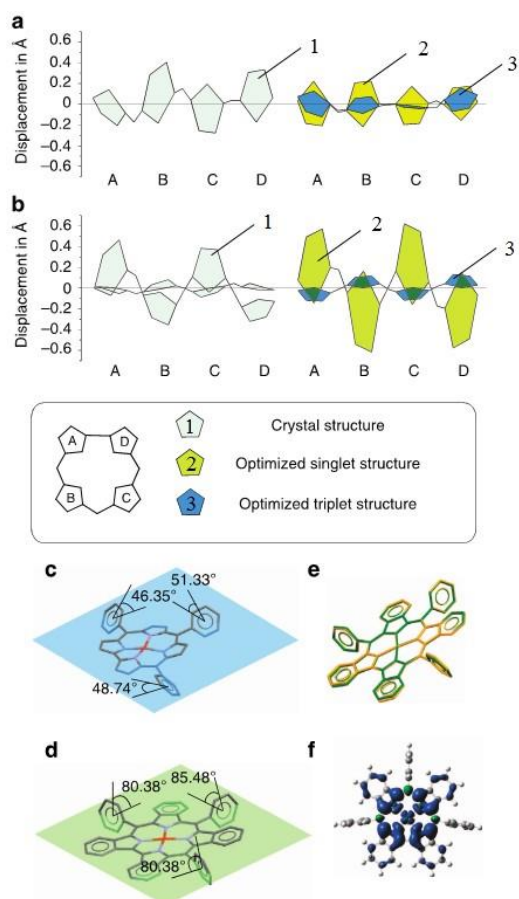Изв. вузов. Химия и хим. технология. 2019. Т. 62. Вып. 4

Fig. 23. Comparison and analysis of the crystal and optimized structures. (a) The distortions of Cu-TPC and (b) Cu-Benzo in the crystal and B3LYP-optimized structures are compared. The displacements from the mean plane of the 23 ligand atoms are illustrated in clothes-line diagrams. The four pyrrole moieties are labelled as A, B, C and D. The colored pyrrole moieties represent crystal structure (1), optimized singlet structure (2) and optimized triplet structure (3). The dihedral angles between meso-aryl groups and 23 ligand atoms' least square planes (the colored plane) in the crystal structures of Cu-TPC (c) and planar Cu-Benzo (d). (e) Overlay of planar crystal (green) and B3LYP-optimized triplet structure (yellow) of Cu-Benzo. (f) Spin density plot of Cu-Benzo for the S = 1 triplet state (isospin = 0.001), calculated with B3LYP/6–31G(d) level of theory (Fig. 23 in color see http://journals.isuct.ru/ctj/article/view/1061)

Рис. 23. Сравнение и анализ кристаллических и оптимизированных структур. (a) Сравнение искажений Cu-TPC и (b) Cu-бензо в кристаллической и B3LYP-оптимизированной структурах. Смещения от средней плоскости 23 атомов лиганда показаны на диаграммах бельевой веревки. Четыре пиррольных фрагмента обозначены как A, B, C и D. Цветные пиррольные фрагменты представляют собой кристаллическую структуру (1), оптимизированную синглетную структуру (2) и оптимизированную триплетную структуру (3). Двугранные углы между мезоарильными группами и плоскостями наименьших квадратов 23 атомов-лигандов (цветная плоскость) в кристаллических структурах Cu-TPC (c) и плоских Cu-Benzo (d). (e) Наложение плоской кристаллической (зеленой) и оптимизированной по B3LYP триплетной структуры (желтой) Cu-Benzo. (f) График спиновой плотности Cu-Benzo для триплетного состояния S = 1 (изоспин = 0,001), рассчитанный на уровне теории B3LYP / 6–31G (d) (Рис. 23 в цвете смотри http://journals.isuct.ru/ctj/article/view/1061)

As has been reported previously, the frontier π-MOs of corroles are very similar to the a_{1u}, a_{2u} and e_g frontier π-MOs of porphyrins, despite the loss of one *meso*-carbon atom on the inner ligand perimeter. Thus a perimeter-model approach can be adopted to study trends in their energies [83]. Michl referred to the two frontier MOs derived from the HOMO and lowest unoccupied molecular orbital (LUMO) of the parent perimeter in which angular nodal planes lie on the y-axis as the **a** (a_{1u}) and **-a** (e_{gy}) MOs, while those which lie on antinodes are referred to as the **s** (a_{2u}) and **-s** (e_{gx}) MOs [82, 83, 107, 108]. For Cu-TPC, saddling enables the **s** MO with large MO coefficients on the pyrrole nitrogens to mix significantly with the $3d_{x2-y2}$ orbital of the central metal, so that the electron spins are paired. This overlap can be seen in the angular nodal patterns of the HOMO and LUMO of Cu-TPC in Fig. 24a. The electronic structure of Cu-Benzo (Fig. 24b,d) is predicted to be markedly different from that of Cu-TPC (Fig. 24a,c), since the triplet state is predicted to be more stable than the corresponding singlet state. The α-spin **a** MO is the singly occupied molecular orbital (SOMO), since its energy is higher than that of the α- and β-spin **s** MO (Fig. 24d). This can be attributed to a destabilization of the energy of **a** MO due to the antibonding effect of fused-ring-expansion on the π-system. The β-spin **a** MO is unoccupied and hence is the LUMO of Cu-Benzo (Fig. 24d). The macrocycle is oxidized to form a corrolate π-cation radical with an unpaired spin and a central Cu(II) ion.

The theoretical considerations discussed above can account for the experimental observation of the Kondo resonance. For the Cu-TPC molecule, it is predicted that the ligand π-orbital is paired and no Kondo resonance is formed, which agrees with the absence of the Kondo feature for this molecule. For the Cu-Benzo molecule, a ground state is calculated, which is consistent with the observation of the Kondo resonance measured at the corrole ligand position. The SOMO level can be attributed to the spin impurity of Kondo resonance. It could be argued that the partial filling of the SOMO level may be due to charge transfer from the Au(III) substrate as is the case with CuPc and NiPc on Ag(III) [109].

In summary, fused-ring-expansion of the corrole ligand has been demonstrated to result in a unique spin state, in a manner that could lead to applications in molecular spintronics. When the Cu-BCOD molecules were sublimed onto the Au(III) surface from a heated Ta boat, they were converted into Cu-Benzo molecules in quantitative yield by a retro-Diels–Alder reaction. The destabilization of the **a** MO of Cu-Benzo results in a planar structure and the oxidation of the ligand leads to the formation of an uncoupled spin and hence a triplet ground state.
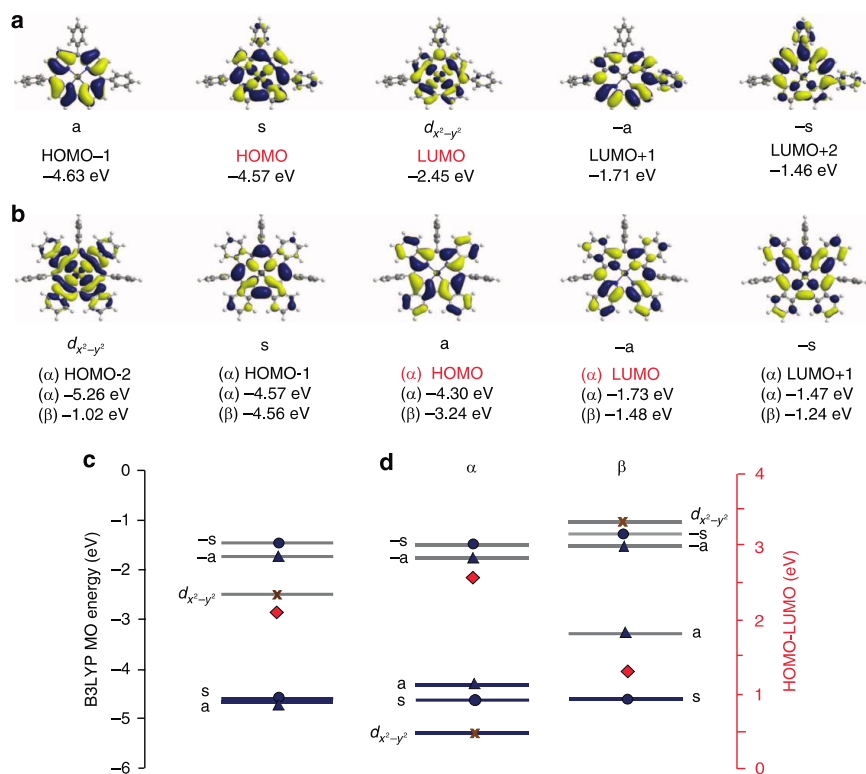
Fig. 24. Contour plots and energy levels of the B3LYP-optimized structures. (a,b) Frontier MO contour plots and corresponding energy values of Cu-TPC (a) and Cu-Benzo (b). Michl's **a**, **s**, **-a** and **-s** nomenclature is used to describe the frontier π-MOs with $M_L = \pm 4$ and ± 5 nodal patterns. (c,d) Schematic energy diagram of the frontier MOs of Cu-TPC (c) and Cu-Benzo (d). Occupied and empty MOs are highlighted with blue and grey lines, respectively, and blue circles, triangles and brown crosses are used to denote the **s** and **-s** MOs, **a** and **-a** MOs and the d_{x2-y2} MOs, respectively. The predicted HOMO–LUMO gaps are denoted with red diamonds and are plotted against a secondary axis (Fig. 24 in color see http://journals.isuct.ru/ctj/article/view/1061)

Рис. 24. Контурные графики и энергетические уровни структур, оптимизированных по B3LYP. (a, b) Границы МО граничного контура и соответствующие значения энергии Cu-TPC (a) и Cu-бензо (b). Номенклатура Michl **a**, **s**, **-a** и **-s** используется для описания пограничных π-МО с ML = ± 4 и ± 5 узловыми схемами. (c, d) Схематическая энергетическая диаграмма пограничных МО Cu-TPC (c) и Cu-Benzo (d). Занятые и пустые МО выделяются синими и серыми линиями соответственно, а синие кружки, треугольники и коричневые кресты используются для обозначения МО и **s**, **-s**, МО и МО и d_{x2-y2} соответственно. Предсказанные промежутки HOMO – LUMO обозначены красными бриллиантами и нанесены на график относительно вторичной оси (Рис. 24 в цвете смотри http://journals.isuct.ru/ctj/article/view/1061)

2-2. Non-Planar Deformed Systems

a) Deformed Phthalocyanines: Synthesis and Characterization of Zinc Phthalocyanines Bearing Phenyl Substituents at the 1-, 4-, 8-, 11-, 15-, 18-, 22-, and/or 25-Positions [110]

In 2001, we reported on a highly deformed α-octaphenylated H_2Pc and H_2TAP [111]. However, at that time, the relationship between deformation and spectroscopic and electrochemical properties could not be studied since Pc compounds with lesser number of phenyl groups could not be prepared. In 2005, we succeeded in preparing Pcs containing two, four, and six phenyl groups at what we call α-positions and systematically examined these relationship [110]. Figure 25 shows the chemical structures of the six ZnPcs prepared for this study, of which compounds **3** and **4** contain four phenyl groups and are positional (geometrical) isomers. These compounds were all characterized by NMR and X-ray crystallography.

Figures 26 and 27 depict colormap analyses [112] of the extent of ring deformation. The displacements of the ligand atoms are calculated relative to the 4N-plane generated by the four pyrrole nitrogens on the inner ligand perimeter. Figure 27 confirms this observation. As expected, **5** and **6** have highly deformed structures at neighboring isoindole units where two phenyl groups overlap. In particular, the structure of **6** is similar to that of H_2PcPh_8, where alternating up and down displacements of the isoindole units results in a saddled structure [111]. The maximum deviation of the pyrrole β-carbon atom is about 1.18 Å for **6** (Fig. 27), which is comparable to that in H_2PcPh_8, while those of near-planar Pcs are within about 0.15 Å. The deviation is somewhat less for **5**, amounting to 0.76 Å at the site with largest deviation and 0.34 and 0.69 Å at sites adjacent to this. Although the structures of **5** and **6** are in line with what was anticipated, the crystal structure of adjZnPcPh$_4$ (**4**) is not. **4** maintains a relatively high degree of planarity in the crystalline state (Figs. 26 and 27), despite the existence of phenyl overlaps.
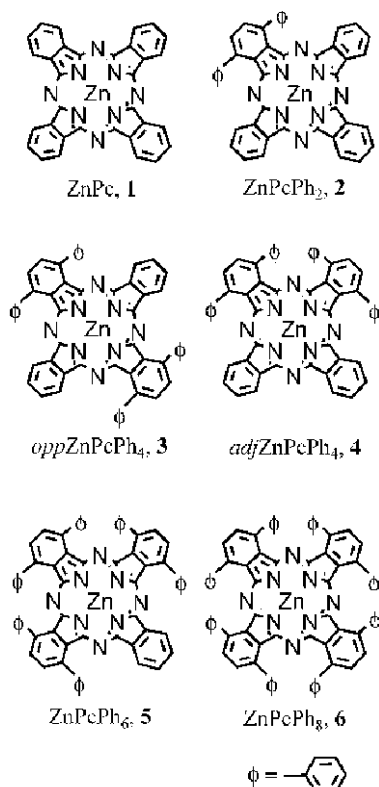
Fig. 25. Six ZnPcs containing various numbers of phenyl groups at α-positions

Рис. 25. Шесть ZnPcs, содержащих различное количество фенильных групп в α-положениях

Fig. 27. Linear display of the out-of-4N-plane deviations from planarity for the core atoms of **2**, **4**, **5**, and **6** from top to bottom, respectively. Crystal data are shown in the left-hand column, and optimized geometry data in the right-hand column. The squares indicate carbon atoms bearing phenyl substituents. The *meso*-nitrogen atoms are shown by empty circles

Рис. 27. Линейное отображение отклонений вне плоскости 4N от плоскостности для атомов ядра **2**, **4**, **5** и **6** сверху вниз, соответственно. Кристаллические данные показаны в левом столбце, а оптимизированные геометрические данные - в правом столбце. Квадраты обозначают атомы углерода, содержащие фенильные заместители. Атомы *мезо*-азота показаны пустыми кружками
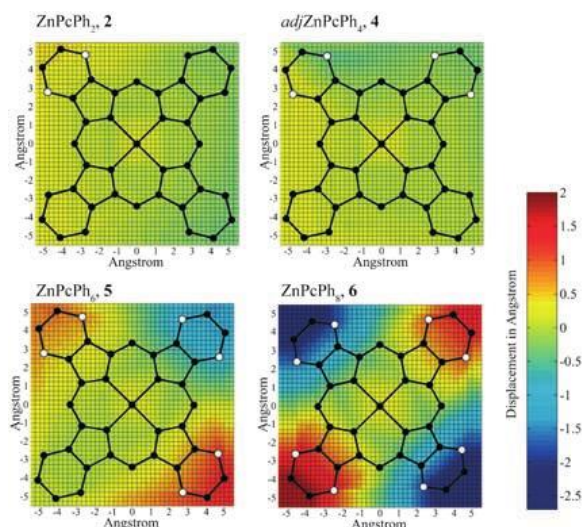

Fig. 26. Colormap analyses of the crystal structures of **2**, **4**, **5**, and **6**. Hydrogen atoms and peripheral and axial substituents are omitted for clarity. White marks indicate phenyl-substituted carbon atoms (Fig. 26 in color see http://journals.isuct.ru/ctj/article/view/1061)

Рис. 26. Анализ цветовой карты кристаллических структур **2**, **4**, **5** и **6**. Атомы водорода и периферические и осевые заместители для ясности опущены. Белые отметки указывают на фенилзамещенные атомы углерода

The color map analysis of **4** resembles that of **2** (Fig. 26). Figure 27 demonstrates that **4** takes on a ruffled rather than a saddled structure, in which the *meso*-nitrogen atoms lie outside the 4 N-plane. DFT geometry
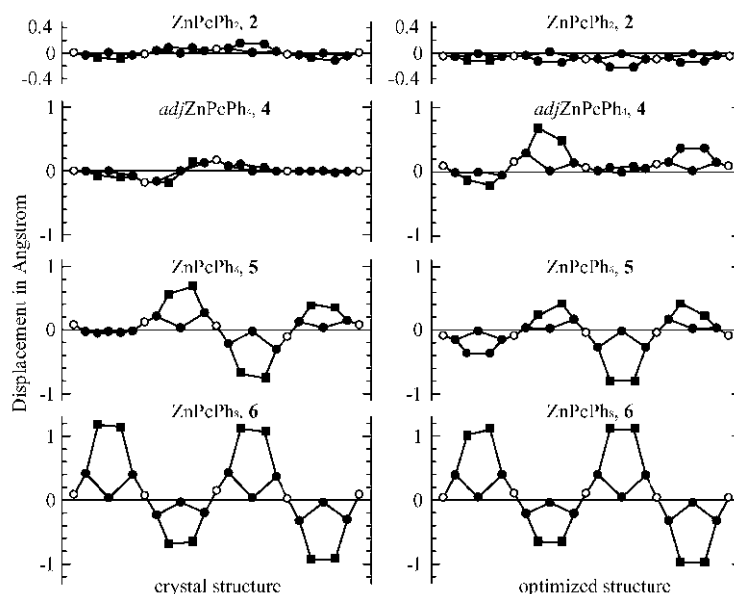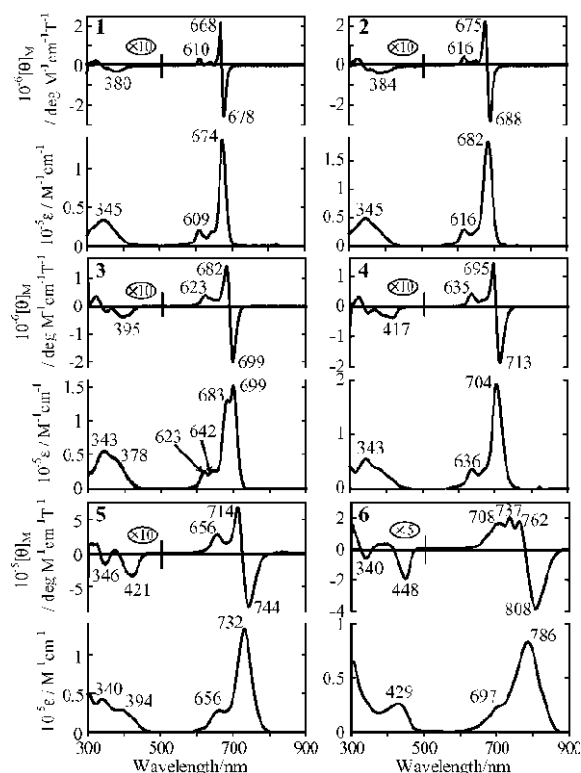

Fig. 28. Absorption and MCD spectra of **1–6** in pyridine

Рис. 28. Спектры поглощения и MCD спектры **1–6** в пиридине

optimizations were conducted for **2, 4, 5**, and **6** using the B3 LYP functional with 6–31 G(d) basis sets, with the results illustrated in the right-hand column of Fig. 27. The nonplanarity of **5** observed in the X-ray crystal data (Fig. 27) indicates that the phenyl-substituted sites deviate significantly from planarity and that the non-substituted isoindole is near-planar.

Figure 28 shows the absorption and MCD spectra of **1–6** in pyridine. The wavelength data are tabulated in Table. All of the complexes, with the exception of **3**, exhibit an intense, unresolved, Q-band in the 650-850 nm region, which shifts to the red as the number of phenyl groups is increased. **1** has a sharp Q-band at 674 nm and the corresponding MCD signal is a typical derivative-shaped Faraday A term, while near-planar phenyl-substituted **2** and **3** show slightly red-shifted Q-bands relative to **1**.

The Q-band shifts are summarized in Fig. 29a. The Q-band of **3** splits into two components. The splitting is less than 350 cm^{-1}, so the corresponding MCD signal can be regarded as a pseudo A-term.

Taking the midpoint of the split Q-band as the Q-band energy of **3**, the Q-band shifts from **1** to **2** and from **2** to **3** are around 170 and 190 cm^{-1}, respectively. The substituent effect of the phenyl groups clearly shifts the Q-band slightly to the red [113]. Partial peripheral substitution usually results in an approximately linear shift of the Q-band energies as the number of substituents is increased [114, 115]. It should be noted that although both **3** and **4** contain four phenyl groups, the Q-band of **4** occurs at longer wavelength, by about 270 cm^{-1}. Figure 29a demonstrates that linearity is only valid for the relatively planar **1–3**, and that marked deviations from linearity are observed for the deformed complexes **4–6**. The shift increases to around 270, 540, and 940 cm^{-1} for **3→4**, **4→5**, and **5→6**. The Q-band shift increases for **4**, **5**, and **6** are therefore primarily due to the increasing ligand folding.

In the Soret band region (ca. 300–450 nm) of **1–3**, one broad band is observed at around 345 nm, accompanied by a less intense, somewhat complex set of MCD signals. In addition, a characteristic band appears at around 400 nm for nonplanar Pcs (i.e., **4–6**), with the band at 429 nm for **6** being especially prominent. The origin of these bands is ascribed to the HOMO→LUMO+3 transition, which is parity-forbidden for planar D_{4h} complexes but becomes allowed when ring deformation removes the center of symmetry [116, 117].
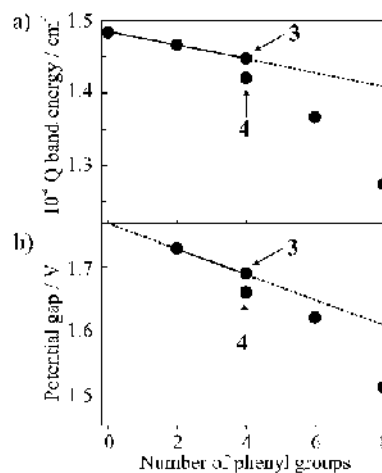

Fig. 29. a) Transition of the Q-band energy with respect to the number of phenyl substituents. b) Potential gaps
Рис. 29. a) Переход энергии Q-полосы по отношению к числу фенильных заместителей. b) Потенциальные щели

It is well established that the HOMO and LUMO energies of Pc derivatives correlate well with their first oxidation and reduction potentials [118-120]. The redox potential data of **1-6** in o-dichlorobenzene (o-DCB) are plotted in Fig. 30.

Compound **1** is too insoluble in o-DCB for satisfactory voltammograms to be obtained. Two oxidation and reduction couples were observed for all of the other compounds, with **5** and **6** giving significantly more distinct redox curves in the oxidation region compared to near-planar **2–4**, since aggregation is probably accelerated upon oxidation for the less substituted Pcs. From the differences between the various redox potentials, all processes are clearly one-electron and can be assigned to either ring oxidation or ring reduction, since Zn^{II} does not undergo redox processes within this

Table. The absorption and MCD data of 1-6 in pyridine
Таблица. Абсорбция и MCD данные для 1-6 в пиридине

Compound	Absorption[a]			MCD[b]			
ZnPc, 1	345 (0.33)	609 (0.20)	674 (1.35)	380 (−0.03)	610 (0.33)	668 (2.15)	678 (−2.55)
ZnPcPh$_2$, 2	345 (0.48)	616 (0.29)	682 (1.82)	384 (−0.04)	616 (0.49)	675 (2.18)	688 (−2.78)
oppZnPcPh$_4$, 3	343 (0.47)	378 (0.42)	623 (0.21)	395 (−0.03)	623 (0.32)	682 (1.19)	699 (−1.71)
	642 (0.22)	683 (1.10)	699 (1.29)				
adjZnPcPh$_4$, 4	343 (0.54)	636 (0.35)	704 (1.92)	417 (−0.04)	635 (0.43)	695 (1.43)	713 (−1.85)
ZnPcPh$_6$, 5	340 (0.43)	394 (0.28)	656 (0.27)	346 (−0.02)	421 (−0.03)	656 (0.27)	714 (0.66)
	732 (1.33)			744 (−0.78)			
ZnPcPh$_8$, 6	429 (0.26)	697 (0.21)	786 (0.83)	340 (−0.01)	448 (−0.04)	708 (0.16)	737 (0.20)
				762 (0.17)	808 (−0.38)		

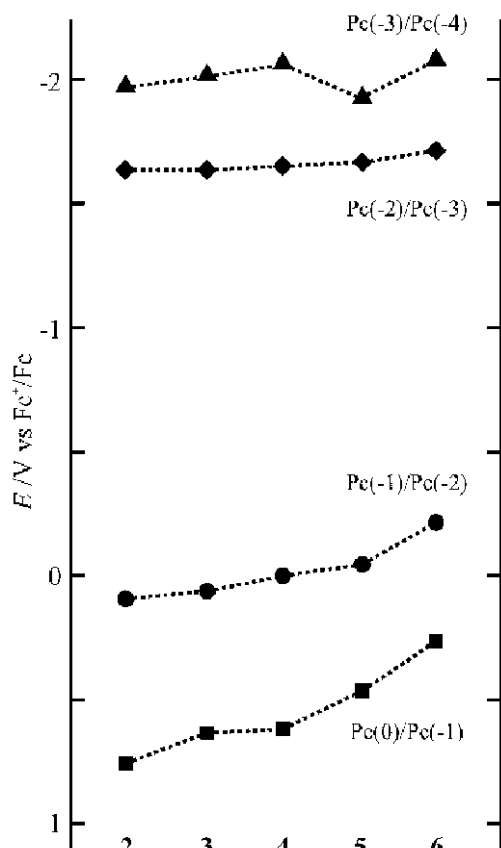[a] λ [nm] (10^{-5}ε [dm^{3}mol^{-1}cm^{-1}]). [b] λ [nm] (10^{-6}[q]$_M$ [deg dm^{3}mol^{-1}cm^{-1}T^{-1}]).

Fig. 30. Electrochemically obtained redox data of **2–6** in o-DCB
Рис. 30. Электрохимически полученные редокс-данные для
2–6 в o-DCB

6, but the second reduction potentials do not shift from ligand to ligand. The relationship between the number of phenyl substituents and the Q-band energies and potential gaps between the first oxidation and reduction couples is shown in Fig. 29. Clearly, there is a close relationship between the Q-band energy and potential gap, since both values decrease as the number of phenyl groups is increased. Linearity is maintained only for the planar derivatives, however, with the nonplanar complexes showing significant deviations from the trend. The potential gap of **4** is smaller than that of **3**, as was observed in the analogous Q-band energy values. Thus, the electrochemical results confirm that molecular deformation causes significant destabilization of the HOMO energies, a consequence of which is the bathochromic shifts of the Q-band.

In order to enhance the interpretation of the above spectroscopic and electrochemical properties, the molecular orbital and excitation energies were calculated using the ZINDO/S method. The Q band of **1** was predicted in the visible region (ca. 720 nm), composed mainly of HOMO-LUMO transitions (ca. 90%). The lowest-energy bands (the Q-bands) of **6** are calculated to lie at 788 and 781 nm, while the experimentally observed wavelength is 786 nm. The Q-band energy increases with decreasing number of phenyl groups: 747 and 741 nm and 733 and 728 nm for **5** and **4**, respectively. These are also in close agreement with the experimental values (732 and 704 nm for **5** and **4**, respectively). Similarly to **1**, the HOMO→LUMO transitions account for about 90% of the Q-band excited state in the CI calculations for **2–6**, which indicates that the ring deformations do not significantly change the composition of the Q-band.
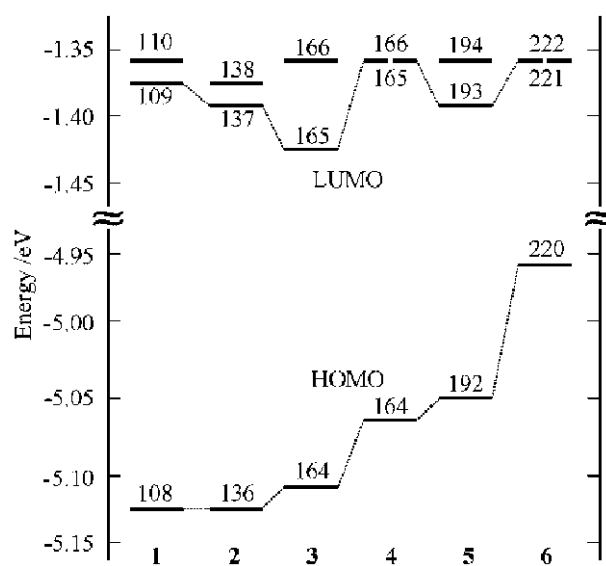
potential window [121]. In the case of fused-ring expanded Pcs, including naphthalocyanines and anthracocyanines, the HOMO energies increase with decreasing Q-band energies, while the LUMO energies remain relatively stable [30]. A similar trend is observed for compounds **2–6**, where the first oxidation potential shifts negatively, while, in contrast, the first reduction potential does not shift appreciably from complex to complex. The first oxidation potentials are +0.10 and -0.20 V (versus Fc$^+$/Fc) for **2** and **6**, respectively, indicating destabilization of the HOMO by 0.30 V. The first reduction potentials shift to the negative by only 0.08 V on going from **2** to **6**. As a consequence, the energy gap between the first oxidation and reduction potentials decreases from 1.73 to 1.51 V on going from **2** to **6**, as would be anticipated given the observed red-shift of the Q-band. On going from **2** to **3**, the first oxidation potential shifts by 0.04 V, while the first reduction potential remains almost identical (-1.63 V versus Fc$^+$/Fc), which indicates that the phenyl groups also cause a slight destabilization of the HOMO levels, although the ring deformation effects are much more significant. As shown in Fig. 30, the second oxidation potentials also shift to the negative on going from **2** to

Fig. 31. Frontier MO energy diagram for **1-6**
Рис. 31. Граница МО энергетической диаграммы для **1-6**

Izv. Vyssh. Uchebn. Zaved. Khim. Khim. Tekhnol. 2019. V. 62. N 4

25

Figure 31 shows the frontier MO energy diagram of **1–6**. Since both the LUMO and LUMO+1 orbitals contribute significantly to the Q-bands, the average energy of the LUMO and LUMO+1 levels should be regarded as the LUMO energy during analysis of the impact of trends in the HOMO-LUMO gaps on the absorption spectra. The energy gap between the HOMO and "midpoint" LUMO levels is 3.77, 3.75, 3.72, 3.71, 3.67, and 3.60 eV for **1–6**, respectively. The same trend is observed in the Q-band energies as phenylation increases on going from **1** to **6**. It should be noted that the LUMO and LUMO+1 energies split even in the case of **1** because of the presence of the axial pyridine ligand. The largest splitting was calculated for **3** and the second largest for **5**, reflecting the lower symmetry of the phenyl substitutions in these complexes. Unlike the LUMO energy, the LUMO+1 energies do not shift markedly from complex to complex. The Q-band of **6***(* means phenyl-removed structure) was calculated to lie at 783 nm, which is close to the wavelength calculated for **6** (788 nm), suggesting that the presence of the phenyl groups has only a limited effect on the Q-band energy. Similar results were obtained for **2–5**, with the lowest energy bands appearing almost at identical positions for the phenyl-substituted and unsubstituted derivatives. For example, the lowest-energy bands for **2–5** were calculated to lie at 729, 736, 733, and 747 nm, respectively, and those for **2***–**5*** at 723, 723, 730, and 747 nm, respectively. This result can be understood by considering the distribution of the nodal patterns of the HOMO, LUMO, and LUMO+1. As depicted in Fig. 32, the nodes of these three MOs are localized on the Pc ligand rather than the phenyl groups. Therefore, the destabilization of the HOMOs originates not from the phenyl substitution, but from ring deformation. The MO calculations can also be used to assign the moderately intense band observed at around 429 nm in the absorption spectrum of **6**. This band is also observed for **5**, together with an accompanying MCD B-term (Fig. 28). INDO/S calculations predict that these transitions originate mainly from the HOMO→LUMO+3 transition (68%), with an oscillator strength of 0.17 in the case of **6**. The molecular symmetries of the π systems of **1** and **6** can be assumed to be D_{4h} and D_{2d}, respectively. The HOMO→ →LUMO+3 transition of **6** is therefore symmetry-allowed, while the corresponding transition for **1** is parity-forbidden with a calculated oscillator strength of 0.00. Since this transition contains 29% of the HOMO→LUMO+4 transition and MO coefficients of LUMO+4 are spread over the entire complex, including the phenyl groups, the presence of the phenyl groups plays an important role in increasing the band intensity in this region of the spectrum. In the calculation for **6***, the calculated oscillator strength of the 429 nm

band is roughly halved. The presence of this band provides another piece of evidence that the structure of **6** is highly deformed even in solution. Although we have reported these kinds of ligand deformation-induced transitions previously for an octaphenylated FePc in which parity-forbidden MLCTs become allowed due to ring deformations [116], this became the first example of a π-π* band of a Pc π system induced by saddle-type deformation.
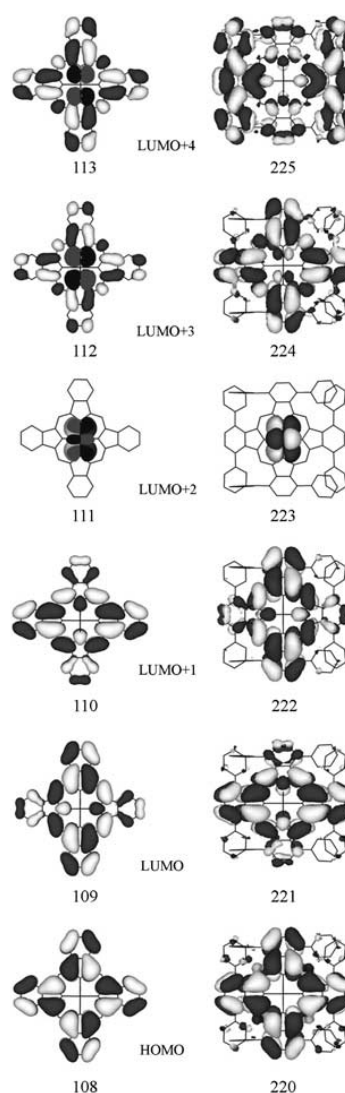

Fig. 32. Selected views of MOs of **1** (left) and **6** (right). The LUMO+2s (111 and 223 for **1** and **6**, respectively) are pyridine-centered orbitals

Рис. 32. Выбранные виды МО **1** (слева) и **6** (справа). LUMO + 2s (111 и 223 для **1** и **6** соответственно) являются пиридин-центрированными орбиталями

We have synthesized various phenyl group-substituted ZnPcs which differ in the extent of the ring deformation, and compared their Q band position, splitting, and electrochemistry, in combination with the results of MO calculations. The Q-band shifts to the red with increasing number of phenyl groups, and a

negative shift of the first oxidation potential was observed. The trends in the redox potentials from complex to complex correlate reasonably well with the results of the calculated MO energies. Configuration interaction calculations based on the INDO/S Hamiltonian reproduced the major experimentally observed spectral features. Calculations for **2*–6*** (**2–6** with the phenyl groups removed and replaced with hydrogen atoms) also showed similar Q-band energies. This study therefore revealed that sizable red shifts of the Q-band in highly deformed Pcs are brought about mainly by the ring deformations. In addition, the reduced symmetry results in the HOMO→LUMO+3 transition, which is parity-forbidden in the case of **1**, gaining significant intensity at about 430 nm in the absorption spectrum of **6**.

b) Azaphenalene Phthalocyanines (APPcs): Phthalocyanine Analogues with Six-Membered-Ring Units Instead of Five-Membered-Ring Units [122]

The electronic structure of Pcs is delineated as an annulenic 18π-electron, aromatic conjugation system comprising four isoindole units and four bridging nitrogen atoms at *meso*-positions. Modification of their electronic structure by substitution of the isoindole moieties with other aromatic units can significantly tune their electronic structures. Among such modified species, core-modified analogues, in which one or two five-membered isoindole rings are replaced with other aromatic rings, have been rather scarce, except for hemiporphyrazine and its derivatives [123]. Here, we embedded six-membered rings to Pc core (Scheme 4) instead of five-membered rings of isoindole rings, and examined their structures and electronic properties [122]. From a mixed-condensation reaction of 1,8-naphthalenedicarbonitrile and 4,5-di-*tert*-butylphenyloxyphthalonitrile in the presence of hydroquinone and nickel acetate at 300 °C for 15 min, nickel complexes of Pc (**1**) and mono- (APPc, **2**) and diazaphenalene phthalocyanines (AP₂Pc) were obtained in 9, 26, and 13% yield, respectively (Scheme 4, conditions a). As depicted in Scheme 4, two structural isomers can be expected for the disubstituted species AP₂Pc. In *adj*-AP₂Pc (**3**) two

azaphenalene moieties are arranged adjacently, whereas *opp*-AP₂Pc (**4**) has two azaphenalene moieties arranged at opposite sites. Based on analysis of the ^{1}H NMR and absorption spectra, the obtained AP₂Pc species was characterized as the *adj*-isomer **3**. The absence of **4** under these solvent-free reaction conditions was mainly due to preferable formation of a "half-Pc" intermediate [124], comprising two isoindole units and a similar subunit composed of two azaphenalene units. After several attempts to obtain **4**, we found that a condensation reaction in quinoline with ammonium molybdate as a catalyst provided all four compounds (Scheme 4, conditions b) in 11, 30, 15, and 1.4 % yield for **1–4**, respectively. The X-ray data of **6** were obtained but others were not succeeded, so that the extent of deformation was inferred from the optimized structures. Figure 33 shows the deviation of the atoms from the 4N-mean plane for **2-4**. Compared with the planar structure of **1**, the optimized structures of the APPcs are severely distorted. The displacement of all of the atoms from the 4N-mean plane clearly reveals ruffle-like distortion for **2** and saddle-like molecular distortion for **3** and **4**, as depicted in this figure. The three isoindole moieties of **2** were arranged in a fairly planar manner, whereas the azaphenalene moiety was tilted by approximately 30° from the 4N mean plane. On the other hand, an optimized structure of the free base of **2** and the crystal structure of **6** both exhibit planar conformations, indicative of the flexibility of the APPc structure. Compared with Pcs, the cavity size of **2** becomes larger due to the broader C-N-C bond angle of the azaphenalene moiety relative to isoindole moieties. Considering that the coordination bond length of low-spin Ni[II]–N is approximately 1.96 Å in the case of Pc and porphyrin complexes [125], the molecular distortion of **2** is considered to be caused mainly to fit a nickel ion into the cavity of **2**. Introduction of more azaphenalene units causes greatly enhanced saddle-like distortion, as in the case of AP₂Pcs **3** and **4**, which is also mainly due to the smaller size of the low-spin Ni[II] ion compared to their cavity size.
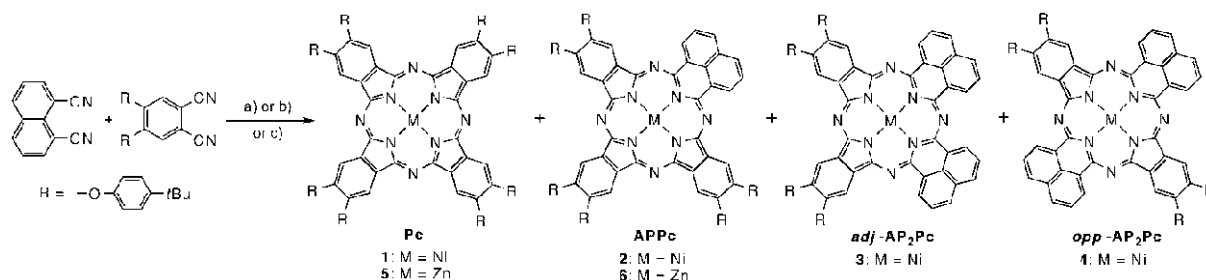
Scheme 4. Synthesis of azaphenalene phthalocyanines. Conditions: a) Ni(OAc)₂, hydroquinone, 300 °C, 15 min. b) Ni(OAc)₂, (NH₄)₂MoO₄, quinoline, 330 °C, 15 min. c) Zn(OAc)₂, hydroquinone, 260 °C, 20 min
Схема 4. Синтез азафеналенфталоцианинов. Условия: a) Ni (OAc)₂, гидрохинон, 300 ° С, 15 мин. б) Ni (OAc)₂, (NH₄)₂MoO₄, хинолин, 330 ° С, 15 мин. в) Zn (OAc)₂, гидрохинон, 260 ° С, 20 мин
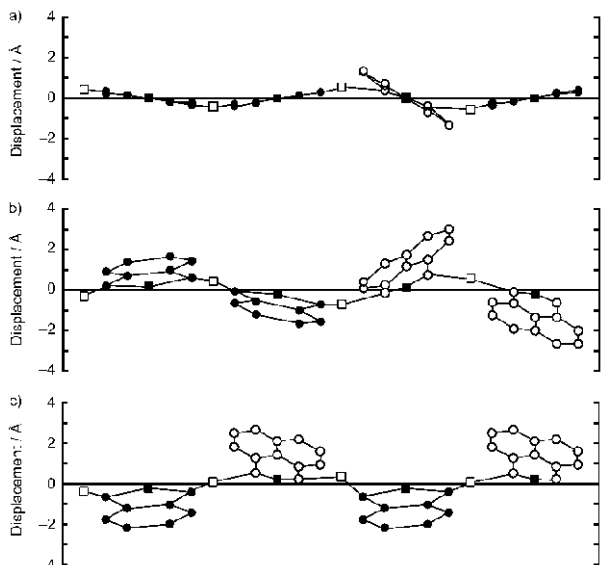
Fig. 33. Views of the skeletal deviation of the atoms from the 4N mean plane for a) **2**, b) **3**, and c) **4**. ○ and ● indicate carbon atoms of azaphenalene units and isoindole units, respectively. □ and ■ indicate nitrogen atoms at meso-positions and coordinating nitrogen atoms, respectively

Рис. 33. Виды скелетного отклонения атомов от средней плоскости 4N для a) **2**, b) **3** и c) **4**. ○ и ● указывают атомы углерода азафеналеновых фрагментов и изоиндольных фрагментов соответственно. □ и ■ обозначают атомы азота в мезо-положениях и координирующие атомы азота соответственно
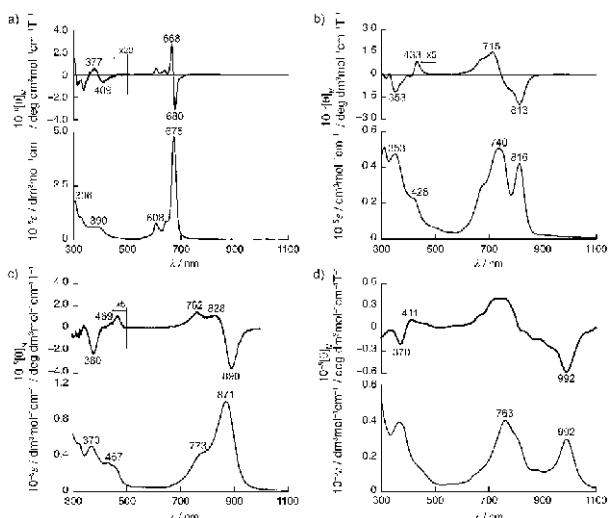

Fig. 34. Electronic absorption (bottom) and MCD (top) spectra of a) **1**, b) **2**, c) **3**, and d) **4** in CHCl₃

Рис. 34. Спектры электронного поглощения (внизу) и MCD (вверху) a) **1**, b) **2**, c) **3** и d) **4** в CHCl₃

The absorption and MCD spectra of complexes **2–4** were collected in CHCl₃ in the absence of aggregation (Fig. 34). In the absorption spectra the APPcs exhibit a fairly broad absorption in the Q-band region. Relative to the Q-band absorption of NiPc complex **1** at 675 nm, the APPc complexes exhibit a significant redshift, indicating that the electronic structures

of APPcs are quite similar to that of Pc and that a macrocyclic 18π-electron conjugation system is predominant in APPcs. Complex **3** shows a broad single Q band at 871 nm with a shoulder at 773 nm, whereas the Q-band absorptions of **2** and **4** are split into two at 816 and 740 nm, and 992 and 763 nm, respectively (Fig. 34). The energy separation of the Q bands of **4** is greater than in **2** and **6**. In the MCD spectra, APPcs **2** and **4** exhibit negative and positive signs in ascending energy, which correspond to the split Q-band absorption (Fig. 34). These signal patterns are assigned as Faraday B terms based on the MCD theory, which indicates that the excited states of these molecules are nondegenerate [22, 59, 82, 83]. The negative sign of the lower-energy Q band suggests that the energy difference between the HOMO and HOMO-1 (ΔHOMO) is larger than that of the LUMO and LUMO+1 (ΔLUMO). On the other hand, compound **3** shows a dispersion-type signal with negative and positive signs in ascending energy. This signal pattern in the Q-band region is typical of Faraday A terms, which suggests a degeneracy of the excited states, and the sign of the Q band indicates that ΔHOMO> >ΔLUMO. Faraday A terms are generally observed for Pc and its derivatives with higher symmetry than C_3. Therefore, the pattern observed for **3** is more likely assigned as pseudo Faraday A terms, which can be observed when a molecule exhibits low symmetry but the excited states are nearly degenerate, that is, when two Faraday B terms lie close in energy. Molecular orbital calculations were also performed, and found that the absorption spectra of **2-4** are described using the Gouterman's four orbital model as a theoretical framework [80]. In the cases of **2** and **4**, the two transitions appear at separate positions (729 and 647 nm for **2** and 886 and 734 nm for **4**), whereas they are close in energy in the case of **3** (780 and 768 nm). These results correlate well with the observed differences in shape of the Q bands in the absorption spectra and with the Faraday B terms for **2** and **4** and pseudo Faraday A terms for **3** in the MCD spectra.

The redox data were also collected and compared with calculated MO energy diagrams (Fig. 35).

Plots of the potentials clearly indicate a sizable negative shift of the first oxidation potential upon an increase in the number of azaphenalene units (0.42, 0.085, -0.13, and -0.23 V vs. Fc⁺/Fc for **1–4**, respectively), whereas the first reduction potential shows very little variation (-1.39, -1.35, -1.41, and -1.28 V vs. Fc⁺/Fc for **1–4**, respectively). The ΔE values thus decrease in the same order (1.81, 1.44, 1.28, and 1.05 V vs. Fc⁺/Fc for **1–4**, respectively). These results are in good agreement with the observed redshift of the lower-energy Q band in this order.

28

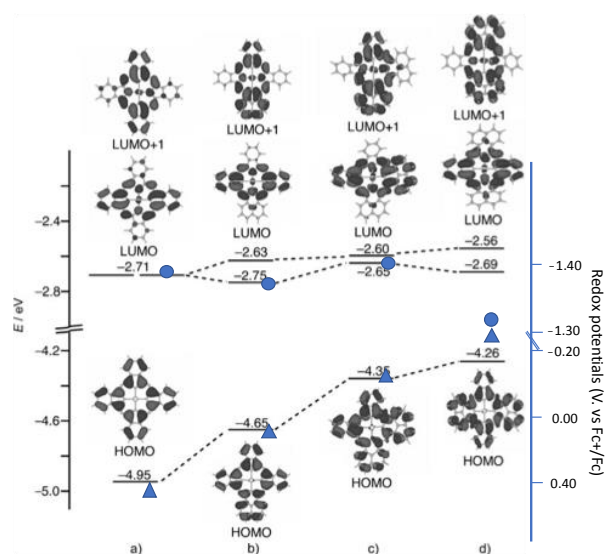Изв. вузов. Химия и хим. технология. 2019. Т. 62. Вып. 4

Fig. 35. Partial MO energy diagram and frontier orbitals of a) **1**, b) **2**, c) **3** and d) **4** derived from the DFT calculations. Experimentally obtained first reduction and oxidation potentials (right axis) are also plotted using circles and triangles, respectively

Рис. 35. Парциальная энергетическая диаграмма МО и граничные орбитали а) **1**, b) **2**, с) **3** и d) **4**, полученные из расчетов DFT. Полученные экспериментально первые потенциалы восстановления и окисления (правая ось) также нанесены с использованием кружков и треугольников соответственно

Partial MOs related to the Q-band absorptions are also depicted in Fig. 35. The amplitude of the frontier MO coefficients of the APPcs exhibit similarities to that of **1**. For each compound, the HOMO is delocalized over the molecule, whereas the LUMO and LUMO+1 are localized along the x- and y-molecular axes, respectively. Upon increasing the number of azaphenalene units, the HOMOs are energetically destabilized to a certain extent (-4.95, -4.65, -4.35, and -4.26 eV for **1–4**, respectively), whereas the LUMO energies appear to be less dependent on the number of azaphenalene units, consistent with the electrochemical results. Because of the delocalization of the LUMO and LUMO+1 along the x- and y-molecular axes, alteration in these MOs of APPcs largely depends on the positions of the azaphenalene moieties. In the case of **2**, only the LUMO+1 is destabilized in energy, which causes orbital nondegeneracy with an energy separation (ΔLUMO) of 0.12 eV. In the case of **3** both the LUMO and LUMO+1 are equally destabilized and degenerate, with a ΔLUMO value of 0.05 eV, due to the presence of two azaphenalene moieties on both the x- and y-molecular axes. In the case of **4** only the LUMO+1 is destabilized (ΔLUMO = 0.13 eV), due to the presence of azaphenalene moieties on the same molecular axis. Changes in the energy of the frontier orbitals observed for the series of APPcs are essentially similar to those of benzene-fused low-symmetry Pcs

[64-66,77]. This indicates that, despite the greatly distorted structures, the variation of the frontier MOs of APPcs from those of Pcs with D_{4h} symmetries can be understood in terms of their molecular symmetries. The contribution of the exterior naphthalene moieties of the azaphenalene units to the macrocyclic-conjugation system is similar to that of the exterior benzene and naphthalene rings of naphthalocyanine and anthracocyanine [126].

Thus, the azaphenalene units were successfully incorporated into Pc-like macrocyclic-conjugation systems. Despite the significant distortion of the molecules, caused mainly by coordination of the central nickel ion, the electronic structures of these novel analogues were more similar to those of Pcs than hemiporphyrazines. The electronic structures and, hence, their optical and electrochemical properties largely depended on the number and positions of the azaphenalene units. Based on MO calculations, a series of changes in the frontier MOs was found to be similar to that seen for benzene-fused low-symmetry Pcs but the extent of the destabilization of the HOMO and redshift of the Q bands were much more significant.

c) Crystal Structures and Electronic Properties of Saddle-Distorted and Protonated Pcs [127]

The properties of protonated Pc species resulting from the acid–base reaction have been little known because of their low basicity arising from the rigid ring structure as compared with the porphyrin ring [128]. In sharp contrast to the protonation of the porphyrin ring, which always occurs at pyrrole nitrogen atoms [129, 130]. Pcs may undergo protonation at two different sites: the isoindole nitrogen atom and the *meso*-nitrogen atom. To date, the protonation of Pcs has been limited to overly acidic conditions such as in concentrated sulfuric acid and in trifluoroacetic acid (TFA) because of the small formation constants of protonated species. Moreover, there have been no reports on either the detection of inner protonation at the isoindole nitrogen atom or of the crystal structure determination of protonated Pcs. As an application of distorted Pcs, we decided to use octaphenylated Pcs (Ph$_8$Pcs) under acidified conditions, and found properties that has not been found in normal flat Pcs.

To elucidate the protonation reaction of Ph$_8$Pcs in solution, we measured absorption spectral changes upon addition of TFA to the solution of Ph$_8$Pcs in CH$_2$Cl$_2$ and benzonitrile (PhCN). The titration of H$_2$Ph$_8$Pc by TFA in CH$_2$Cl$_2$ allowed us to observe the one-step spectral change, with isosbestic points as shown in Fig. 36a.
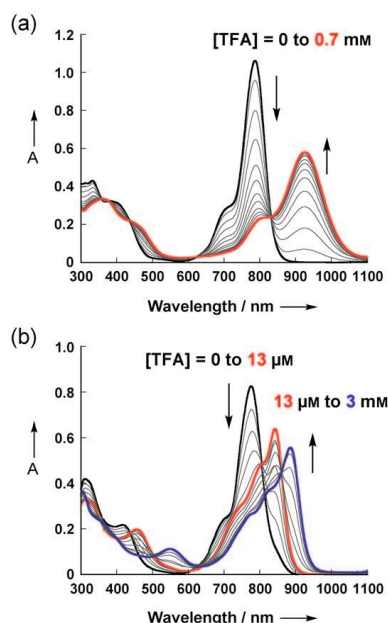
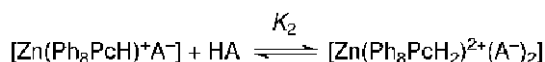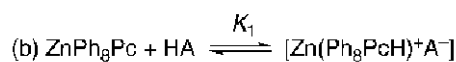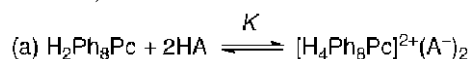Fig. 36. Absorption spectral changes upon addition of TFA to the solution of a) H_2Ph_8Pc (1.2×10^{-5} M) and b) [$ZnPh_8Pc$] (1.0×10^{-5} M) in CH_2Cl_2

Рис. 36. Спектральные изменения поглощения при добавлении TFA к раствору a) H_2Ph_8Pc ($1,2 \times 10^{-5}$ M) и б) [$ZnPh_8Pc$] ($1,0 \times 10^{-5}$ M) в CH_2Cl_2

The Job continuous variation method clearly indicates that this spectral change has 1:2 stoichiometry (not shown). From the one-step 1:2 stoichiometry equilibrium, we determined the equilibrium constant of diprotonation of the phthalocyanine ring K to be $1.2 \cdot 10^8$ M^{-2} and $4.8 \cdot 10^5$ M^{-2} in CH_2Cl_2 and PhCN, respectively (Scheme 5).

$$(a)\ H_2Ph_8Pc + 2HA \xrightleftharpoons{K} [H_4Ph_8Pc]^{2+}(A^-)_2$$

$$(b)\ ZnPh_8Pc + HA \xrightleftharpoons{K_1} [Zn(Ph_8PcH)^+A^-]$$

$$[Zn(Ph_8PcH)^+A^-] + HA \xrightleftharpoons{K_2} [Zn(Ph_8PcH_2)^{2+}(A^-)_2]$$

Scheme 5. The protonation equilibria of a) H_2Ph_8Pc and b) [$ZnPh_8Pc$] by acid (HA)

Схема 5. Протонное равновесие a) H_2Ph_8Pc и б) [$ZnPh_8Pc$] кислотой (HA)

This apparent one-step diprotonation is ascribed to the high basicity of the inner-monoprotonated Pc, which is due to the more deformed structure, akin to the monoprotonated porphyrin [129b].

In sharp contrast to H_2Ph_8Pc, a two-step spectral change was observed in the course of the titration of [$ZnPh_8Pc$] with TFA in CH_2Cl_2, with two isosbestic points (Fig. 36b). These spectral changes were assigned to monoprotonation and diprotonation of the Pc ring in the light of previous work [128]. The first spectral change was induced by adding one equivalent of

TFA, clearly showing that monoprotonation occurred. The equilibrium constants of mono- and diprotonation (K_1 and K_2, Scheme 5b) were determined to be $1.4 \cdot 10^5$ and 27 M^{-1} in PhCN, respectively. The absorption spectra of the single crystals of [H_4Ph_8Pc]Br_2 and [$ZnCl(Ph_8PcH)$)] in CH_2Cl_2 agreed with those obtained by absorption titration experiments (red lines in Fig. 36a,b), which clearly indicates that the protonated Ph_8Pcs are stable even in a non-acidic solution owing to the large formation constants of the protonated species.

In the case of planar free-base Pcs, the protonation of the *meso*-position is energetically more favorable [128]; however, inner protonation (-9.5 kcal·mol^{-1}) is more stable than outer protonation (-4.5 kcal·mol^{-1}) for the saddle-distorted H_2Ph_8Pc, as suggested by DFT calculations. This energy reversal can be explained by the compensation for destabilization arising from the structural distortion by stabilization of hydrogen bond formation among N-H protons of the isoindole rings and bromide ions, as seen in the crystal structure (although not shown, two bromide ions are located just above and below the center of four pyrrole nitrogens of H_2Ph_8Pc). In the ^1H NMR spectrum of the single crystals of [H_4Ph_8Pc]Br_2 in $CDCl_3$, a singlet signal at $\delta = 6.4$ ppm was assigned to the isoindole N-H, since the peak disappeared. upon addition of a drop of D_2O. The ^1H NMR spectrum of [$ZnCl(Ph_8PcH)$] shows more complex signals than that of [$ZnPh_8Pc$], probably owing to the lowering symmetry induced by the proton at the *meso*-nitrogen atom. This situation was confirmed by the observation of an exchangeable proton with a signal at $\delta = 12.3$ ppm, which was assigned to the proton bound to the *meso*-nitrogen atom. The coordination of the chloride ion to the zinc center of [$ZnCl(Ph_8PcH)$] in solution was confirmed by electrospray ionization mass spectrometry (ESI-MS), which detected a peak cluster arising from [$ZnCl(Ph_8Pc)$]$^-$ (m/z 1222.4) in its deprotonated form in the negative detection mode.

We measured the magnetic circular dichroism (MCD) spectra of protonated Ph_8Pcs in CH_2Cl_2 to reveal the electronic structures of both inner- and outer-protonated Ph_8Pcs (Fig. 37).

[H_4Ph_8Pc]Br_2 adopts D_{2d} symmetry owing to saddle deformation of the ligand caused by steric congestion at the ligand periphery. The spectral features are similar to those of a D_{4h} metallophthalocyanine derivative, because a four-fold axis of symmetry is retained in the central part of the core and the LUMO therefore remains doubly degenerate [80]. An intensification of the lower-energy Q band was observed in the MCD spectrum relative to the absorption spectrum, owing to the larger orbital angular momentum change associated with the Q transition [16, 17]. Only the A_1

term arising from the Q band of [H₄Ph₈Pc]Br₂ can be readily identified owing to extensive configurational interaction between the B1 and higher-energy $\pi\pi^*$ states. The presence of an axial ligand and a protonated *meso*-nitrogen atom lowers the symmetry of [ZnCl(Ph₈PcH)] to C_1. Therefore, the Q band shifts to longer wavelength (845 nm) relative to the corresponding D_{2d} [ZnPh₈Pc] complex (786 nm) [110] A trough of MCD intensity (846 nm) corresponds almost exactly to the absorption maximum of the Q band (845 nm), thus confirming the presence of well-separated Faraday B_0 terms, as would normally be anticipated when there is a large zero-field splitting of the Q and B1 $\pi\pi^*$ states owing to the absence of a C_3 or higher axis of symmetry [16]. A minus-to-plus pattern is consistently observed in ascending energy terms in the Q-band region of each MCD spectra. which is consistent with a greater splitting of the occupied MOs than would be anticipated for [H₄Ph₈Pc]Br₂ based on the D_{2d} symmetry of the chromophores and for [ZnCl(Ph₈PcH)] based on the results of molecular orbital calculations [16, 17, 55, 81-83].

In summary, the first crystal structures of Pcs protonated at the *meso*- and isoindole nitrogen atoms
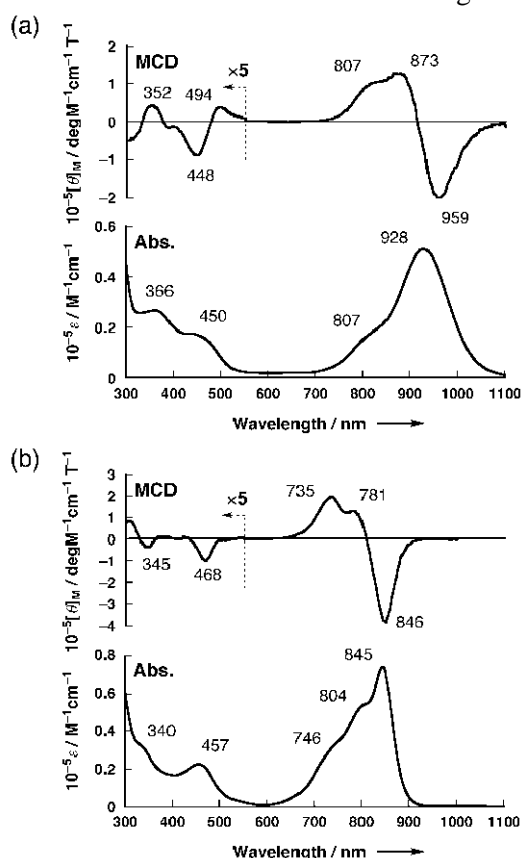

Fig. 37. Absorption (lower) and MCD (upper) spectra of a) [H₄Ph₈Pc]Br₂ and b) [ZnCl(Ph₈PcH)] in CH₂Cl₂

Рис. 37. Спектры поглощения (нижний) и MCD (верхний) a) [H₄Ph₈Pc] Br2 и b) [ZnCl (Ph₈PcH)] в CH₂Cl₂

were determined by using saddle-distorted phthalocyanines. The saddle distortion of Ph₈Pc facilitates the protonation of the phthalocyanine ring. The outer protonation of [ZnPh₈Pc] afforded the stable monoprotonated form with small structural change, while the inner-diprotonated [H₄Ph₈Pc]Br₂ shows a significantly deformed structure. The presence of two possible sites for protonation differentiates Pc from porphyrin in terms of protonation pattern and resultant characteristics. The saddle-distorted structure of H₂Ph₈Pc enables the inner protonation by virtue of the hydrogen bonding among isoindole protons and the counteranion, as is also true for saddle-distorted porphyrins [129b]. These results describe two types of protonated Pcs in terms of their structures and their spectroscopic and electrochemical properties.

d) Azepiphthalocyanine—An Unprecedented Large Twist of a π-Conjugation System upon Core-Modification with a Seven-Membered Ring Unit [131]

In the above b), six-membered units were introduced and its effect on the structure and spectroscopic units were discussed [122]. Further motivation to reveal the role of the ring unit in the core led us to a synthesis of a novel core-modified Pc analogue with a larger seven-membered ring unit. Thus, aromatic dicarbonitrile bearing cyano groups in a 1,4-relationship was utilized for a Pc synthesis to give azepiphthalocyanine (AZPPc) having a seven-membered ring unit instead of a five-membered ring unit. This molecule exhibited a significantly twisted structure and large splitting of the Q band absorption, indicative of its azachlorin-like conjugation system.

A mixed-condensation reaction of 4,5-di-*p*-*tert*-butylphenyloxyphthalonitrile (**1a**) and 2,2'-biphenyldicarbonitrile (**2**) in the presence of anhydrous nickel acetate and ammonium molybdate in quinoline at 330 °C provided a mixture of Pc (**3a**) and AZPPc (**4a**, Scheme 6). **4b** was similarly obtained from a reaction using 4,5-di-p-*tert*-butylphenylphthalonitrile. The ¹H NMR spectra of **4a** and **4b** in CDCl₃ at room temperature exhibit three signals due to the α-benzo protons at 8.55, 8.53, and 8.37 ppm and at 9.06, 9.04, and 8.81 ppm, respectively, while the *tert*-butyl protons are observed at 1.34, 1.33, and 1.31 ppm and at 1.37, 1.35, and 1.31 ppm. These signal patterns suggest C_2 symmetric molecular structures. The ¹H–¹H COSY experiments on **4a** and **4b** enable assignment of the biphenyl proton signals at 7.86, 7.58, 7.29, and 6.58 ppm and at 7.91, 7.60, 7.36, and 6.68 ppm, respectively. Significant up-field shifts of biphenyl protons at 6.58 ppm for **4a** and at 6.68 ppm for **4b** infer the presence of diatropic ring current effects arising from macrocyclic aromatic conjugation systems.

Izv. Vyssh. Uchebn. Zaved. Khim. Khim. Tekhnol. 2019. V. 62. N 4

31
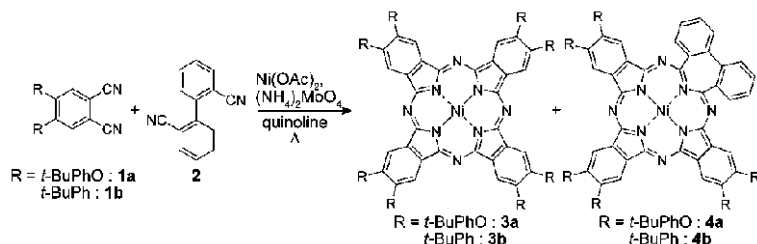
Scheme 6. Synthesis of AZPPc **4a** and **4b**

Схема 6. Синтез AZPPc **4a** и **4b**

The structure of **4b** was unambiguously elucidated by X-ray crystallographic analysis (Fig. 38). The biphenyl moiety is nearly orthogonal from the mean plane, which is determined by four coordinating nitrogen atoms, mainly due to the strain caused around the seven-membered ring and the steric congestion of the biphenyl moiety, while the rest of the molecule takes a slightly distorted ruffle conformation. The central nickel ion does not have a significant effect on this deformation, considering that the structural optimization on model compounds of a free-base and a zinc complex suggests similar distorted structures. Hydrogen atoms at C3 and C12 positions lie above and below the molecular plane, which results in the observed up-field shift of these proton signals in the ^{1}H NMR spectra. The single bond nature of the C1–C2 and C13–C14 bonds, 1.514(5) and 1.501(5) Å, respectively, infers a small contribution of an azepin-like conjugation system in this molecule. On the other hand, the double bond nature of the C1–N1 and N1–C14 bonds, 1.366(5) and 1.372(5) Å, respectively, and the small bond length alternation between these bonds are indicative of the major contribution of these bonds for the [18] annulene-like conjugation system.

The absorption spectra of **4a** and **4b** in CHCl$_3$ exhibit significantly split Q-bands in both the higher and lower energy regions relative to the Q bands of **3a** at 675 nm in CHCl$_3$ (Fig. 39). The tail of the absorption extends to 1000 nm, and **4a** and **4b** cover a broad range in the vis/NIR region, in which conventional Pcs do not exhibit absorption. These absorption spectra are also clearly different from those of periphery expanded low-symmetry Pc analogues, which exhibit similar split Q band absorptions in the lower energy region than Pcs. [63, 64, 118, 119]. The MCD spectrum of **4a** shows negative and positive envelopes (Faraday B terms) in ascending energy corresponding to the split Q bands in the absorption spectrum (Fig. 39). The peak position of the negative envelope deviates to the red by 387 cm^{-1} relative to the λ_{max} of the lower energy Q band absorption.

The TDDFT calculations indicate that the absorption spectrum of AZPPc can be basically illustrated using Gouterman's four orbital model as a theoretical framework [80]. The coefficient of the frontier orbitals is delocalized over the molecule with the exception of the biphenyl moiety, which is due to the

twist of the azepine moiety (Fig. 40). This is clearly different from Pcs [16, 19, 22, 37, 38], APPcs [122], and periphery expanded low-symmetry Pc analogues [63, 118], in which the frontier molecular orbitals are delocalized over the whole molecules. A change in the main conjugation pathway due to the significant twist at the azepine moiety causes destabilization of the HOMO and LUMO+1. The HOMO–LUMO gap thus becomes smaller, while the HOMO–LUMO+1 gap becomes larger.
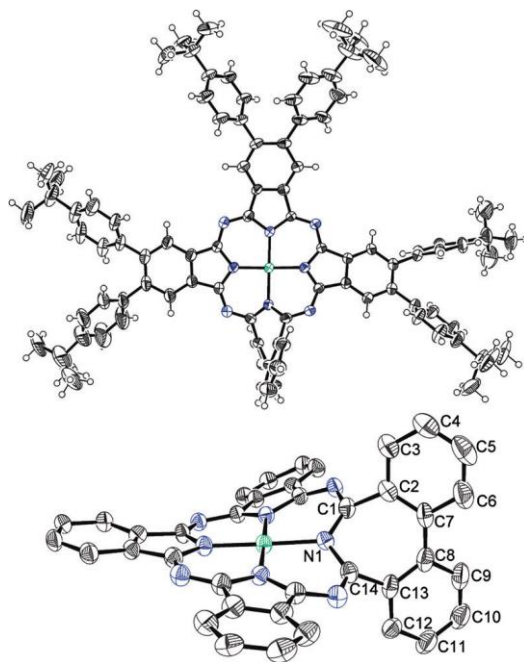
Fig. 38. Crystal structure of **4b**, top view (top) and side view (bottom). tert-Butylphenyl substituents and hydrogen atoms are omitted for clarity in the side view

Рис. 38. Кристаллическая структура **4b**, вид сверху (сверху) и вид сбоку (снизу). Трет-бутилфенильные заместители и атомы водорода опущены для ясности в виде сбоку
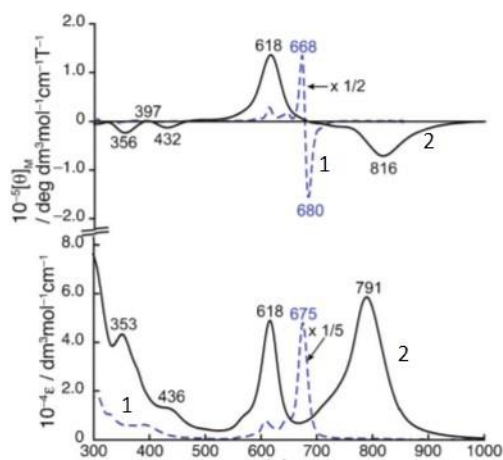
Fig. 39. Absorption (bottom) and MCD (top) spectra of **3a** (1) and **4a** (2) in CHCl$_3$

Рис. 39. Спектры поглощения (внизу) и МCD (вверху) для **3a** (1) и **4a** (2) в CHCl$_3$

These results are in good agreement with the observed large splitting of the Q bands and the Faraday B terms. This variation of the frontier molecular orbital diagram is essentially similar to those of azachlorin-type molecules [132], indicating that the electronic structure of AZPPc is rather similar to that of an azachlorin molecule than that of Pc.
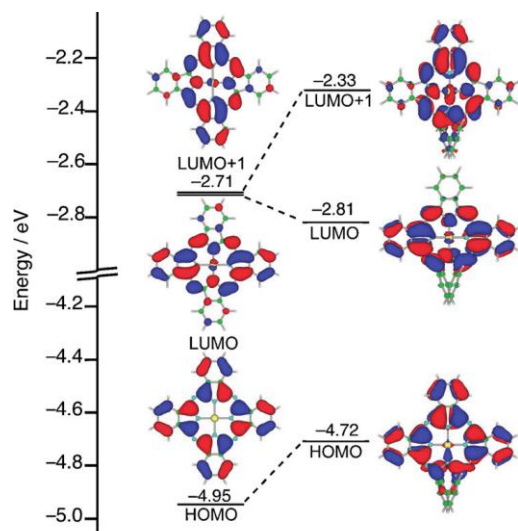

Fig. 40. Frontier molecular orbital diagrams of model compounds of **3a** (left) and **4a** (right)

Рис. 40. Границы молекулярно-орбитальных диаграмм модельных соединений **3a** (слева) и **4a** (справа)

TDDFT calculations at the B3LYP/6-31G(d) level reproduce the observed absorption spectra well and predict two energetically different bands in the Q band region at 729 and 647 nm with the oscillator strengths of 0.33 and 0.23, respectively. These two theoretical bands mainly consist of transitions from the HOMO to LUMO and from the HOMO to LUMO+1, respectively.

In conclusion, AZPPc synthesized by using 2,2'-biphenyldicarbonitrile as a key synthetic precursor showed enhanced distortion of the molecular structure due to the steric congestion of the seven-membered ring and biphenyl moiety. The X-ray structure revealed that the seven-membered unit is nearly perpendicular to the macrocyclic plane. The inner seven-membered ring unit has less contribution to merge the 18π annulenic conjugation system and the peripheral conjugation system of the biphenyl unit. This results in variation of the frontier molecular orbital diagram as exemplified by the high-lying HOMO and LUMO+1. The absorption spectrum of AZPPc is thus better illustrated by the azachlorin-like electronic structure.

e) Superazaporphyrins: Meso-Pentaazapentaphyrins and One of Their Low-Symmetry Derivatives [133]

As a ring-expanded pentapyrrolic Pc congener, only the compound called superphthalocyanine (SPc),

consisting of five isoindole units, is known [134]. The first SPc was reported more than 40 years ago [134a]. SPcs are attractive in modern technology in that they show a Q band in the near-IR region beyond 900 nm. To date, researchers in the fields of, for example, solar cells and photodynamic therapy, have tried to obtain stable compounds having strong absorption in the near-IR region. This absorption may be attained by going from smaller to larger compounds, since the absorption bands generally shift to longer wavelengths (reduction of the HOMO–LUMO gap) [16, 22, 30]. However, when easily prepared Ncs and Acs are used, the problem has been the instability of the larger compounds as they generally decompose within a few days [30, 126]. Herein, we report the synthesis and properties of the so-called superazaporphyrins (SAzP) which consist of five pyrrole units (Scheme 7). In particular, it is shown why they are stable even though their Q band appears beyond 800 nm. After SPc, SAzP is the second example of a compound consisting of five pyrrolic rings and *meso*-nitrogen atoms.
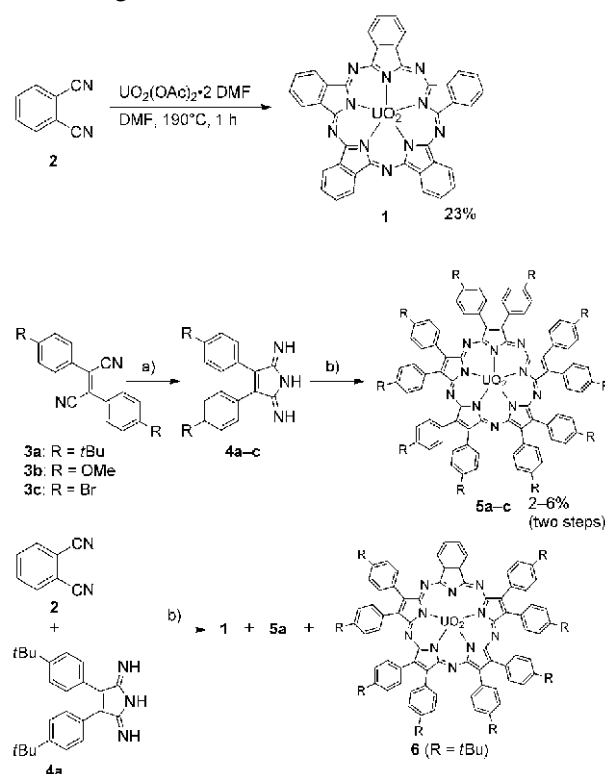
Scheme 7. Synthesis of the superphthalocyanine (SPc) **1**, superazaporphyrins (SAzPs) **5a-c**, and the low-symmetry SAzP **6**. Reagents and conditions : a) Na, NH3 (gas), nC5H11OH, 105 °C, 3 h; b) UO2(OAc)2·2DMF, 190 °C, 1 h

Схема 7. Синтез суперфталоцианина (SPc) **1**, суперазапорфиринов (SAzPs) **5a-c** и SAzP **6** с низкой симметрией . Реагенты и условия: a) Na, NH3 (газ), nC5H11OH, 105 ° C, 3 ч; b) UO2(OAc)2 2DMF, 190 ° C, 1 ч

An unsubstituted SPc containing a linear and rigid O=U=O central core (**1**) was obtained by condensation of **2** in the presence of UO2(OAc)2·2DMF in

DMF in 23% yield. The SAzPs **5** were obtained by uranium-templated cyclization of five molecules of **4** which were synthesized from the fumaronitrile **3** (Scheme 7). Although SPc **1** is known to be obtained practically only when substituent-free **2** is used. In the case of the low-symmetry **6**, which contains one isoindole and four pyrroline rings, a mixed condensation was carried out using **2** and **4** a at a mole ratio of 1:1 at 190 °C for 1hour.
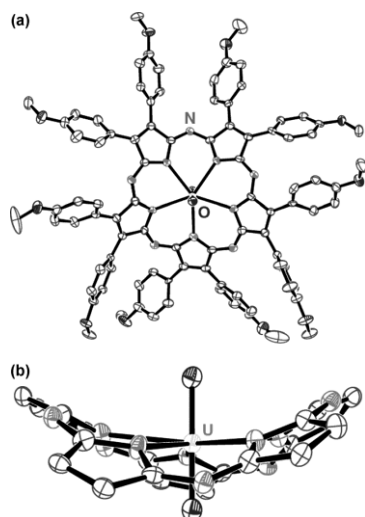

Fig. 41. The molecular structure of **5b**. The thermal ellipsoids are shown at 50 % probability. a) Top view and b) side view (peripheral substituents omitted). Hydrogen atoms and solvent molecules are omitted for clarity

Рис. 41. Молекулярная структура **5b**. Тепловые эллипсоиды показаны с вероятностью 50%. a) вид сверху и b) вид сбоку (периферические заместители опущены). Атомы водорода и молекулы растворителя опущены для ясности

Formation of the compounds was first confirmed by HR/ MALDI-FT-ICR/MS and ^{1}H NMR spectroscopy. Compound **1** showed only two ^{1}H NMR signals assignable to the α and β protons of the isoindoles (δ = 9.15 and 8.09 ppm), whereas **5a–c** showed only two sets of signals arising from the *ortho* and *meta* protons of the phenyl groups, thus suggesting a highly symmetrical structure in solution. The compound **6** showed both α and β protons of the isoindoles and *ortho* and *meta* protons of the phenyl groups in the expected ratio (1:1:8:8), all at different positions, thus reflecting the low symmetry of the molecule. Single crystals of **5b** suitable for X-ray crystallography were grown by slow diffusion of *n*-hexane into a toluene solution of **5b** (Fig. 41). The crystal structure of **5b** reveals that the macrocycle comprises five pyrroline rings linked by five nitrogen atoms, with the U^{VI} ion sitting in the center of the SAzP 5N mean plane (Δ5N < 0.005 Å). **5b** is not planar, but has a severely saddled structure, as reported for the crystal structure of SPc

[134b]. No significant bond-length alternation was observed for the C-N and C-C bonds of the core structure of **5b**, as would be anticipated for a nonplanar heteroaromatic π system.
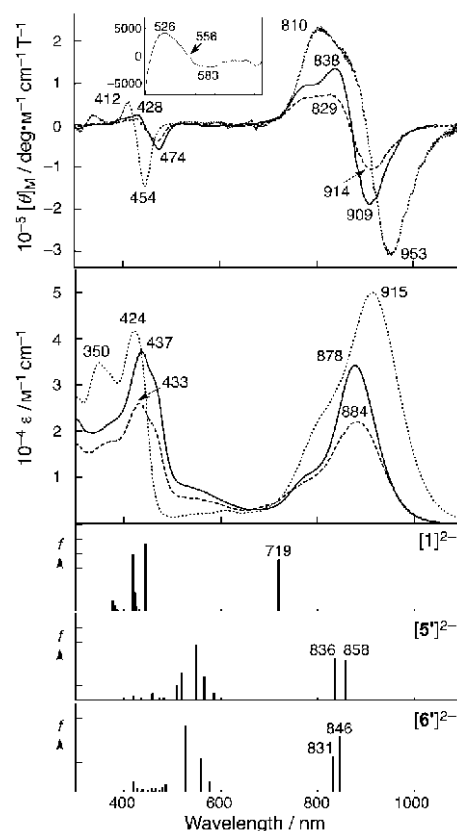

Fig. 42. MCD (top) and electronic absorption (middle) spectra of **1** (dotted lines), **5a** (solid lines), and **6** (dotted broken lines). Inset: Magnified MCD spectrum of **5a**. Theoretical absorption spectra (bottom); the solid lines are those calculated by the TD-DFT method. Calculations were carried out for the free-base dianion species without *tert*-butyl groups at the B3LYP/6-31G* level of theory

Рис. 42. Спектры MCD (вверху) и электронного поглощения (в центре) для **1** (пунктирные линии), **5a** (сплошные линии) и **6** (пунктирные пунктирные линии). Вставка: увеличенный спектр MCD для **5a**. Теоретические спектры поглощения (внизу); сплошные линии - это те, которые рассчитаны методом TD-DFT. Расчеты проводились для разновидностей дианионов со свободным основанием без трет-бутильных групп на уровне теории B3LYP / 6-31G *

Figure 42 shows the electronic absorption and MCD spectra of compounds **1**, **5a**, and **6**. The SPc **1** exhibited Q- and Soret-like bands at 915 nm and 424 nm, respectively, which are at longer wavelengths than those of normal Pcs (ca. 650-700 nm and 330-350 nm, respectively), and the corresponding dispersion-type, Faraday A MCD curves, thus experimentally supporting the fact that the excited state is orbitally degenerate. The SAzP **5a** exhibited these bands at 878 and 437 nm. Therefore, in going from **1** to **5a**, the Q band shifted to a shorter wavelength, while the Soret band shifted to a

34

Изв. вузов. Химия и хим. технология. 2019. Т. 62. Вып. 4

longer wavelength, both of which are phenomena similar to those observed in going from Pc to octaaryltetraazaporphyrin [38], A weak absorption on the longer-wavelength side of the Soret band, at about 500-600 nm, is characteristic of AzPs having many phenyl groups [89]. The substitution effect at the aryl position is relatively weak so that the positions of the Q bands of **5a–c** are close together. The low-symmetry **6** showed a Q band at 884 nm, which is between that of **5a** (878 nm) and **1** (915 nm), thus suggesting indeed that **6** is an intermediate compound between **1** and **5a.** The dispersion-type MCD curves corresponding to the Q bands of **5a** and **6** are theoretically Faraday A and pseudo Faraday A terms, respectively [16, 17, 107, 108]. In the case of **6**, it is thought that the splitting of the Q band is so small that the superimposition of two oppositely-signed Faraday B terms give seemingly A-term-like MCD signals.

To enhance the interpretation of the electronic absorption spectra, MO calculations have been performed for unsubstituted and pyrrole proton-deprotonated Pc, uranium ion-free and pyrrole proton-deprotonated **1**, **5a**, and **6** without *tert*-butyl groups, that is, $[\mathbf{Pc}]^{2-}$, $[\mathbf{1}]^{2-}$, $[\mathbf{5'}]^{2-}$, and $[\mathbf{6'}]^{2-}$, at the DFT level. This analysis omitting the metal is due to the fact that it is difficult to evaluate accurately the electron density of f-block metals such as uranium. Calculated stick absorption spectra are attached at the bottom of Fig. 42, with obtained MO energy levels and isosurface plots of some frontier MOs shown in Fig. 43. The calculated Q bands, which are transitions mainly from the HOMO to LUMO and LUMO+1, were estimated at wavelengths close to the experimental values for the compounds. In addition, as can be judged from the configuration (not shown), the contribution of the four frontier orbitals is large in both the Q- and Soret-band regions, thus indicating that these bands can be explained using Gouterman's four-orbital model [80]. The calculated Q-band intensity increases on going from $[\mathbf{5'}]^{2-}$ to $[\mathbf{1}]^{2-}$, that is, with increasing size of the π system, as generally observed among tetraazaporphyrins of varying sizes [126].

As shown in Fig. 43, the LUMO and LUMO+1 of $[\mathbf{1}]^{2-}$ and $[\mathbf{5'}]^{2-}$ are degenerate, similar to $[\mathbf{Pc}]^{2-}$, whereas the degeneracy is lifted slightly in the case of $[\mathbf{6'}]^{2-}$. In going from $[\mathbf{Pc}]^{2-}$ to $[\mathbf{1}]^{2-}$, that is, from cyclic tetramer (**Pc**) to pentamer (**1**), the energy of the four frontier orbitals is stabilized, but since the stabilization of the LUMO is larger than that of the HOMO, the Q band shifts to a longer wavelength. Comparison between the cyclic pentamer $[\mathbf{5'}]^{2-}$ and $[\mathbf{1}]^{2-}$ reveals a similar change as observed when the cyclic tetramers Pc and Nc are compared. In going from Pc to Nc, with increasing π-molecular size by fusion of the benzo rings,

both the HOMO and LUMO destabilize and the Q band shifts to a longer wavelength. However, even the LUMOs and HOMO of $[\mathbf{1}]^{2-}$ (SPc **1**) lie lower in energy than those of Pcs. This lower energy of the HOMO appears to be the reason for high stability of the SAzPs **5** and SPc **1**. Although the SAzPs **5** and SPc **1** have their Q bands at around 840-880 nm and 915 nm, respectively, they appear to be much more stable than Ncs [54, 126].
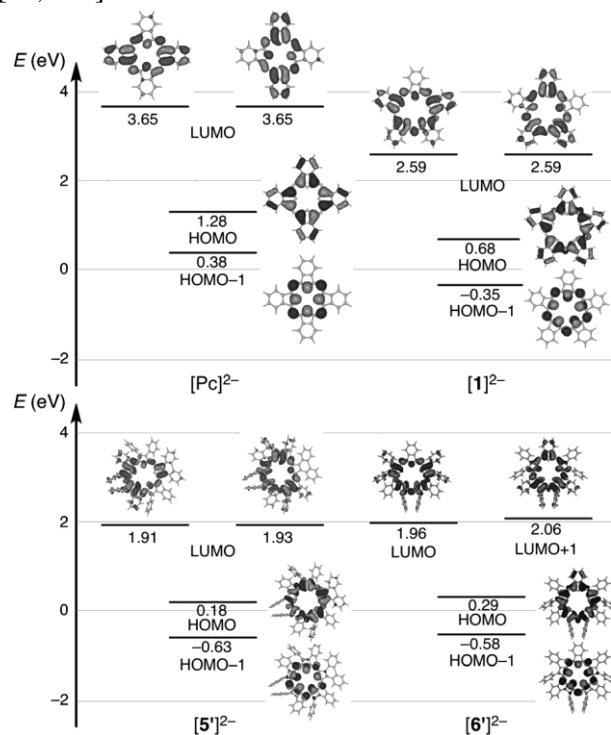

Fig. 43. Energies and some frontier orbitals of $[\mathbf{Pc}]^{2-}$, $[\mathbf{1}]^{2-}$, $[\mathbf{5a'}]^{2-}$ and $[\mathbf{6'}]^{2-}$. Calculations were performed at the B3LYP/6-31G* level of theory

Рис. 43. Энергии и некоторые пограничные орбитали $[\mathbf{Pc}]^{2-}$, $[\mathbf{1}]^{2-}$, $[\mathbf{5a'}]^{2-}$ и $[\mathbf{6'}]^{2-}$. Расчеты проводились на уровне теории B3LYP / 6-31G *

Cyclic voltammograms of the tetra-*tert*-butyl-substituted H₂Pc (*t*Bu₄H₂Pc), SPc **1**, and **5a** were measured in *o*-DCB. The *t*Bu₄H₂Pc showed redox couples at 0.26, -1.44, and -1.79 V (E_{1ox}-E_{1red} = 1.70 V), whereas the SPc **1** exhibited couples at 0.24, -0.94, -1.29, -1.69 V (E_{1ox}-E_{1red} = 1.18 V). Although the oxidation potentials are similar, the reduction of the SPc **1** is much easier (by $\Delta E = 0.50$ V) than that of *t*Bu₄H₂Pc, thus indicating marked stabilization of the LUMOs of the SPc **1**. This result implies that the origin of the narrow HOMO–LUMO gap of **1** is attributable to the low-lying LUMOs. The SAzP **5a** showed redox couples at 0.48, -0.85, and -1.18V (E_{1ox}-E_{1red} = 1.33 V), thus revealing that the frontier orbitals of **5a** are further stabilized compared with those of the SPc **1**, and provides support for the predicted MO energy level. Thus, the longer-wavelength shift of the Q bands of the SAzP **5**

and SPc **1** is attributable to the stabilization of the frontier orbitals, particularly the LUMOs. The position of the Q band of general Pcs (ca. 650-700 nm), **5**, and **1** is also in accord with the order of the (E_{1ox}-E_{1red}) values.

In conclusion, superazaporphyrins (SAzPs) consisting of five pyrroline-2,5-diimine units and a uranium atom, and one of their low-symmetry derivatives were synthesized , by using pyrroline-2,5-diimine as a precursor. We also reinvestigated superphthalocyanine (SPc) using methods which were not used 35-40 years ago. X-ray crystallography revealed a distorted macrocyclic structure for the superazaporphyrins. Decaaryl SAzPs showed Q bands at approximately 840–880 nm, and the spectra could be interpreted by Gouterman's four-orbital model [80]. Both SAzPs and SPcs are aromatic and can be explained by the ($4n+2$) aromaticity rule, where $n = 5$. MCD spectroscopy and MO calculations strongly suggest that the Q-excited state is doubly degenerate. Although the Q bands of SAzPs and SPcs appear at longer wavelengths than those of Ncs, electrochemical measurements and MO calculations indicated that they are relatively air stable, since the energy of both the LUMOs and HOMO is lower than those of Pcs and Ncs.

2-3. Subporphyrin (SubP) and SubPc Systems
a) Synthesis and Characterization of meso-Triarylsubporphyrins [135]

Porphyrins normally consist of four pyrrole rings linked by *meso*-carbons at the α-pyrrole carbons. Tetraphenylporphyrins (TPPs) and octaethylporphyrins (OEPs) have been examined most intensively due to their easy synthesis, in the case of TPPs, and relevance to biologically important porphyrins, in the case of OEPs. However, porphyrin congeners that consist of three pyrrole units (subporphyrin, SubP) were not known, although ring-contracted phthalocyanine congeners named subphthalocyanine (SubPc) consisting of three isoindole rings was first reported in 1972 and a few hundreds of papers have been reported since then [38, 136].

A series of *meso*-triarylsubporphyrins were synthesized in 4-8% yields by using tripyrrolylborane as the template for an Adler reaction (Scheme 8).
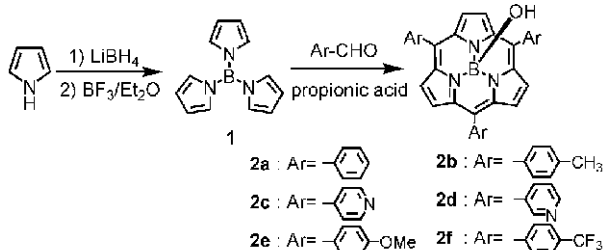
Scheme 8. Synthetic pathway to triarylsubporphyrins
Схема 8. Синтетический путь к триарилсубпорфиринам

Typically, for example, **2a** was prepared as follows. Other **2b-2f** were obtained in a similar manner. Tripyrrolylborane **1** (0.1 g, 0.48 mmol) was dispersed in propionic acid (35 mL). The solution was added slowly dropwise to a refluxing solution of benzaldehyde (*ca.* 0.1 mol/L, 3.5 mmol) in propionic acid (35 mL) over 45 min. The progress of the reaction was monitored by periodically measuring the absorption spectra of the reaction solution. The solution was then heated under reflux for a further 3-4 h until the absorbance of a PhsubP (**2a**) peak at 373 nm ceased to increase. The solvent was removed. The residue was dissolved in $CHCl_3$ and then passed through a short column of Celite to remove undissolved materials. Subsequently, purification was performed using silica gel chromatography.
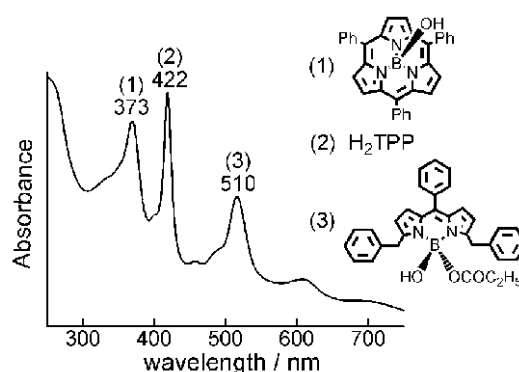
Fig. 44. Electronic absorption spectrum recorded at the end of the condensation reaction of PhsubP (**2a**). The solvent consists of a few drops of propionic acid solution diluted by $CHCl_3$. The peaks at 373, 422, and 510 nm are associated with (**1**) PhsubP (**2a**), (**2**) H_2TPP, and (**3**) a boron dipyrromethene derivative, respectively

Рис. 44. Электронный спектр поглощения записанный в конце реакции конденсации PhsubP (**2a**). Растворитель состоит из нескольких капель раствора пропионовой кислоты, разбавленной $CHCl_3$. Пики при 373, 422 и 510 нм связаны с (**1**) PhsubP (**2a**), (**2**) H_2TPP и (**3**) производным дипиррометен-бора, соответственно

Figure 44 shows the absorption spectrum of the reaction solution diluted by $CHCl_3$. Three intense peaks are seen and these are assigned to the target **2a**, tetraphenylporphyrin free-base, and a BODIPY compound. In the ^1H NMR spectrum, the β-position ^1H peak is observed at 8.1 ppm in the case of **2a** due to the heteroaromatic nature of the subporphyrin π-system. The downfield shift is not as great as that observed for TPP (8.75 ppm), since the diamagnetic ring current effect is reduced due to the domed structure and the inner ligand perimeter being comprised of a 14π- rather than an 18π-electron conjugation system. In order to confirm the structure, x-ray analysis was carried out for **2f** (Fig. 45). (**2f**) Exhibited a domed conformation with the boron atom coordinated in tetrahedral fashion by the three pyrrolic nitrogen atoms and an oxygen atom of the methoxy group (Fig. 45a, b). The bowl depth as

36

Изв. вузов. Химия и хим. технология. 2019. Т. 62. Вып. 4

defined by the distance from the boron to the mean plane of the six β-position carbon atoms is 1.430 Å, which is significantly deeper than the 1.175 Å depth observed by Osuka and co-workers [137] for the corresponding methoxy ligated tribenzosubporphyrin.

The angles data also provide strong evidence for a shallow domed tripyrrolic cyclic structure. The average O(axial oxygen)-B-N(pyrrole) angle is 113.8°, which is slightly lower than the 115.6° angle reported for subAP (hexaethyltriazasubporphyrin) [138]. In contrast, the N-B-N angle is *ca.* 104.8°, which is higher than the 102.7° value observed in the case of subAP. These data reflect the fact that the depth of the dome is shallower than that of subAP and this, in turn, is related to the smaller central hole size of subAP due to the shorter N(*meso*)-pyrrole-(α) distance. One of the most distinct differences from TPP is that the C(*meso*)-C(pyrrole(α))-C(pyrrole(β)) angle is much larger (133.2°) than that of ZnTPP (124.6°) [139]. As a result, the phenyl substituents are gently tilted from the subporphyrin plane with a dihedral angle of *ca.* 50.3°, while the phenyl dihedral angles are generally in the 70°-90° range in the case of TPP [140].
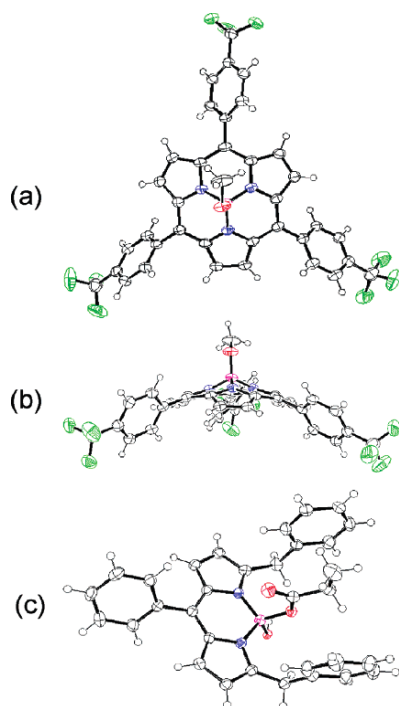

Fig. 45. (a) Top and (b) side view of the X-ray structure of TFsubP (**2f**) and (c) side view of the boron dipyrromethene by-product (see Fig. 44, for the molecular structure)
Рис. 45. (a) Вид сверху и (b) сбоку рентгеновской структуры TFsubP (**2f**) и (c) вид сбоку побочного продукта дипиppoметена бора (молекулярная структура см. на рис. 44)

The redox couples of **2a-f** were collected in o-DCB (Fig. 46). The first reduction occurred at *ca.* -2.1 to -1.8 V vs Fc+/Fc, while the first oxidation potentials

were detected at 0.45-0.85 V. Since the central boron atom does not participate in the redox process within the potential range used in this experiment, the observed redox couples are ascribed to the subP ligand. Both oxidation and reduction couples shift depending on whether the *meso*-substituents are electron donating or withdrawing.
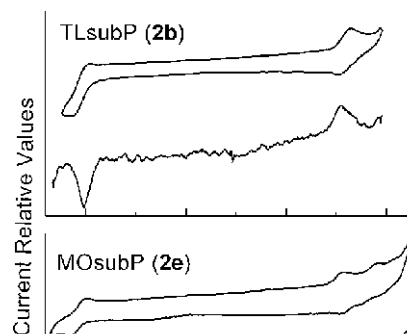

Fig. 46. Redox potentials obtained from DPV experiments on subPs
Рис. 46. Окислительно-восстановительные потенциалы, полученные из экспериментов DPV на subPs

For example, the redox couples of compounds having electron withdrawing groups appear at more positive potentials. The potential difference between the first oxidation and reduction is in the 2.52-2.64 V range (or 2.58±0.06 V), which is larger than those observed for *meso*-tetraarylporphyrins (*ca.* 2.25±0.05 V) [141], reflecting the ring contraction effect. This is consistent with the appearance of the UV-visible absorption bands at shorter wavelengths than those for the standard tetrapyrrole porphyrins (Fig. 47). Comparison of the redox potentials with those of ZnTPP (first oxid) 0.30 and (first redn) -1.75 V vs Fc+/Fc) [142] suggests that the HOMOs of the subPs are more stable, while the LUMOs are destabilized.

The electronic absorption and MCD spectra of all six monomeric subPs and (3PysubP)$_2$O (**3**) are displayed in Fig. 47, while Fig. 48 provides greater detail for the absorption spectra in the Q band region. The strong absorption in the 370-380 nm region is clearly similar to the Soret band of TPP and therefore almost certainly arises from a transition directly analogous to the B transition within Gouterman's four-orbital model [80]. This band appears at a shorter wavelength in the case of compounds with electron withdrawing substituents. The weaker absorption band in the 400-540 nm region can be assigned by direct inspection as almost certainly arising from a transition directly analogous to the Q transition within Gouterman's four-orbital model, since it is about an order of magnitude less intense. The Soret and Q bands, therefore, lie at considerably shorter wavelengths (*ca.* 30-50 and 70-100 nm, respectively) than the corresponding bands in the spectra of metallotetraphenylporphyrins (*ca.* 410-420 and 500- 610 nm) [80].

The absorption coefficient of the Soret band is *ca.* 25% that of ZnTPP in the same solvent [135b]. The absorption spectra of the six subPs are generally similar in shape, with the exception of the Q_{00} band where there is greater intensity for compounds with electron donating *meso*-substituents (Fig. 48). The weak Q_{00} intensity is related to the fact that the first and second HOMOs and LUMOs are degenerate or near degenerate. In the context of tetrapyrrole porphyrins, Gouterman's four-orbital model predicts that this results in a π-system, which mimics that of a D_{16h} symmetry cyclic polyene, by having an allowed B and a forbidden Q band based on orbital angular momentum changes of $\Delta M_L = \pm 1$ and ± 9, respectively [80]. It is known that the Q_{00} bands of TPPs are generally weaker than those of octaethylporphyrins where there is greater separation of the first and second HOMOs. As a result, in TPPs, generally the Q_{00} band is weaker than the Q_{01} vibrational band, while, in OEPs, the Q_{00} and Q_{01} band have comparable intensities.

In contrast with the electronic absorption spectra, the MCD spectra differ markedly from compound to compound. Although the absorption coefficient ratio of the Soret band to Q band in the absorption spectra is about 10:1, the relative Q band intensities in the MCD spectra are much larger, thus reflecting the greater orbital angular momentum associated with the excited state of a forbidden $\Delta M_L = \pm 7$ transition (by analogy with Gouterman's four-orbital model for standard tetrapyrrole porphyrins). The MCD spectra of the Q band region can be divided into two distinct groups. The subPs with electron donating groups show an intense -ve/+ve pattern in ascending energy (i.e. positive Faraday A term), while those with electron withdrawing groups are more complex with a concomitant decrease in intensity. The Soret band region MCD spectra can be divided into groups on a similar basis. The spectra of subPs with electron donating groups such as 4-methoxy and tolyl groups contain a -ve/+ve pattern as in the Q band region, while in contrast the spectra of subPs with electron withdrawing groups such as pyridyl and 4-(trifluoromethyl)phenyl contain a +ve/-ve pattern (i.e., a negative Faraday A term) [143]. In addition, careful inspection reveals that the -ve/+ve Soret MCD pattern observed for MOsubP (**2e**) changes gradually on going to TLsubP (**2b**) and then to PhsubP (**2a**). That is to say, the relative intensity of the positive envelope at higher energy becomes weaker, so that, in PhsubP, only the negative trough is observed. On going further to 3PysubP (**2d**), a positive MCD envelope develops at lower energy, and this intensifies in the case of TFsubP (**2f**), to the point in the case of 4PysubP (**2c**) that the positive and negative MCD envelopes
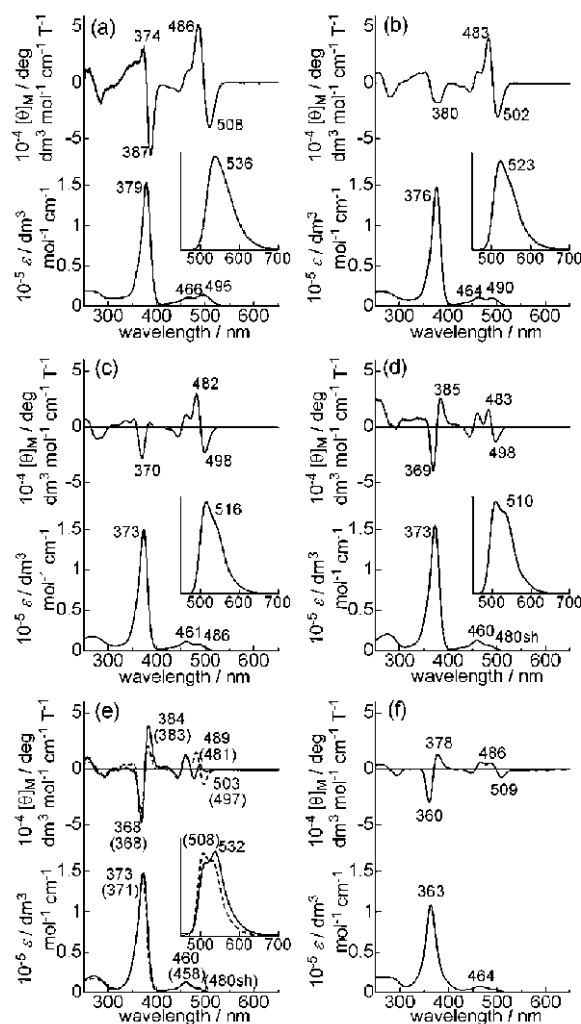
Fig. 47. Electronic absorption, MCD, and fluorescence spectra of (a) MOsubP (**2e**), (b) TLsubP (**2b**), (c) PhsubP (**2a**), (d) TFsubP (**2f**), (e) 3PysubP (**2d**) (broken lines) and 4PysubP (**2c**) (solid lines), and (f) (3PysubP)₂O (**3**) in CHCl₃ (absorption and MCD) and in EtOH (fluorescence)

Рис. 47. Спектры электронного поглощения, MCD и флуоресценции (a) MOsubP (**2e**), (b) TLsubP (**2b**), (c) PhsubP (**2a**), (d) TFsubP (**2f**), (e) 3PysubP (**2d**) (прерывистые линии) и 4PysubP (2c) (сплошные линии) и (f) (3PysubP)₂O (**3**) в CHCl₃ (поглощение и MCD) и в EtOH (флуоресценция)

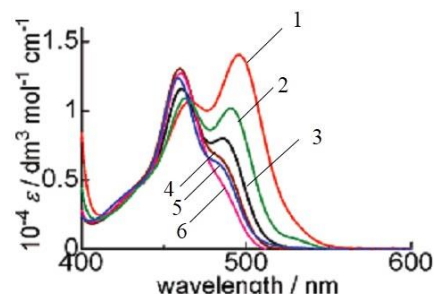Fig. 48. Electronic absorption spectra in the Q band region of: 1- MOsubP (**2e**), 2 - TLsubP (**2b**), 3 - PhsubP (**2a**), 4 - TFsubP (**2f**), 5 - 3PysubP (**2d**), and 6 - 4PysubP (**2c**) in CHCl₃

Рис. 48. Электронные спектры поглощения в области Q-полосы для 1 - MOsubP (**2e**), 2 - TLsubP (**2b**), 3 - PhsubP (**2a**), 4 - TFsubP (**2f**), 5 - 3PysubP (**2d**) и 6 - 4PysubP (**2c**) в CHCl₃

have almost equal intensities. These drastic changes in MCD patterns depending on substituents are highly unusual. In the cases of subPcs [144] and subAP [145], only positive A terms were observed for the Q_{00} and Soret bands. Although, as described above, the MCD signal in the Soret band region of the PhsubP spectrum is not a typical Faraday A term, the presence of first-derivative-shaped Q_{00} and Soret bands of the other compounds strongly suggests that the excited states are still orbitaly degenerate [146], as would be anticipated based on the effective C_3 symmetry of the subPs. These spectral sign anomaly of MCD of subPs were later after all theoretically elucidated to be due to the quenching of the magnetic moment of the LUMO by acceptor orbitals of the substituent [147].

MO calculations were performed for substituent-free subP, MOsubP (**2e**), PhsubP (**2a**), and 4PysubP (**2c**). The results were compared to those derived for ZnTPP calculated under the same conditions. Figure 49 provides a comparison of the frontier MOs and energy levels of ZnTPP and PhsubP (**2a**). The second HOMO (a_{1u}), first HOMO (a_{2u}), and LUMO (e_{gx}, e_{gy}) of the D_{4h} symmetry ZnTPP complex transform under the C_{3V} symmetry of PhsubP (**2a**) as a_1, a_2, and e, respectively. Since the inner ligand perimeter of subP contains a 12-atom 14-π-electron system, the $n = 3$ condition is satisfied in terms of the $4n+2$ aromaticity rule. Three sets of alternating nodes are observed for the first HOMO and second HOMO, while four sets of alternating nodes are observed for the LUMOs of PhsubP (**2a**).
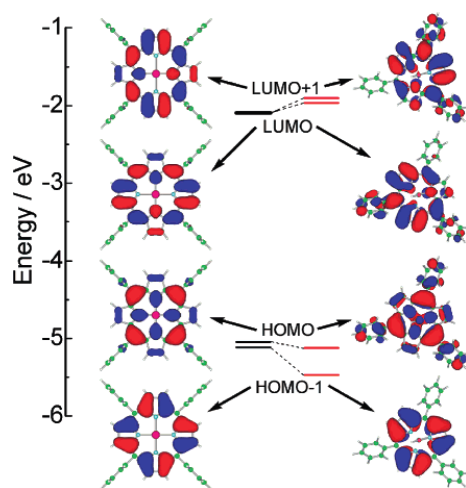

Fig. 49. Calculated frontier MOs and MO energies of ZnTPP and PhsubP (**2a**). Note that there is almost no electron density on the phenyl group of ZnTPP, while the LUMOs and HOMO of PhsubP (**2a**) are fully delocalized to the phenyl group

Рис. 49. Расчетные граничные МО и энергии МО ZnTPP и PhsubP (**2a**). Обратите внимание, что на фенильной группе ZnTPP электронная плотность почти отсутствует, в то время как LUMO и ВЗМО PhsubP (**2a**) полностью делокализованы в фенильную группу

This explicitly demonstrates that subPs can indeed be viewed as ring-contracted porphyrins and can be analyzed based on Gouterman's four-orbital model [80], since four and five sets of alternating nodes are observed for the corresponding MOs of metal porphyrin complexes based on the orbital angular momentum properties of the 16-atom 18-π-electron inner ligand perimeter. As would be anticipated based on the redox data, the LUMOs of PhsubP (**2a**) are destabilized while the first HOMO and second HOMO are stabilized relative to the four frontier π-MOs of ZnTPP. As can be demonstrated from the size of the MO coefficients (not shown), the HOMO and LUMOs of PhsubP (**2a**) are delocalized over the phenyl moiety, while the corresponding coefficients are almost zero in the case of the phenyl moieties of ZnTPP. There is clearly a much larger interaction between the central subP or porphyrin π-system and the phenyl moieties in the case of the subP systems. Several reasons can be inferred for this phenomenon. (i) In the case of TPPs, the angles reported between the phenyl group and porphyrin plane have consistently been greater than 70° [140] due to the steric hindrance between the hydrogen atoms at the ortho positions of the phenyl groups and those at the β-pyrrole positions. This effect was reproduced in the optimized structures in our DFT calculations with the rotational barrier calculated to be *ca.*150 kcal·mol^{-1} per phenyl group. In contrast, the corresponding angle was predicted to be in the 45°-55° range in the case of the triphenylsubporphyrins, since the steric hindrance is reduced. The distances between hydrogens at the *ortho*-positions of the phenyl groups and the β−pyrrole protons are significantly longer in the case of subPs, and the calculated rotational barrier is, therefore, reduced to *ca.*20 kcal mol^{-1} per phenyl group. If this prediction is accurate, the π-π interactions between the $2p_z$ carbon atomic orbitals of the *meso*-phenyl groups and the main subP π-system must become larger. (ii) The subP ligand is substantially smaller than the porphyrin tetrapyrole structure so the HOMO-LUMO energy gap of the phenyl groups is expected to be closer to that of subP (3.156 eV) than to that of tetraphenylporphyrin (2.951 eV).

In Fig. 50, the energy levels of the frontier π-MOs of four of the subPs are compared. Since the B-O-H (OH) axial ligand) angle is not 180°, the first LUMO and second LUMO have slightly different energies. The energy gap is 0.048-0.065 eV. The MO energies are stabilized on going from the electron rich MOsubP (**2e**) compound to PhsubP (**2a**), and still further to the electron deficient 4PysubP (**2c**), since the electronic repulsion between the subP π-system and the aryl groups decreases in this order. In particular, the

extent of stabilization of the first HOMO is more marked than that of the second HOMO, since there are large coefficients at *meso*-positions, thereby making the first HOMO-second HOMO energy gap smaller for subPs with electron withdrawing aryl groups. It should be noted that there is no coefficient at the *meso* position of the second HOMO. This is the reason that the Q_{00} bands of (trifluoromethyl)phenyl- and the pyridylsubporphyrins are weak. The first HOMO- second HOMO energy gap of MOsubP (**2e**), PhsubP (**2a**), and 4PysubP (**2c**) are calculated to be 0.51, 0.35, and 0.21 eV, respectively (the Q_{00} bands are stronger the larger the difference between the HOMO and HOMO-1) [80]. Comparison of the substituent-free subP and PhsubP (**2a**) data suggests that the a_2 MO is destabilized by *meso*-phenyl substitution. This has been reported previously in the case of tetrapyrole porphyrins and TPPs [80].
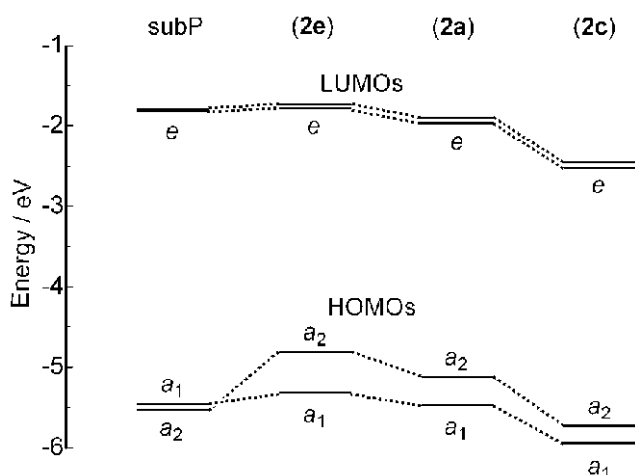

Fig. 50. Energies calculated for the frontier π-MO levels of unsubstituted subP, MOsubP (**2e**), PhsubP (**2a**), and 4PysubP (**2c**). The second LUMO- first LUMO energy gap is always less than 0.07 eV, while the first HOMO- second HOMO energy gap values are 0.075, 0.506, 0.348, and 0.211 eV, respectively
Рис. 50. Энергии, рассчитанные для граничных уровней π-МО незамещенного subP, MOsubP (**2e**), PhsubP (**2a**) и 4PysubP (**2c**). Вторая LUMO-первая энергетическая щель LUMO всегда меньше 0,07 эВ, в то время как первая HOMO-вторая энергетическая щель HOMO составляет 0,075, 0,506, 0,348 и 0,211 эВ соответственно

Through this study, the synthesis of six *meso*-triarylsubPs in *ca.* 4-8% yield was reported for the first time, which was based on adding tripyrrolylborane to refluxing propionic acid containing arylaldehyde. The main byproduct was a boron dipyrromethene with two methylphenyl moieties at the terminal α-positions. All six subPs show Soret and Q band-like absorption bands in the 370-380 and 400-540 nm regions, respectively, and these bands could be interpreted on the basis of MO calculations within the conceptual framework of Gouterman's four-orbital model [80]. The MCD spectra are characteristic of porphyrin congeners, but the Soret band region MCD spectra are markedly different from those of tetrapyrrole porphyrins, since the Faraday A terms change their sign from -ve/+ve for subPs with electron donating aryl groups to +ve/-ve for subPs with electron withdrawing *meso*-aryl groups. SubPs in this study exhibit green fluorescence in the 490-620 nm region, and their quantum yields were 0.10-0.12 in benzene and 0.06-0.07 in ethanol, which are larger than that for ZnTPP (0.03 in benzene) and comparable to that of metal-free tetraphenylporphyrin (0.11 in benzene) [39, 148]. IR spectra were assigned on the basis of DFT calculations. The difference in potential between the first oxidation and reduction steps is *ca.* 2.6 V, which is larger than those of conventional porphyrins (2.25±0.05 V) [141], reflecting the smaller π-conjugated system.

b) A Facile One-Pot Synthesis of meso-Aryl-Substituted [14] Triphyrin(2.1.1) [149]

All subporphyrins reported till 2007 contained a boron atom and consist of three pyrrole rings connected by three *meso*-carbons. In 2008, we reported the facile synthesis of a series of *meso*-aryl-substituted [14]triphyrin(2.1.1) and [14]benzotriphyrin(2.1.1) compounds (Scheme 9). These compounds were unprecedented in porphyrinoid research since they represented the first examples of near planar metal-free contracted porphyrinoids with 14 π-electron aromatic systems containing only the standard pyrrole and isoindoline moieties of the porphyrins and tetrabenzoporphyrins. The insertion of a second sp²-hybridized carbon atom between one of the three neighboring pairs of pyrroles eliminates the need for a central boron atom.
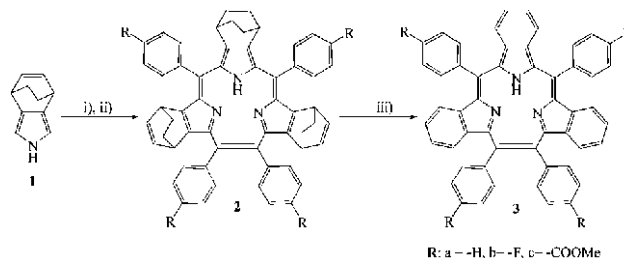
Scheme 9. Synthesis of *meso*-aryl-substituted [14]triphyrin(2.1.1).
Reagents and conditions: (i) p-RC6H4CHO, BF3· Et2O, CH2Cl2, room temp, 12 h; (ii) p-chloranil, 2 h; (iii) 220 °C, 2 mmHg, 20 min
Схема 9. Синтез мезоарилзамещенного [14] трифирина(2.1.1).
Реагенты и условия: (i) RC6H4CHO, BF3· Et2O, CH2Cl2, комнатная температура, 12 ч; (ii) п-хлоранил, 2 часа; (iii) 220 ° С, 2 мм рт.ст., 20 мин

We initially prepared *meso*-aryl-substituted [14] triphyrin(2.1.1) serendipitously during a BF3•Et2O catalyzed Rothemund condensation of 4,7-dihydro-4,7-ethano-2*H*-isoindole (**1**) with aryl aldehyde in dichloromethane, Scheme 9, which was followed by an oxidation with *p*-chloranil. After silica gel column chromatography, **2a-c** ((aryl)phenyl **2a**, 4-fluorophenyl **2b**, and 4-methylbenzoatephenyl **2c**) can be isolated in ca. 35% yield. The corresponding [14] benzotriphyrin(2.1.1) compounds **3a-c** can be formed

40

Изв. вузов. Химия и хим. технология. 2019. Т. 62. Вып. 4

quantitatively based on a retro Diels-Alder reaction of the bicyclo[2.2.2]octadiene (BCOD) rings by heating **2a-c** at 220 °C under vacuum (2 mmHg) for 20 min.

The triphyrin structures were determined definitively by X-ray structural analysis of single-crystals of **2a** and **3a**, which were obtained by slow diffusion of hexane into the CH_2Cl_2 solution. The triphyrin macrocycle is near planar, Fig. 51. The mean deviations of the ring atoms are 0.1077 Å for **2a** and 0.1309 Å for **3a**. In both **2a** and **3a**, the *meso*-phenyl rings are inclined 67.0°, 53.8°, 83.2°, and 86.5° with respect to the triphyrin mean plane. These values are larger than the phenyl dihedral angles that have been reported for the subporphyrins (ca. 50.3°) [135], perhaps due to the greater steric hindrance caused by the presence of fused BCOD or benzene rings at the β-pyrrole positions.
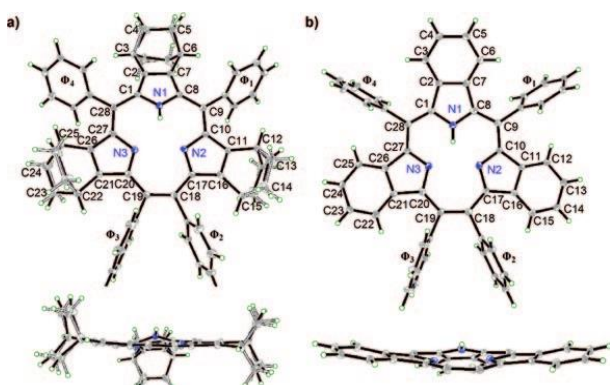

Fig. 51. The crystal structures of **2a** (a) and **3a** (b) with 50% probability thermal ellipsoids (top, perspective view; below, side view with phenyl groups omitted)
Рис. 51. Кристаллические структуры **2a** (a) и **3a** (b) с тепловыми эллипсоидами вероятности 50% (вид сверху, в перспективе; внизу вид сбоку с пропущенными фенильными группами)

The average bond length between the *meso*-carbon atoms and the phenyl rings was 1.505 Å for **2a** and 1.498 Å for **3a**. The pyrrole rings are tilted relative to the triphyrin mean plane by 20.1°, 4.3°, and 6.7° in the case of **2a** and 16.6°, 7.5°, and 6.7° in the case of **3a**. The peripheral bond distances of **2a** and **3a** are very close to the values reported for subporphyrins with the exception of the pyrrole(β)-pyrrole(β) distance in **3a** (ca. 1.42 Å), which is significantly longer. The π-conjugation system is highly delocalized. For example, the C18-C19 bond between the two carbons bridging neighboring pyrroles (1.407 Å in **2a** and 1.423 Å in **3a**) is similar in length to the C19-C20 (1.424 Å in **2a** and 1.423 Å in **3a**) and C_{17}-C_{18} bonds (1.438 Å in **2a** and 1.423 Å in **3a**). This, in turn, suggests that there is rapid exchange between the two NH tautomers in the solid state, Fig. 52 and that the inner NH proton forms part of a three-centered hydrogen bond. The average N-N distances (2.573 Å for **2a** and 2.578 Å for **3a**) lie in the range anticipated for a very strong hydrogen-bond interaction.
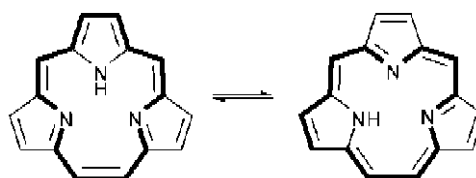
Fig. 52. NH tautomers of [14] triphyrin(2.1.1)
Рис. 52. NH-таутомеры [14] трифирина (2.1.1)

The singlet NH resonance was determined to lie at 7.68 ppm in the ^1H NMR spectrum of **2c** in $CDCl_3$. With the exception of three broad singlet peaks at 3.63, 3.35, and 2.47 ppm, which are associated with the bridge head of three bicyclo[2.2.2]octadiene groups, the other signals of the peripheral protons lie in the 7-9 ppm range, reflecting the 14 π-electron aromatic pathway of the triphyrin macrocycle. In the ^1H NMR spectrum of **3c**, the peaks associated with the bicyclo[2.2.2]octadiene (bridge head, bridge, and olefin) groups are replaced by new peaks associated with the fused benzene rings. The identification of the NH proton resonance ($\delta = 8.16$ ppm) is straightforward based on the COSY NMR spectrum, since it is not scalar coupled to any other proton resonance. The inner NH resonances lie at remarkably low field (7.68 ppm). The strong hydrogen bonding probably compensates for the diamagnetic ring-current effect.

Fig. 53. MCD (top) and UV-visible absorption spectra (bottom) of **2a** and **3a** in $CHCl_3$
Рис. 53. MCD (вверху) и УФ-видимые спектры поглощения (внизу) **2a** и **3a** в $CHCl_3$

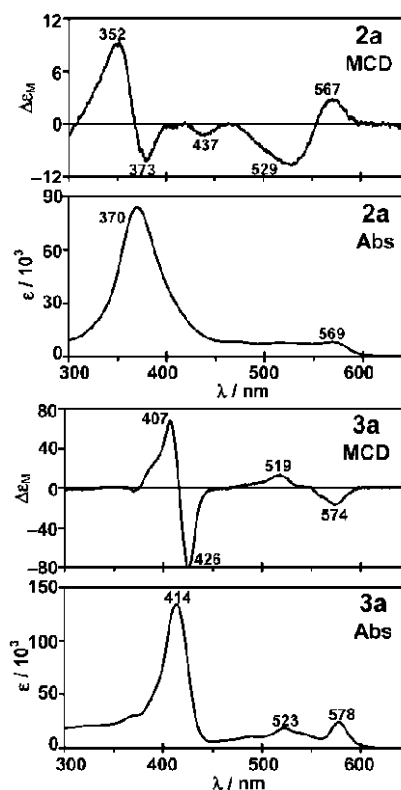The UV-visible absorption spectra of **2a** and **3a**, Fig. 53, contain intense bands at 370 and 414 nm, respectively, and weaker bands in the 500-600 nm region in a pattern similar to the B (or Soret) and Q bands of the porphyrins. Similar absorption band data were obtained for **2b**, **2c**, **3b**, and **3c** (not shown). The MCD spectra are dominated by coupled pairs of oppositely signed Gaussian-shaped Faraday $\mathcal{B}$ terms, similar to those observed for the Q and B bands of low symmetry porphyrins and phthalocyanines [22]. The relative intensification of the visible region bands of **2a** in the MCD spectrum is comparable to that observed for the Q bands of porphyrins based on Gouterman's four-orbital model [80].

In conclusion, we successfully synthesized a series of *meso*-aryl substituted [14]triphyrins(2.1.1) in moderate yield from mild Rothemund porphyrin condensation reactions and the corresponding [14]benzotriphyrin(2.1.1) compounds based on retro Diels-Alder reactions. These compounds represented the first examples of free-base contracted porphyrinoids with 14 π-electron aromatic systems containing only the pyrrole and isoindoline moieties of the porphyrins and tetrabenzoporphyrins.

REFERENCES
ЛИТЕРАТУРА

1. **Broun A., Tcherniac J.** Uber die Produkte der Einwirkung von Acetanhydrid auf Phthalamid. *Ber. Deut. Chem. Ges.* 1907. V. 40. P. 2709-2714.
2. **Kobayashi N.** Synthesis, Optical Properties, Structures, and Molecular Orbital Calculations of Subazaporphyrin, Subphthalocyanine, Subnaphthalocyanines, and Related Compounds. *J. Porphyrins and Phthalocyanines.* 1999. V. 3. P. 453-467.
3. **Kobayashi N.** Phthalocyanines. *Current Opinion in Solid State & Materials Science.* 1999. V. 4. P. 345-353.
4. **Kobayashi N.** Phthalocyaninato Macrocyclic Molecules-Macromolecules Applied in Various Fields. *Kagaku to Kogyou (Chemistry and Industry).* 1999. V. 52. P. 968-971.
5. **Ishii K., Kobayashi N.** The Excited Multiplet States of Metalloporphyrins and Metallophthalocyanines Coordinated or Linked to Nitroxide Radicals. *Coord. Chem. Rev.* 2000. V. 198. P. 231-250.
6. **Kobayashi N., Konami H.** Molecular Orbitals and Electronic Spectra of Benzo-Fused and Related Porphyrin Analogues. *J. Porphyrins and Phthalocyanines.* 2001, V. 5, P. 233-255.
7. **Kobayashi N.** Optically Active Phthalocyanines. *Coord. Chem. Rev.* 2001. V. 221/222. P. 99-123.
8. **Kobayashi N.** Dimers, Trimers, and Oligomers of Phthalocyanines and Related Compounds. *Coord. Chem. Rev.* 2002. V. 227. P. 129-152.
9. **Kobayashi N.** Design, Synthesis, Structure, and Spectroscopic and Electrochemical Properties of Phthalocyanines. *Bull. Chem. Soc. Jpn. (Accounts)* 2002. V. 75. P. 1-19.
10. **Kobayashi N.** Porphyrins and Phthalocyanines as They are (in Japanese). *Bull. Jpn. Soc. Coord. Chem.* 2002. V. 39. P. 26-30.
11. **Kobayashi N., Leznoff C.C.** Synthesis, Structure and Properties of New Phthalocyanines. *J. Porphyrins and Phthalocyanines.* 2004. V. 8. P. 1015-1019.
12. **Kobayashi N.** Metal Complexes of Macrocyclic π Systems (in Japanese). *Kagaku to Kyouiku (Chemistry and Education).* 2004. V. 52. P. 28-29.
13. **Kobayashi N., Fukuda T.** Leading-Edge Research on Phthalocyanines (in Japanese). *Kagaku Kougyou (Chemical Industry).* 2004. V. 55. P. 771-777.
14. **Muranaka, A., Okuda M., Kobayashi N.** Recognition of Chiral Catechols Using Oxo-Titanium Phthalocyanine (in Japanese). *Shokuhin-Shokuhin Tenkabutsu Kenkyushi (Foods & Food Ingredients J. Jpn).* 2005. V. 210. P. 849-853.
15. **Kobayashi N., Muranaka A.** High Precision Analysis of Molecular Electronic Structures of Organic Molecules by CD and MCD Spectroscopy. *Yuki Gousei Kagaku Kyoukaishi (Journal of Synthetic Organic Chemistry, Japan).* 2006. V. 64. P. 735-743.
16. **Mack J., Stillman M. J., Kobayashi N.** Application of MCD Spectroscopy to Porphyrinoids. *Coord. Chem. Review.* 2007. V. 251. P. 429-453.
17. **Kobayashi N., Nakai K.** Applications of Magnetic Circular Dichroism Spectroscopy to Porphyrins and Phthalocyanines. *Chem. Commun. (Feature Article).* 2007. P. 4077-4092.
18. **Fukuda T., Kobayashi N.** Hydrogenated Tetraazaporphyrins - Old but New Core-Modified Phthalocyanine Analogues. *Dalton Trans. (Perspective).* 2008. P. 4685-4704.
19. **Kobayashi N., Fukuda T.** Phthalocyanine, Porphyrin, Cyclodextrin, and Polymer Systems Suitable for Studying by Circular Dichroism, Magnetic Circular Dichroism, and/or Electrochemistry. *Bull. Chem. Soc. Jpn. (Award Account).* 2009. V. 82. P. 631-663.
20. **Shimizu S., Kobayashi N.** Porphyrin Analogues that Realize Higher Oxidation State of Central Metal. *Kagaku (Chemistry).* 2009. V. 64. P. 64-65.
21. **Yoshimoto S., Kobayashi N.** Supramolecular Nanostructures of Phthalocyanines and Porphyrins at Surfaces Based on the "Bottom-up Assembly". *Structure and Bonding.* 2010. V. 135. P. 137-168.
22. **Mack J., Kobayashi N.** Low Symmetry Phthalocyanines and Their Analogues. *Chem. Rev.* 2011. V. 111. P. 281-321.
23. **Shimizu S., Kobayashi N.** Structurally-Modified Subphthalocyanines: Molecular Design towards Realization of Expected Properties from the Electronic Structure and Structural Features of Subphthalocyanine. *Chem. Commun. (feature article).* 2014. V. 50. P. 6949-6966.
24. **Furuyama T., Kobayashi N.** Design, Synthesis, and Properties of Azaporphyrin Phosphorus Complexes. *Yuki Gousei Kagaku Kyoukaishi (Journal of Synthetic Organic Chemistry, Japan).* 2015. V. 73. P. 833-843.
25. **Kobayashi N.** Properties of Phthalocyanines and Porphyrins Deduced from Their Molecular Orbitals. *Gendai Kagaku (Chemistry of Present Days), Tokyo Kagaku Dojin.* 2016. V. 539. P. 30-35.
26. **Lu H., Kobayashi N.** Optically Active Porphyrin and Phthalocyanine Systems. *Chem. Rev.* 2016. V. 116. P. 6184-6261.
27. **Hoshi H., Kobayashi N.** Spectroscopic and Structural Properties of Phthalocyanines Deduced from Their Frontier Molecular Orbitals (MOs) and MO Calculations. *Coord. Chem. Rev.* 2017. V. 345. P. 31-41.
28. **Furuyama T., Kobayashi N.** Azaporphyrin Phosphorus(V) Complexes: Synthesis, Structure, and Modification of Optical Properties. *PCCP.* 2017. V. 19. P. 15596-15612.

29. **Kobayashi N.** Synthesis and Spectroscopic Properties of Phthalocyanine Analogues. In "Phthalocyanines-Properties and Applications". Ed by C.C. Leznoff and A.B.P. Lever. V. II. Chap. 3 (pp. 97-161). New York, Weinheim, Cambridge: VCH. 1992.

30. **Kobayashi N., Konami H.** Electronic Spectra and Molecular Orbitals of Phthalocyanines. In"Phthalocyanines - Properties and Applications". Ed by C.C. Leznoff and A.B.P. Lever. V. IV. Chap. 6 (pp. 343-404). New York, Weinheim, Cambridge: VCH. 1996.

31. **Kobayashi N.** Synthesis of Starting Materials of Phthalocyanines and Metal-Free Phthalocyanines. In "Phthalocyanine-Kagaku to Kinou- (Phthalocyanines-Chemistry and Functions)". Ed. by N. Kobayashi, H. Shirai. Sections 1.1 and 1.2 (pp. 1-20). Tokyo: IPC. 1997. (in Japanese).

32. **Kobayashi N.** Synthesis of Starting Materials of Phthalocyanine Congeners. In "Phthalocyanine-Kagaku to Kinou- (Phthalocyanines-Chemistry and Functions)". Ed. by N. Kobayashi and H. Shirai. Section 1.4 (pp. 28-39). Tokyo: IPC. 1997. (in Japanese).

33. **Kobayashi N.** Synthesis of Phthalocyanine Congeners. In "Phthalocyanine-Kagaku to Kinou- (Phthalocyanines-Chemistry and Functions)". Ed. by N. Kobayashi and H. Shirai. Section 1.5 (pp. 39-45). Tokyo: IPC. 1997. (in Japanese).

34. **Koyama T., Shirai H., Kobayashi N.** Langmuir and Blodgett Films of Phthalocyanines. In "Phthalocyanine-Kagaku to Kinou- (Phthalocyanines-Chemistry and Functions)". Ed. by N. Kobayashi, H. Shirai. Section 2.5 (pp. 108-119). Tokyo: IPC. 1997. (in Japanese).

35. **Kobayashi N.** Electrochemistry of Phthalocyanines. In "Phthalocyanine-Kagaku to Kinou- (Phthalocyanines-Chemistry and Functions)". Ed. by N. Kobayashi, H. Shirai. Section 4.1.1 (pp. 183-196). Tokyo: IPC. 1997. (in Japanese).

36. **Kobayashi N.** Phthalocyanine as Electrocatalysts. In "Phthalocyanine-Kagaku to Kinou- (Phthalocyanines-Chemistry and Functions)". Ed. by N. Kobayashi, H. Shirai. Section 5.2 (pp. 290-301). Tokyo: IPC. 1997. (in Japanese).

37. **Kobayashi N.** meso-Azaporphyrins and Their Analogues. In "Handbook of Porphyrins and Related Macrocycles". Ed. by K.M. Kadish, K.M. Smith, R. Guilard. V. 2. Chap. 13 (pp. 301-360). New York: Academic Press. 1999.

38. **Kobayashi N.** Synthesis and Spectroscopic Properties of Phthalocyanine Analogues. In "Handbook of Porphyrins and Related Macrocycles". Ed. by by K.M. Kadish, K.M. Smith, R. Guilard. V. 15. Chap.100 (pp. 161-262). New York: Academic Press. 2002.

39. **Ishii K., Kobayashi N.** The Photophysical Properties of Phthalocyanines and Related Compounds. In "Handbook of Porphyrins and Related Macrocycles". Ed. by K.M. Kadish, K.M. Smith, R. Guilard. V. 16. Chap. 102 (pp. 1-42). New York: Academic Press. 2002.

40. **Kobayashi N., Fukuda T.** Phthalocyanines. In "Lecture on Experimental Chemistry". Ed. by Chem. Soc. of Jpn. V. 22. Section 3.3.5 (pp. 452-460). Tokyo: Maruzen. 2004. (in Japanese).

41. **Fukuda T., Kobayashi N.** Deformed Phthalocyanines. In "Phthalocyanines as Functional Dyes". Ed by R. Hirohashi, K. Sakamoto, E. Okumura. Section 2.4.3 (pp. 68-70). Tokyo: IPC. 2004. (in Japanese).

42. **Fukuda T., Kobayashi N.** Chemical Structure of Phthalocyanines. In "Phthalocyanines as Functional Dyes". Ed by R. Hirohashi, K. Sakamoto, E. Okumura. Section 3.1 (pp. 79-103). Tokyo: IPC. 2004. (in Japanese).

43. **Ishii K., Kobayashi N.** Electronic Structure and Photophysical Properties of Phthalocyanines. In "Phthalocyanines as Functional Dyes". Ed by R. Hirohashi, K. Sakamoto, E. Okumura. Sections 3.2 and 3.3 (pp. 103-122). Tokyo: IPC. 2004. (in Japanese).

44. **Ishii K., Kobayashi N.** Solid State Spectra of Phthalocyanines. In "Phthalocyanines as Functional Dyes". Ed by R. Hirohashi, K. Sakamoto, E. Okumura. Section 4.3 (pp. 199-204). Tokyo: IPC. 2004. (in Japanese).

45. **Fukuda T., Kobayashi N.** Magnetic Circular Dichroism Spectra of Phthalocyanines. In "Phthalocyanines as Functional Dyes". Ed by R. Hirohashi, K. Sakamoto, E. Okumura. Section 4.4 (pp. 204-219). Tokyo: IPC. 2004. (in Japanese).

46. **Kobayashi N., Yoshimoto Y.** Electrochemistry and Electron Transfer of Phthalocyanines. In "Phthalocyanines as Functional Dyes". Ed by R. Hirohashi, K. Sakamoto, E. Okumura. Chapter 7 (pp. 279-293). Tokyo: IPC. 2004. (in Japanese).

47. **Kobayashi N., Fukuda T.** Phthalocyanine as Pigments. In "Bunsan Gijutsu Daizenshu". Section 4.6 (pp. 172-180). Tokyo: Joho Kikou. 2005. (in Japanese).

48. **Kobayashi N., Fukuda T.** Recent Progress in Phthalocyanine Chemistry: Synthesis and Chacterization. In "Functional Dyes". Ed by S. –H. Kim. Chap. 1 (pp. 1-47). Holland: Elsevier. 2005.

49. **Kobayashi N.** Progress in Phthalocyanine Synthesis. In "カラーフィルターにおける新しい材料開発と製造プロセス全集". Section 1.1 (pp. 3-23). Tokyo: Technical Information Institute. 2006. (in Japanese).

50. **Kobayashi N.** Oxygen Electrocatalysis. In "Encyclopedia of Electrochemistry". Ed by A.J. Bard, M. Stratman. V. 10 (Modified Electrode). Chap. 1 (pp. 687-694). Wiley-VCH. 2007.

51. **Kobayashi N.** Electrochromism. In "Inorganic Chemotropism". Ed. by Y. Fukuda. Chap. 7 (pp. 291-336). Tokyo, Heidelberg: Kodansha, Splinger. 2007.

52. **Kobayashi N.** Metallophthalocyanines. In "Kinousei Shikiso no Gousei to Ouyou (Synthesis and Applied Technology of Functional Dyes)". Ed. by M. Matsui. Chap. 4 (pp. 61-75). Tokyo: CMC. 2007. (in Japanese).

53. **Kobayashi N.** Optically Active Porphyrin Systems Analyzed by Circular Dichroism. In "Handbook of Porphyrin Science". Ed. by K.M. Kadish, K.M. Smith, R. Guilard. V. 7. Chap. 33 (pp. 147-245). Singapore: World Scientific. 2010.

54. **Fukuda T., Kobayashi N.** Electronic Absorption Spectra – Phthalocyanines. In "Handbook of Porphyrin Science". Ed. by K.M. Kadish, K.M. Smith, R. Guilard. V. 9. Chap. 42 (pp. 1-650). Singapore: World Scientific. 2010.

55. **Mack J., Kobayashi N.** Recent Applications of MCD Spectroscopy to Porphyrinoids. In "Multiporphyrin Arrays". Ed. by D. Kim Chapter 3 (pp. 91-147). Pan Stanford Publ. 2012.

56. **Mack J., Kobayashi N., Shen Z.** The Effect of Structural Modifications on the Properties of Porphyrinoids. In: "Handbook of Porphyrin Science". Ed. by K.M. Kadish, K.M. Smith, R. Guilard. Singapore: World Scientific. 2012. V. 23. Chapt. 109. P. 281-371.

57. **Snow A.W.** Phthalocyanine Aggregation. In "Handbook of Porphyrin Science". Ed. by K.M. Kadish, K.M. Smith, R. Guilard. V. 23, Chap. 109 (pp. 281-371). Singapore: World Scientific. 2012.

58. **Kobayashi N.** Synthesis and Characterization of Chiral Phthalocyanines. In "Handbook of Porphyrin Science". Ed. by K.M. Kadish, K. M. Smith, R. Guilard. V. 23. Chap. 110 (pp. 373-440). Singapore: World Scientific. 2012.

59. **Kobayashi N. Muranaka A., Mack J.** Circular Dichroism and Magnetic Circular Dichroism for Organic Chemists (textbook). London: Royal Society of Chemistry. 2012. (comments in Angew. Chem. Int. Ed. 2012, V. 51, P. 10446).

60. **Kobayashi N.** Porufirin oyobi Futaroshianin kei Shikiso (Porphyrinoid and Phthalocyaninoid Dyes). In "Kinou kei Shikiso no Kagaku (Science of Functional Dyes)". Ed by H. Nakasumi. Chap. 11. pp. 157-172. Tokyo: Kagakudojin. 2013.

61. **Shimizu S., Kobayashi N.** Creation of Novel Pi-Electron Systems Based on Phthalocyanines, In "Shinki Pai Kukan no Souhatsu to Kinou Kaihatsu (Creation and Functional Development of Novel Pi-Electron Systems)". Ed by T. Akaska, A. Osuka, S. Fukuzumi, H. Kandori, pp. 85-90. Tokyo: CMC. 2013.

62. **Shimizu S., Kobayashi N.** Recent Advances in the Chemistry of Phthalocyanine as Functional Chromophores. In "Chemical Science of π-Electron Systems". Ed by T. Akaska, A. Osuka, S. Fukuzumi, H. Kandori. pp. 273-291. Tokyo: Springer JP. 2015.

63. **Kobayashi N., Mack J., Ishii K., Stillman M.J.** Electronic Structure of Reduced Symmetry Peripheral Fused-Ring-Substituted Phthalocyanines. *Inorg. Chem.* 2000. V. 41. P. 5350-5363.

64. **Miwa H., Ishii K., Kobayashi N.** Electronic Structures of Zinc and Palladium Tetraazaporphyrin Derivatives Controlled by Fused Benzo Rings. *Chem. Eur. J.* 2004. V. 10.P. 4422-4435.

65. **Ishii K., Itoya H., Miwa H., Fujitsuka M., Ito O., Kobayashi N.** Relationship between Symmetry of Porphyrinic π-Conjugated Systems and Singlet Oxygen ($^1\Delta_g$) Yields: Low Symmetry Tetraazaporphyrin Derivatives. *J. Phys. Chem. A.* 2005. V. 109. P. 5781-5787.

66. **Miwa H., Makarova E.A., Ishii K., Luk'yanets E. A., Kobayashi N.** Spectroscopy, Electrochemistry, and Molecular Orbital Calculations of Metal-Free Tetraazaporphyrin, -chlorine, -bacteriochlorin, and -isobachteriochlorin. *Chem. Eur. J.* 2002. V. 8. P. 1082-1090.

67. **Firey P.A., Ford W.E., Sounik J.R., Kenney M.E., Rodgers M.A.J.** Silicon Naphthalocyanine Triplet State and Oxygen. A Reversible Energy-Transfer Reaction. *J. Am. Chem. Soc.* 1988. V. 110. P. 7626-7630.

68. **Aoudia M., Cheng G., Kennedy V.O., Kenney M.E., Rodgers M.A.J.** Synthesis of a Series of Octabutoxy- and Octabutoxybenzophthalocyanines and Photophysical Properties of Two Members of the Series. *J. Am. Chem. Soc.* 1997. V. 119. P. 6029-6039.

69. **Ishii K., Takeuchi S., Shimizu S., Kobayashi N.** A Concept for Controlling Singlet Oxygen ($^1\Delta_g$) Yields Using Nitroxide Radicals: Phthalocyaninatosilicon Covalently Linked to Nitroxide Radicals. *J. Am. Chem. Soc.* 2004. V. 126. P. 2082-2088.

70. **Turro N.J.** Modern Molecular Photochemistry. Mill Valley, California: University Science Books. 1991.

71. **Ishii, K., Kobayashi N.** The Photophysical Properties of Phthalocyanines and Related Compounds. In "The Porphyrin Handbook". Ed. by K.M. Kadish, R.M. Smith, R. Guilard. New York: Academic Press. 2003. V. 16. Chap. 102.

72. **van der Waals J.H., van Dorp W.G., Schaafsma T.J.** In The Porphyrins. Ed. by D. Dolphin. New York: Academic Press. 1978. V. 4. Chap. 3.

73. **van Dorp W.G., Schoemaker W.H., Soma M., van der Waals J.H.** The Lowest Triplet State of Free Base Porphyrin. *Mol. Phys.* 1975. V. 30. P. 1701-1721.

74. **Ishii K., Ishizaki T., Kobayashi N.** Experimental Evidence for a Selection Rule of Intersystem Crossing to the Excited Quartet States: Metallophthalocyanines Coordinated by 4-Amino-TEMPO. *J. Phys. Chem. A.* 1999. V. 103. P. 6060-6062.

75. **Ishii K., Abiko S., Kobayashi N.** Time-Resolved Electron Spin Resonance of Gallium and Germanium Porphyrins in the Excited Triplet State. *Inorg. Chem.* 2000. V. 39. P. 468-472.

76. **Kobayashi N., Togashi M., Osa T., Ishii K., Yamauchi S., Hino H.** Low Symmetrical Phthalocyanine Analogues Substituted with Three Crown Ether Voids and Their Cation-Induced Supermolecules. *J. Am. Chem. Soc.* 1996. V. 118. P. 1073-1085.

77. **Ishii K., Hirose Y., Kobayashi N.** Selective Populations from the Excited Multiplet States to the Triplet Ground State in a Phthalocyanine: A New Concept for Controlling Magnetic Properties by Photoexcitation. *J. Am. Chem. Soc.* 1998. V. 120. P. 10551-10552.

78. **Furuya F., Ishii K., Kobayashi N.** Direct EPR Observations of Both Oxidized and Reduced Porphyrin Dimers in the Lowest Excited States: A Novel Analysis of a Homobiradical with a Strong Antiferromagnetic Interaction. *J. Am. Chem. Soc.* 2002. V. 124. P. 12652-12653.

79. **Nakai K., Kurotobi K., Osuka A., Uchiyama M., Kobayashi N.** Electronic structures of azulene-fused porphyrins as seen by magnetic circular dichroism and TD-DFT calculations. *J. Inorg. Biochem.* 2008. V. 102. P. 466-471.

80. **Gouterman M.** In The Porphyrins. Ed. by D. Dolphin. New York: Academic Press. 1978. V. 3. Chap. 1.

81. **Michl J.** Magnetic Circular Dichroism of Cyclic. Pi.-electron Systems. 1. Algebraic Solution of the Perimeter Model for the A and B Terms of High-Symmetry Systems with a (4N+2) π-Electron [n] Annulene Perimeter. *J. Am. Chem. Soc.* 1978. V. 100. P. 6801-6811.

82. **Michl J.** Magnetic Circular Dichroism of Cyclic. Pi.-electron Systems. 2. Algebraic Solution of the Perimeter Model for the B Terms of Systems with a (4N +2) π-Electron [n] Annulene Perimeter. *J. Am. Chem. Soc.* 1978. V. 100. P. 6812-6818.

83. **Muranaka A., Homma S., Maeda H., Furuta H., Kobayashi N.** Detection of unusual ΔHOMO < ΔLUMO relationship in tetrapyrrolic cis- and trans-doubly N-confused porphyrins. *Chem. Phys. Lett.* 2008. V. 460. P. 495-498.

84. **Srinivasan A., Furuta H.** Confusion Approach. to Porphyrinoid Chemistry. *Acc. Chem. Res.* 2005. V. 38. P. 10-20.

85. **Furuta H., Maeda H., Osuka A.** Doubly N-Confused Porphyrin: A New Complexing Agent Capable of Stabilizing Higher Oxidation States. *J. Am. Chem. Soc.* 2000. V. 122. P. 803-807.

86. **Maeda H., Osuka A., Furuta H.** Trans Doubly N-Confused Porphyrins: Cu(III) Complexation and Formation of Rodlike Hydrogen-Bonding Networks. *J. Am. Chem. Soc.* 2003. V. 125. P. 15690-15691.

87. **Shimizu S., Haseba Y., Yamazaki M., Kumazawa G., Kobayashi N.** Control of Chromophore Symmetry by Positional Isomerism of Peripheral Substituents. *Chem. Eur. J.* 2014. V. 20. P. 4822-4828.

88. **Furuyama T., Yoshida T., Hashizume D., Kobayashi N.** Phosphorus(V) tetraazaporphyrins: Porphyrinoids Showing an Exceptionally Strong CT Band between the Soret and Q bands. *Chem. Sci.* 2014. V. 5. P. 2466-2474.

89. **Kobayashi N., Nakajima S., Osa T.** Spectroscopy, Electrochemistry, and Spectroelectrochemistry of Tetra-tert-Butylated and Octaphenylated Tetraazaporphyrins. **Chem. Lett.** 1992. P. 2415-2418.

90. **Fukuda T., Masuda S., Kobayashi N.** Tetraazachlorin-Fullerene Conjugates: On-Off Control of Electronic Communication Enabled by Push-Pull Substituents. *J. Am. Chem. Soc.* 2007. V. 129. P. 5472-5479.

91. **Wu F., Liu J., Mishra P., Komeda T., Mack J., Chang Y., Kobayashi N., Shen Z.** Modulation of the Molecular Spintronic Properties of Adsorbed Copper Corroles. *Nature Commun.* 2015. V. 6. 7547. DOI: 10.1038/ncomms8547.

92. **Rocha A.R., García-Suárez V.M., Bailey S.W., Lambert C.J., Ferrer J., Sanvito S.** Towards Molecular Spintronics. *Nat. Mater.* 2005. V. 4. P. 335–339.

93. **Irie M.** Photochromism: memories and switches introduction. *Chem. Rev.* 2000. V. 100. P. 1683–1684.

94. **Yamase T.** Photo- and Electrochromism of Polyoxometalates and Related Materials. *Chem. Rev.* 1998. V. 98. P. 307–326.

95. **Vincent R., Klyatskaya S., Ruben M., Wernsdorfer W., Balestro F.** Electronic Read-Out of a Single Nuclear Spin Using a Molecular Spin Transistor. *Nature.* 2012. V. 488. P. 357–360.

96. **Chang Y., Chen H., Zhou Z., Zhang Y., Schutt C., Herges R., Shen Z.** A 20π-electron Heteroporphyrin Containing a Thienopyrrole Unit. *Angew. Chem. Int. Ed.* 2012, V. 124. P. 12973–12977.

97. **Ghosh A., Wondimagegn T., Parusel A.B.** Electronic Structure of Gallium, Copper, and Nickel Complexes of Corrole. High-Valent Transition Metal Centers versus Non-Innocent Ligands. *J. Am. Chem. Soc.* 2000. V. 122. P. 5100–5104.

98. **Bro'ring M., Bregier F., Consul Tejero E., Hell C., Holthausen M.C.** Revisiting the Electronic Ground State of Copper Corroles. *Angew. Chem. Int. Ed.* 2007. V. 46. P. 445–448.

99. **Alemayehu A.B., Gonzalez E., Hansen L. K., Ghosh A.** Copper Corroles are Inherently Saddled. *Inorg. Chem.* 2009. V. 48. P. 7794–7799.

100. **Pierloot K., Zhao H., Vancoillie S.** Copper Corroles: The Question of Noninnocence. *Inorg. Chem.* 2010. V. 49. P. 10316–10329.

101. **Kondo J.** Effect of Ordinary Scattering on Exchange Scattering from Magnetic Impurity in Metals. *Phys. Rev.* 1968. V. 169. P. 437–440.

102. **Fano U.** Effects of Configuration Interaction on Intensities and Phase Shifts. *Phys. Rev.* 1961. V. 124. P. 1866–1878.

103. **Kobayashi N., Lever A.B.P.** Cation or Solvent-Induced Supermolecular Phthalocyanine Formation: Crown Ether Substituted Phthalocyanines. *J. Am. Chem. Soc.* 1987. V. 109. P. 7433–7441.

104. **Kadish K.M., Adamian V.A., Caemelbecke E.V., Gueletii E., Will S., Erben C., Vogel E.** Electrogeneration of Oxidized Corrole Dimers. Electrochemistry of (OEC) M Where M = Mn, Co, Ni, or Cu and OEC is the Trianion of 2, 3, 7, 8, 12, 13, 17, 18-Octaethylcorrole. *J. Am. Chem. Soc.* 1998. V. 120. P. 11986–11993.

105. **Kahn O.** Molecular Magnetism. VCH Publishers. 1993.

106. **Thomas K.E., Alemayehu A.B., Conradie J., Beavers C.M., Ghosh A.** The Structural Chemistry of Metallocorroles: Combined X-ray Crystallography and Quantum Chemistry Studies Afford Unique Insights. *Acc. Chem. Res.* 2012. V. 45. P. 1203–1214.

107. **Michl J.** Electronic structure of aromatic π-electron systems as reflected in their MCD spectra. *Pure. Appl. Chem.* 1980. V. 52. P. 1549–1563.

108. **Michl J.** Magnetic Circular Dichroism of Aromatic Molecules. *Tetrahedron.* 1984. V. 40. P. 3845–3934.

109. **Mugarza A., Krull C., Robles R., Stepanow S., Ceballos G., Gambardella P.** Spin Coupling and Relaxation Inside Molecule–Metal Contacts. *Nat. Commun.* 2011. V. 2. P. 490. DOI: 10.1038/ncomms1497.

110. **Fukuda T., Homma S., Kobayashi N.** Deformed Phthalocyanines: Synthesis and Characterization of Zinc Phthalocyanines Bearing Phenyl Substituents at the 1-, 4-, 8-, 11-, 15-, 18-, 22-, and/or 25-Positions. *Chem. Eur. J.* 2005. V. 11. P. 5205-5216.

111. **Kobayashi N., Fukuda T., Ueno K., Ogino H.** Extremely Non-Planar Phthalocyanines with Saddle or Helical Conformation: Synthesis and Structural Characterizations. *J. Am. Chem. Soc.* 2001. V. 123. P. 10740-10741.

112. **Fukuda T., Kobayashi N.** A Colormap Analysis Method for Visual Presentation of the Skeletal Deformations of Phthalocyanine Derivatives. *J. Porph. Phthal.* 2004. V. 8. P. 1251-1257.

113. **Sugimori T., Torikata M., Nojima J., Tominaka S., Tobikawa K., Handa M., Kasuga K.** Preparation and properties of octa-substituted phthalocyanines peripherally substituted with phenyl derivatives. *Inorg. Chem. Commun.* 2002. V. 5. P. 1031-1033.

114. **Konami H., Hatano H.** Synthesis and Spectroscopic Properties of Zn(II) Mono-2-(t-butyl)phthalocyanine. *Chem. Lett.* 1988. P. 1359-1362.

115. To confirm the "additivity", we have synthesized a series of para-substituted a-octaphenyl Pcs, that is, αααα, αααβ, αβαβ (opp), ααββ (adj), and ββββ, where a denotes 3,6-diphenylphthalonitrile units and b denotes 3,6-bis(4-methoxyphenyl)-4,5-dicyanobenzene units. The ligand deformations are expected to be almost identical from complex to complex on the basis of the molecular structures, and they show reasonable additivities of the Q-band energies with respect to the number of methoxy groups. In particular, the opposite and adjacent isomers show practically identical Q-band energies (i.e., 800 and 801 nm for metal-free αβαβ and ααββ isomers, respectively). Fukuda T., Doctoral Thesis, Tohoku University, 2004.

116. **Fukuda T., Homma S., Kobayashi N.** A Highly Deformed Iron(II) Low-Spin Phthalocyanine Which Shows Two MLCT Transitions beyond the Q-Band. *Chem. Commun.* 2003. P. 1574-1575.

117. **Edwards L., Gouterman M.** Porphyrins: XV. Vapor Absorption Spectra and Stability: Phthalocyanines. *J. Mol. Spectr.* 1970. V. 33. P. 292-310.

118. **Kobayashi N., Fukuda T.** Mono-Aromatic Ring-Fused versus Adjacently Di-Aromatic Ring-Fused Tetraazaporphyrins: Regioselective Synthesis and Their Spectroscopic and Electrochemical Properties. *J. Am. Chem. Soc.* 2002. V. 124. P. 8021-8034.

119. **Kobayashi N., Miwa H., Nemykin V.N.** Adjacent versus Opposite Type Di-Aromatic Ring-Fused Phthalocyanine Derivatives: Synthesis, Spectroscopy, Electrochemistry, and Molecular Orbital Calculations. *J. Am. Chem. Soc.* 2002. V. 124. P. 8007-8020.

120. **Fukuda T., Makarova E.A., Luk'yanets E.A., Kobayashi N.** Synthesis and Spectroscopic and Electrochemical Studies of Novel Benzo- or 2,3-Naphtho-Fused Tetraaza-chlorins, -bacteriochlorins, and -isobacteriochlorins. *Chem. Eur. J.* 2004. V. 10. P. 117-133.

121. **Lever A.B.P., Milaeva E.R., Speier G.** The Redox Chemistry of Metallophthalocyanines in Solution. In "Phthalocyanines – Properties and Applications". Ed. by C.C. Leznoff, A.B.P. Lever. V. III. Chap. 1. New York: VCH. 1993.

122. **Shimizu S., Hua Zhu H., Kobayashi N.** Azaphenalene Phthalocyanines: Phthalocyanine Analogues with Six- Membered-Ring Units Instead of Five-Membered-Ring Units. *Chem. Eur. J.* 2010. V. 16. P. 11151-11159.

123. **Rodoriguez-Morgade M., De La Torre G., Torres T.** Design and Synthesis of Low-Symmetry Phthalocuyanines and Related Systems. In "The Porphyrin Handbook". V. 15. Ed. by K.M. Kadish, K.M. Smith, R. Guilard. San Diego: Academic Press. 2003. pp. 125–160.

124. **Oliver S.W., Smith T.D.** Oligomeric Cyclization of Dinitriles in the Synthesis of Phthalocyanines and Related Compounds: the role of the Alkoxide Anion. *J. Chem. Soc. Perkin Trans.* 1987. V. 2. P.1579-1582.

125. **Scheidt W.R.** Systematics of the Stereochemistry of Porphyrins and Metalloporphyrins. in "The Porphyrin Handbook". V. 3. Ed. by K.M. Kadish, K.M. Smith, R. Guilard. San Diego: Academic Press. 2000. pp. 49–112.

126. **Kobayashi N., Nakajima S., Ogata H., Fukuda T.** Synthesis, Spectroscopy, and Electrochemistry of Tetra-tert-Butylated Tetraazaporphyrins, Phthalocyanines, Naphthalocyanines, and Anthracocyanines, together with Molecular Orbital Calculations. *Chem. Eur. J.* 2004. V. 10. P. 6294-6312.

127. **Honda T., Kojima T., Kobayashi N., Fukuzumi S.** Crystal Structures and Electronic Properties of Saddle-Distorted and Protonated Phthalocyanines. *Angew. Chem. Int. Ed.* 2011. V. 50. P. 2725-2728.

128. **Ogunsipe A., Nyokong T.** Effects of Substituents and Solvents on the Photochemical Properties of Zinc Phthalocyanine Complexes and Their Protonated Derivatives. *J. Mol. Struct.* 2004. V. 689. P. 89-97.

129. a) **Kojima T., Honda T., Ohkubo K., Shiro M., Kusukawa T., Fukuda T., Kobayashi N., Fukuzumi S.** A Discrete Supramolecular Conglomerate Composed of Two Saddle-Distorted Zinc(II)-Phthalocyanine Complexes and a Doubly Protonated Porphyrin with Saddle-Distortion Undergoing Efficient Photoinduced Electron Transfer. *Angew. Chem. Int. Ed.* 2008. V. 47. P. 6712-6716. b) **Honda T., Kojima T., Fukuzumi S**. Crystal Structures and Properties of a Mono-protonated Porphyrin. *Chem. Commun.* 2009. P. 4994-4996.

130. **Stuzhin P.A., Khelevina O.G., Berezin B.D.** Azaporphyrins: Acid-Base Properties. In "Phthalocyanines-Properties and Applications". Ed. by C.C. Leznoff, A.B.P. Lever. V. IV. Chap. 2 (pp. 19-77). New York, Weinheim, Cambridge: VCH. 1996.

131. **Shimizu S., Zhu H., Kobayashi N.** Azepiphthalocyanine— an Unprecedented Large Twist of a π-Conjugation System upon Core-Modification with a Seven-Membered Ring Unit. *Chem. Commun.* 2011. V. 47. P. 3072–3074.

132. **Fukuda T., Kobayashi N.** Hydrogenated Tetraazaporphyrins - Old but New Core-Modified Phthalocyanine Analogues. *Dalton Trans.* 2008. P. 4685-4704.

133. **Furuyama T., Ogura Y., Yoza K., Kobayashi N.** Superazaporphyrins: Meso-Pentaazapentaphyrins and One of Their Low-Symmetry Derivatives. *Angew. Chem. Int. Ed.* 2012. V. 51. P. 11110–11114.

134. a) **Bloor J.E., Schlabitz J., Walden C.C.** Organic Complexes of Uranium: Part I. The Synthesis and Spectrum of Uranyl Phthalocyanine. *Can. J. Chem.* 1964. V. 42. P. 2201-2208; b) **Day V.W., Marks T.J., Wachter W.A.** Large Metal Ion-Centered Template Reactions. Uranyl Complex of Cyclo-pentakis(2-iminoisoindoline). *J. Am. Chem. Soc.* 1975. V. 97. P. 4519-4527.

135. a) **Takeuchi Y., Matsuda A., Kobayashi N.** Synthesis and Characterization of *meso*-Triarylsubporphyrins. *J. Am. Chem. Soc.* 2007. V. 129. P. 8271-8281. b) **Kobayashi N., Takeuchi Y., Matsuda A.** *meso*-Aryl Subporphyrins. *Angew. Chem. Int. Ed.* 2007. V. 46. P. 758-760.

136. **Claessens, C. G., Torres, T.** Subphthalocyanines: Singular Nonplanar Aromatic Compounds - Synthesis, Reactivity, and Physical Properties. *Chem. Rev.* 2002. V. 102. P. 835-854.

137. **Inokuma Y., Kwan J. H., Ahn T. K., Yoon M. C., Kim D., Osuka A**. Tribenzosubporphines: Synthesis and Characterization. *Angew. Chem., Int. Ed.* 2006. V. 45. P. 961-964.

138. **Stork J.R., Brewer J.J., Fukuda T., Fitzgerald J.P., Yee G.T., Nazarenko A.Y., Kobayashi N., Durfee W.S.** Chloro and Hydroxo Forms of a Boron(III) Subtriazaporphyrin Macrocycle. *Inorg. Chem.* 2006. V. 45. P. 6148-6151.

139. **Scheidt W.R., Kasatner M.E., Hatano K.** Stereochemistry of the toluene solvate of α,β,γ,δ-tetraphenylporphinato-zinc(II). *Inorg. Chem.* 1978. V. 17. P. 706-710.

140. **Senge M.O.** Database of Tetrapyrrole Crystal Structure Determinations. Ed. by K. M. Kadish, K. M. Smith, R. Guilard. San Diego: Academic Press. 2000. V. 10. P. 1-218.

141. **Kadish K.M., Royal G., Gueletti L.** Metalloporphyrins in Nonaqueous Media: Database of Redox Potentials. In "The Porphyrin Handbook". Ed. by K. M. Kadish, K. M. Smith, R. Guilard. San Diego: Academic Press. 2000. V. 9. Chap. 59. P. 1-219.

142. **Rao T.A., Maiya B.G.** Spectroscopic, Redox and Emission Properties of 2-Nitro-Substituted Free Base- and Metallo-Tetra-Aryl Porphyrins. *Polyhedron.* 1994. V. 13. P. 1863-1873.

143. **Ishii K., Kobayashi N., Matsuo T., Tanaka M., Sekiguchi A.** Observation of the Predicted Negative Faraday A MCD Term in a Cyclobutadiene Dianion. *J. Am. Chem. Soc.* 2001. V. 123. P. 5356-5357.

144. **Kobayashi N., Ishizaki T., Ishii K., Konami H**. Synthesis, Spectroscopy, and Molecular Orbital Calculations of Subazaporphyrins, Subphthalocyanines, Subnaphthalocyanines, and Compounds Derived Therefrom by Ring Expansion. *J. Am. Chem. Soc.* 1999. V. 121. P. 9096-9110.

145. **Stork J.R., Brewer J.J., Fukuda T., Fitzgerald J.P., Yee G.T., Nazarenko A.Y., Kobayashi N., Durfee W.S.** . Chloro and Hydroxo Forms of a Boron(III) Subtriazaporphyrin Macrocycle. *Inorg. Chem.* 2006. V. 45. P. 6148-6151.

146. **Stillman M.J., Nyokong T.** Absorption and Magnetic Circular Dichroism Spectral Properties of Phthalocyanines. Part 1: Complexes of the Dianion, Pc(-2). In "Phthalocyanines-Properties and Applications". Ed. by C.C. Leznoff, A.B.P. Lever. Weinheim: VCH. 1989. Chap. 3. P. 133-289.

147. **Vancoillie S., Hendrickx M., Holz T., Nguyen M. T., Pierloot K., Ceulemans A., Mack J., Kobayashi N.** Fourteen-Electron Ring Model and the Anomolous Magnetic Circular Dsichroism of meso-Triarylsubporphyrins. *J. Phys. Chem. A.* 2012. V. 116. P. 3960−3967.

148. **Seybold P. G., Gouterman M.** Porphyrins: XIII: Fluorescence Spectra and Quantum Yields. *J. Mol. Spectrosc.* 1969. V. 31. P. 1-13.

149. **Xue Z. L., Shen Z., Mack J., Kuzuhara D., Yamada H., Okujima T., Ono N., You X. Z, Kobayashi N.** A Facile One-Pot Synthesis of *meso*-Aryl-Substituted [14]Triphyrin(2.1.1). *J. Am. Chem. Soc.* 2008. V. 130. P. 16478–16479.